

Design and Analysis of Magnetocaloric Devices for Cooling Heating and Waste Heat Recovery

Huang, B.

DOI

[10.4233/uuid:1027d16b-3082-438d-8d9c-ef2949c11211](https://doi.org/10.4233/uuid:1027d16b-3082-438d-8d9c-ef2949c11211)

Publication date

2024

Document Version

Final published version

Citation (APA)

Huang, B. (2024). *Design and Analysis of Magnetocaloric Devices for Cooling Heating and Waste Heat Recovery*. [Dissertation (TU Delft), Delft University of Technology]. <https://doi.org/10.4233/uuid:1027d16b-3082-438d-8d9c-ef2949c11211>

Important note

To cite this publication, please use the final published version (if applicable).
Please check the document version above.

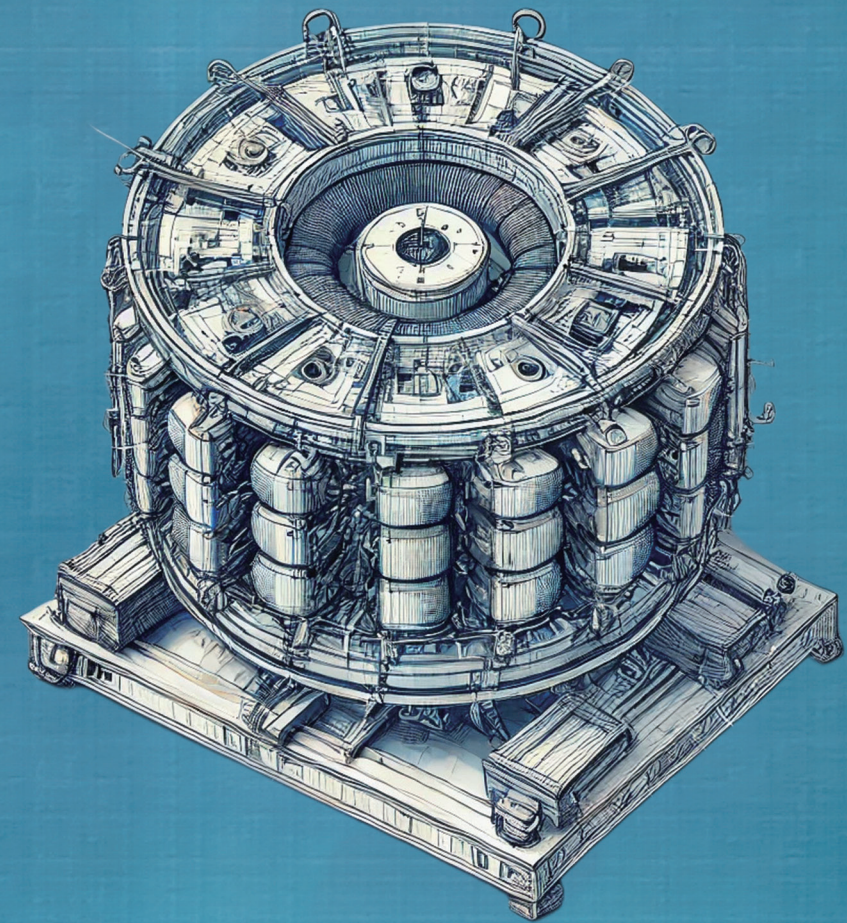
Copyright

Other than for strictly personal use, it is not permitted to download, forward or distribute the text or part of it, without the consent of the author(s) and/or copyright holder(s), unless the work is under an open content license such as Creative Commons.

Takedown policy

Please contact us and provide details if you believe this document breaches copyrights.
We will remove access to the work immediately and investigate your claim.

Design and Analysis of Magnetocaloric Devices for Cooling Heating and Waste Heat Recovery

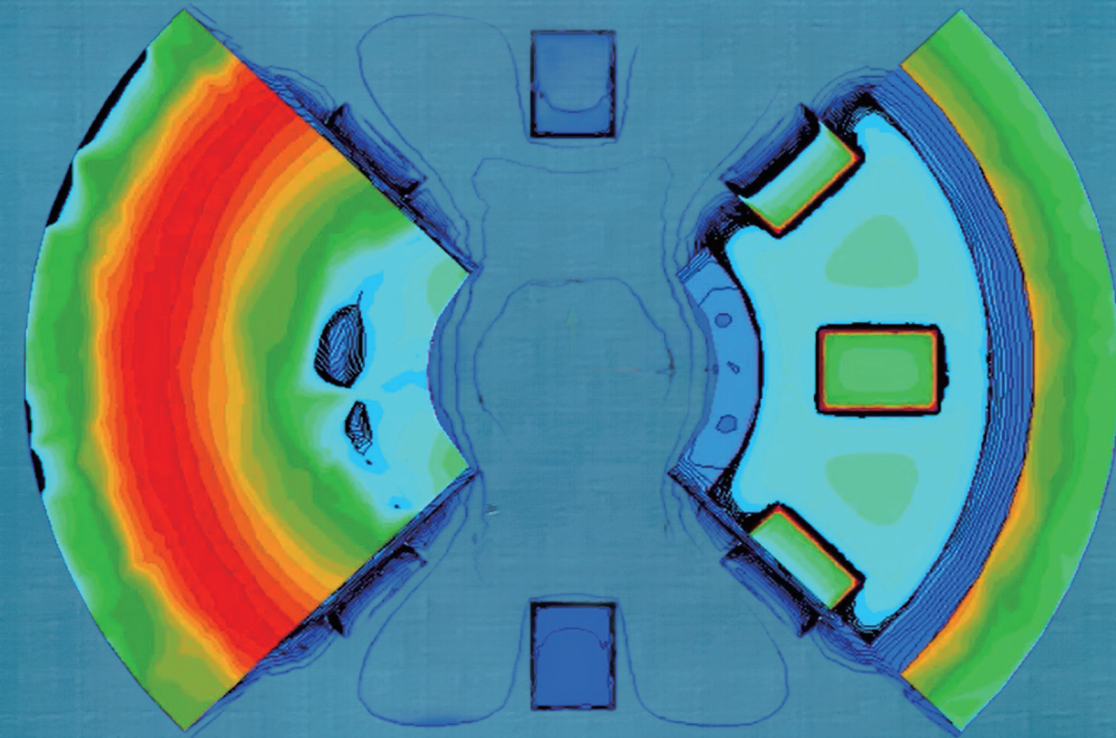


Bowei Huang
黄博微

Design and Analysis of Magnetocaloric Devices for Cooling Heating and Waste Heat Recovery

Bowei Huang

 TU Delft



Propositions belonging to this thesis

Design and Analysis of Magnetocaloric Devices for Cooling Heating and Waste Heat Recovery

by
Boweï Huang

1. There is no technology without science.
2. Scientific experiments are well planned miracles, and industrialization is to transform these miracles into everyday form.
3. In scientific research, taking shortcuts usually means more work in the future.
4. One can only know the world by travelling.
5. Creation is like mixing a potion. More passion creates art, more rationality leads to science. A balanced mix? That's engineering.
6. A great discovery needs more than observation; timing and imagination are also needed.
7. Stress without direction is turbulence, stress with direction is flow.
8. Every little bit of energy harvested from waste is a gain.
9. Magnetic heat pumps have the future.
10. For now, thermomagnetic motors are more promising than thermal magnetic generators.

These propositions are regarded as opposable and defensible, and have been approved as such by the promoters Dr N.H. van Dijk and Prof. dr E.H. Brück

Design and Analysis of Magnetocaloric Devices for Cooling Heating and Waste Heat Recovery

Bowei Huang

Design and Analysis of Magnetocaloric Devices for Cooling Heating and Waste Heat Recovery

Dissertation

for the purpose of obtaining the degree of doctor
at Delft University of Technology
by the authority of the Rector Magnificus, Prof. dr. ir. T.H.J.J. van der Hagen,
chair of the Board for Doctorates
to be defended publicly on
Monday 9 September 2024 at 15:00

by

Bowei Huang

Master of Science in Control Theory and Control Engineering
Hunan University of Science and Technology

Cover image: Bowei Huang and DALL E
Lay-out: Ilse Modder (www.ilsemodder.nl)
Printed by: Gildeprint Enschede (www.gildeprint.nl)
ISBN/EAN: 978-94-6496-190-4

Copyright © 2024 B. Huang

All rights reserved. No part of this thesis may be reproduced, stored or transmitted in any form or by any means, without permission of the author, or when appropriate, by the publishers of the included scientific papers.

This dissertation has been approved by the promotor.

Composition of the doctoral committee:

Rector Magnificus

Prof.dr. E.H. Brück,

Dr.ir. N.H. van Dijk

Chairman

Delft University of Technology, promotor

Delft University of Technology, promotor

Independent members:

Prof.dr. A. Kitanovski

University of Ljubljana, Slovenia

Prof.dr. M. Lo Bue

ENS Paris Saclay, France

Prof.dr. M. Shahi

University of Twente, the Netherlands

Prof.dr. K. Hooman

Delft University of Technology

Prof.dr. R. Pecnik

Delft University of Technology

Dedicated to my parents my wife Huijun and my daughter Celine

致我的父母，爱人和女儿



This work is part of the Industrial Partnership Program IPP I28 of the Dutch Foundation for Fundamental Research on Matter (FOM), which is the former physics division of NWO, financially supported by BASF New Business.

Keywords: Magnetocaloric, Thermodynamics, Magnetic heat pump, Thermomagnetic motor

TABLE OF CONTENTS

1	Introduction	11	5	Development of a proof-of-concept Thermomagnetic Motor	89
1.1	Brief history of Magnetocaloric technology	12	5.1	Introduction	90
1.2	Magnetocaloric effect	13	5.2	Design and Features	93
1.3	MCE from thermodynamical perspective	14	5.3	Experiment and result	99
1.4	Applied Thermodynamic cycles for Magnetocaloric technology	16	5.4	Improve the performance of TMM with MnFePSiV	101
1.5	Magnetocaloric materials	19	5.5	Conclusions	122
1.6	Shape of the Magnetocaloric materials	21	References		124
1.7	Other main components of a magnetocaloric device	26			
1.8	Prototypes of magnetocaloric devices	30	Appendices		127
1.9	The scope of the dissertation	37	Summary		128
References		38	Nederlandse samenvatting		130
			Acknowledgements		132
			Curriculum vitae		135
2	Experimental Techniques	45			
2.1	SQUID	46			
2.2	MDSC	46			
2.3	NI CompactRIO	47			
2.4	Delta SM300-10 DC power source	47			
2.5	Schneider servo drive LXM32M	48			
References		49			
3	Prototype Heat Pump – MMFF cooler	51			
3.1	Background of design	52			
3.2	System features	53			
3.3	Experiment and results	59			
3.4	Conclusion	62			
References		63			
4	Experimental Rotary Magnetic Refrigerator Prototype and its performance optimization	65			
4.1	Introduction	66			
4.2	Design overview	67			
4.3	Performance metrics	74			
4.4	Experiment and discussion	76			
4.5	System Fine-tuning and the result	80			
4.6	Conclusions	84			
		85			

CHAPTER 1

Introduction

Magnetocaloric technology utilizes magnetocaloric material (MCM) to effectively convert magnetic energy into thermal energy and vice versa. When exposed to a magnetic field, MCMs change their temperature. In the reversed process, cooling or heating MCMs across the magnetic transition activate or deactivate their magnetic state. Therefore, magnetocaloric technology can be applied for heating and cooling applications as well as electric power generation applications. During the recent 30 years, scientists and engineers have proven this technology in many experiments and demonstrations ranging from wine coolers to power generators. While their simple mode of operation has been intriguing, their nonideal efficiency, limited temperature ranges, and high costs have been major barriers to their wide-scale use in existing and novel applications. During my PhD research, I implemented magnetocaloric technology in multiple applications and explored methods to improve the system efficiency by combining improvements in system engineering and material shaping techniques.

1.1 BRIEF HISTORY OF MAGNETOCALORIC TECHNOLOGY

There is an ongoing debate in the scientific community about who should be credited for the discovery of the magnetocaloric effect, though many sources agree upon it being first observed and named as such by the French physicist P. Weiss and Swiss physicist A. Piccard in 1917, who established the physical principles that govern the MCE phenomenon[1]. This allowed the first application of the MCE to arise from the proposals of Debye in 1926 and Giauque in 1927 [2]. Their proposals aimed to create magnetic refrigeration cycles to reach temperatures below liquid helium. In 1933, Giauque and MacDougall were able to experimentally achieve a temperature of 242 mK with gadolinium sulfate [3]. This breakthrough overtook the 1K barrier for the first time, and earned Giauque a Nobel Prize. It is an important landmark in the history of cooling and magnetic cooling technology. The feasibility of magnetic refrigeration at room temperature was introduced by Brown in 1976 [4]. He created a magnetic refrigerator prototype working in accordance with an Ericsson cycle. The prototype used Gd metal plates as active material and a magnetic field created by superconducting magnets. In 1997, Pecharsky and Gschneidner discovered gadolinium-based alloy materials with large magnetocaloric response at room temperature, and in 2001, researchers at Astronautics Cooperation build a magnetic refrigerator prototype, which replaced the superconducting magnet for the first time by permanent magnets. Around 2000, two widely tunable magnetocaloric material families have been discovered. Fujita et al.[5] presented in 1999 La-Fe-Si compounds, which contain only light rare-earth element. Brück et al. [6] published the study on Mn-Fe-P-As in 2002, which is the first rare-earth free magnetocaloric material. These two discoveries sparked the interest of not only

universities and research institutes but also companies around the world, such as BASF in Germany, Cooltech in France, Camfridge in UK, General Electric in the USA. Since then, numerous publications and patents regarding magnetocaloric materials and magnetocaloric devices have emerged.

1.2 MAGNETOCALORIC EFFECT

The foundation of magnetocaloric technology is the Magnetocaloric effect (MCE). MCE is a phenomenon which describes that magnetic materials change their temperature when exposed to a changing magnetic field. The temperature change in such a material is best explained as the result of entropy exchange between the magnetic structure of the material and the lattice structure of the material, when these materials become magnetized (or demagnetized). The applied magnetic field on the material forces the magnetic moments in the material to align with the field. This decreases the magnetic entropy in the material and increases the lattice entropy of the material, which result in random thermal motion and an increase in temperature[6-10].

Figure 1.1 is a temperature (T)–entropy (S) diagram that displays a ferromagnetic material under two different magnetic fields - one with zero magnetic field (H_0) and another with a non-zero magnetic field (H_1). When we apply the magnetic field adiabatically and reversibly, which means the total entropy of the system remains constant during the magnetic field change, the MCE can be calculated as the isentropic difference between the corresponding functions, which is shown in the graph as a horizontal arrow (ΔT_{ad}). This process is called adiabatic temperature change, which can be calculated as equation 1-1:

$$\Delta T_{ad} = T_1(S_0, H_1) - T_0(S_0, H_0) \quad (1-1)$$

Another way to express the MCE is through the isothermal magnetic entropy change (ΔS_M), which is represented by a vertical arrow. This process can be calculated as equation 1-2:

$$\Delta S_M = S_1(T_0, H_0) - S_0(T_0, H_1) \quad (1-2)$$

It's important to note that both ΔT_{ad} and ΔS_M are affected by the initial temperature (T_0) and the change in magnetic field ($\Delta H = H_1 - H_0$).

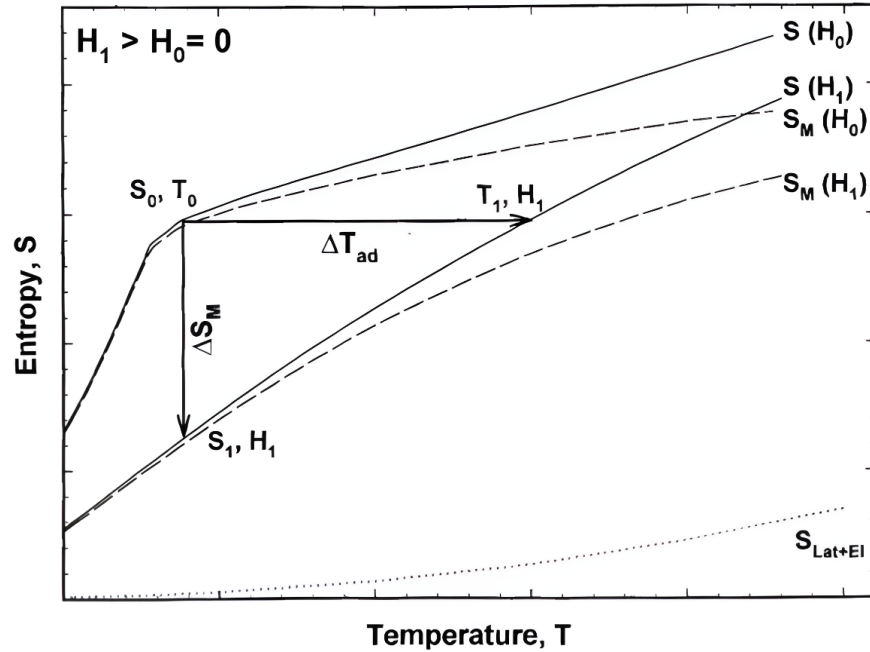


Figure 1.1: This TS-graph demonstrates the entropy of a MCM as a function of its temperature under different applied magnetic field. Note that the area under the curve in the graph is equal to the internal energy of the MCM [7].

1.3 MCE FROM THERMODYNAMICAL PERSPECTIVE

To further explore the analytical expression of MCE in form of T_{ad} and ΔS_M , it is necessary to understand the interrelatedness between the used variables in the thermodynamical frame of reference.

Entropy is a measure of the number of possible states a system can have, which is determined by the sum of its micro-states. Micro-states are determined by the individual atoms, molecules, etc. that occupy the system, and are dependent on various factors such as particle location, speed, and direction. The total entropy of a magnetocaloric system is a sum of its components, which include the magnetic entropy ΔS_M , crystal lattice entropy ΔS_{lat} and entropy of the conduction electrons ΔS_{el} . In magnetic materials, these components are either dependent on B (magnetic field), T (temperature), or both. The total entropy of a magnetic material can thus be described as the sum of the entropy components and their dependencies (B , T) [10], so that,

$$\Delta S_{tot}(B, T) = \Delta S_M(B, T) + \Delta S_{lat}(T) + \Delta S_{el}(T) \quad (1-3)$$

where:

$$\Delta S_{tot}(B, T) = \text{total entropy change [J/(kg·K)]}$$

$$\Delta S_M(B, T) = \text{magnetic entropy change [J/(kg·K)]}$$

$$\Delta S_{lat}(T) = \text{crystal lattice entropy change [J/(kg·K)]}$$

$$\Delta S_{el}(T) = \text{conduction electron entropy change [J/(kg·K)]}$$

In magnetocaloric applications, people mainly consider the magnetic entropy ΔS_M , crystal lattice entropy ΔS_{lat} , because the contribution of the conduction electron entropy is negligible near room temperature. In an adiabatic magnetization process, the value of ΔS_M decreases while ΔS_{lat} increases in the form of heat, as the total entropy of the system ΔS_{tot} is fixed. [8]

The values of ΔT_{ad} and ΔS_M can be calculated by using one of the fundamental Maxwell relations:

$$\frac{1}{\mu_0} \left(\frac{\partial S(T, H)}{\partial H} \right)_T = \left(\frac{\partial M(T, H)}{\partial T} \right)_H \quad (1-4)$$

Where $M(T, H)$ is the magnetization of the material. After integration (for an isothermal-isobaric process) yields:

$$\Delta S_M(T, \Delta H) = \int_{H_1}^{H_2} \left(\frac{\partial M(T, H)}{\partial T} \right)_H dH \quad (1-5)$$

Since the heat capacity C_p is defined in the second law of thermodynamics:

$$C_p(T, H) = T \left(\frac{\partial S}{\partial T} \right)_H \quad (1-6)$$

Using equation (2-2) and the fundamental equations $CdT = dQ$ and $dQ = -TdS$ (The proportion that the magnetic entropy decreased is the increase of lattice heat) we get for infinitesimal adiabatic temperature rise:

$$dT = - \left(\frac{T}{C_p(T, H)} \right)_M \left(\frac{\partial M(T, H)}{\partial T} \right)_H dH. \quad (1-7)$$

After integrating Eq.(1-7) we obtain the value of the magnetocaloric effect as:

$$\Delta T_{ad}(T, \Delta H) = - \int_{H_0}^{H_1} \left(\frac{T}{C_p(T, H)} \right)_M \left(\frac{\partial M(T, H)}{\partial T} \right)_H dH. \quad (1-8)$$

On the other hand, the magnetic entropy change can be obtained more directly from a magnetocaloric measurement of the field dependence of the heat capacity by the integration:

$$\Delta S_M(T, H) = \int_0^T \frac{C_p(T', H) - C_p(T', 0)}{T'} dT' \quad (1-9)$$

where $C_p(T, H)$ and $C_p(T, 0)$ are the values of the heat capacity measured in a field H and in zero field, respectively. Foldeaki et al [11] and Spichkin et al [12] confirmed that the values of $\Delta S_M(T, H)$ derived from the magnetization measurement coincide with the values from calorimetric measurement. This is the direct proof of the reversible convertibility of magnetic energy and thermal energy in MCMs.

Some additional point shall be made at this point. First, since the magnetization at constant field of paramagnets and simple ferromagnets decreases with increasing temperature [i.e. $(\frac{\partial M}{\partial T})_H < 0$], then $\Delta S_M(T, H)$ should be negative (Eq. (1-4) and (1-5)), while $\Delta T_{ad}(T, \Delta H)$ should be positive (Eq. (1-7) and (1-8)), which agrees with Fig. 1.1.

Second, in ferromagnets $|\left(\frac{\partial M}{\partial T}\right)_H|$ is the largest at the Cuire Temperature (T_c), and therefore, $|\Delta S_M(T, H)|$ should peak at TC (Eq. (1-4) and (1-5)).

Third, for the same $\Delta S_M(T, H)$, the $\Delta T_{ad}(T, \Delta H)$ will be larger at a higher absolute temperature, and also when the total heat capacity of the solid is lower (Eq. (1-8)). The latter point is critical in understanding the fact that paramagnets display significant $\Delta T_{ad}(T, \Delta H)$ only at temperatures close to absolute zero, where the limited value of $|\left(\frac{\partial M}{\partial T}\right)_H|$ is easily offset by the negligible lattice heat capacity.

Furthermore, at high temperatures the measurable adiabatic heating (or cooling) is expected only if the solid orders spontaneously, i.e. when the value of $|\left(\frac{\partial M}{\partial T}\right)_H|$ becomes significant.

1.4 APPLIED THERMODYNAMIC CYCLES FOR MAGNETOCALORIC TECHNOLOGY

To utilize the MCE in different applications, suitable thermodynamic cycles are needed. In figure 1.2, we can see the relationship between entropy (S) and temperature (T) for various cycles such as the Carnot, Brayton, and Ericsson cycles. The upper curve in figure 1.2 represents a material that is in a zero-magnetic field ($H=0$), while the lower curve represents a material that is in a magnetic field with a non-zero strength ($H \neq 0$). The rectangle ABCD represents the non-regenerative Carnot cycle which includes two isentropic (A-B and C-D) and two isothermal (B-C and D-A) processes. Additionally, the figure also presents the Ericsson regenerative cycle (A-F-C-E) and Brayton cycle (A-G-C-H). These two regenerative cycles include processes at a constant field, which makes it possible to take full advantage of the change in the magnetic part of the entropy generated when the magnetic field changes. In the Ericsson cycle, the magnetic field changes isothermally (F-C and E-A processes), while in the Brayton cycle, it changes

adiabatically (A-G and C-H processes). In both Ericsson cycle and Brayton cycle the processes at constant field require thermal regeneration. The component in which the thermal generation happens is called a regenerator, it transfers heat between different parts of the cycle, which allows for an increase of the working temperature difference. The regenerator stores heat in itself in the part of the cycle where heat is generated by the working material (the MCM) and gives it up in the part where the working material absorbs it. This is especially important in magnetocaloric heat pumps since the values of the adiabatic temperature change of MCMs are usually much smaller than the required working temperature difference. In Figure 1.2, thermal energy should be absorbed by the regenerator during processes in a non-zero magnetic field (C-E and G-C for Ericsson and Brayton cycles, respectively) and be given by the regenerator during processes in a zero-magnetic field (A-F and H-A for Ericsson and Brayton cycles, respectively).

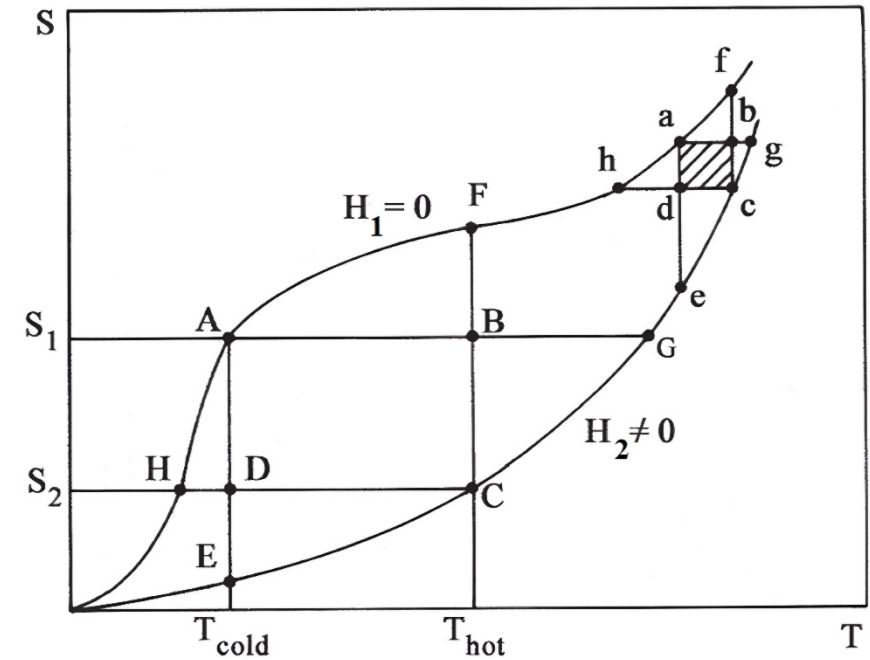


Figure 1.2: $S - T$ diagrams of the Carnot, Brayton and Ericsson cycles[13]

At temperatures span above 20 K, the Carnot cycle becomes less effective, according to research [13]. This is because the entropy of solids increases strongly at higher temperatures, leading to a decrease in the operating temperature span, see the rectangle abcd at the upper right corner of figure 1.2. The temperature span is limited

to the ΔT of the working material, and for the Carnot cycle, it is only several K at room temperature region. Therefore, regenerative cycles like Brayton, Ericsson, and AMR cycle (active magnetic regeneration cycle) have become more popular in devices operating at temperatures above 20 K. These cycles allow for an increase in the temperature span. The Carnot cycle, as well as the Brayton, Ericsson, and AMR cycles, have been discussed in detail in review [14].

An effective way to enhance temperature span is by using cascading thermodynamic cycles [15]. Magnetocaloric materials possess the highest MCE at their specific Curie temperature. As the working temperature moves away from this temperature, the MCE decreases. In applications that require a large temperature span, there is reduced efficiency due to the decrease of MCE caused by the deviation of T_c . To tackle this problem, one solution is to implement a cascade system of cycles where each cycle involves a different material with a T_c in proximity to its application so that its working domain and operating temperature range are optimal.

Fig. 1.3 (a) shows a cascade process of Ericsson cycles, showing that the cooling power of cycle (A) is used to absorb the energy rejected by cycle (B). The heat absorbed from the cold source by the cascade refrigeration system is represented by the surface S_{4b} , 4b, 3b, S_{3b} of cycle (B). The total work carried out in the cascade system is given by the sum of the areas formed by the two cycles, (A) and (B). The temperature spans of these two cycles are also combined. Instead of a span of T_h to T_{mix} for the cycle (A) and T_{cold} to T_{mix} for the cycle (B), the cascaded cycle has a temperature span of T_h to T_{cold} . Note that the two cycles (A) and (B) has some overlap around the temperature T_{mix} , which is a redundancy to ensure the cascade will work even if any cycle in the cascade is non-ideal due to the manufacturing imperfection.

A major advantage of a magnetic refrigeration cascade system over that of a conventional one is that the MR machine does not require heat exchangers between cycles. This is due to the fact that magnetocaloric material is solid so that the heat transfer media (usually is a fluid, that is so-called HTF) can transfer heat between these cascaded cycles. In application, there are two ways of cascading the thermodynamic cycles: the first one is to stack several of MCMs with sequential T_c s in one regenerator to bridge the temperature span of the regenerator, the so-called layered AMR concept. The MCM layering strategy has been explored experimentally by Govindappa et al [16] on MnFePAs material family and Navickaitė et al [17] on LaFeSi material family. Quijano et al developed a layering strategy with numerical modeling [18], a temperature – entropy diagram indicates the properties of the layered MCMs is shown in Fig. 1.3 (b). The other one is associated with the use of multi-stage AMR. In this case, each AMR stage uses different magnetic materials and each AMR stage has its own operating range [19].

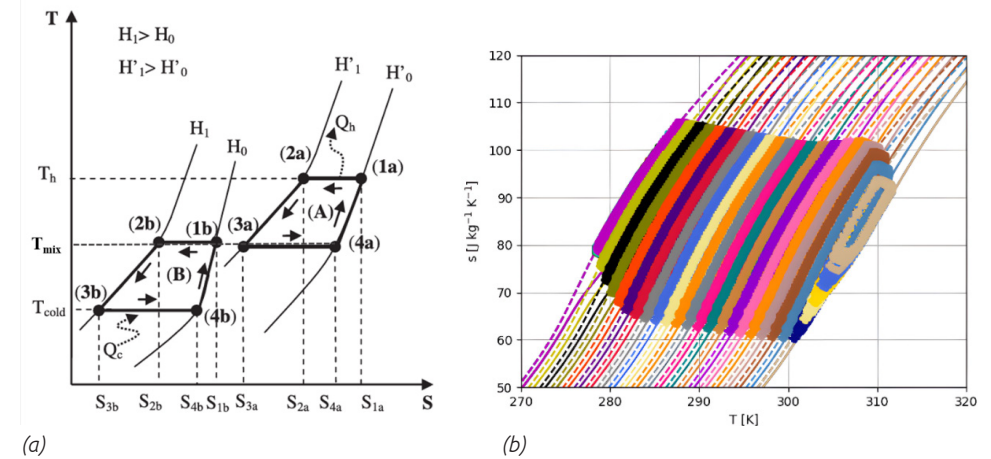


Figure 1.3: cascaded thermodynamic cycle (a) and multi-layer AMR strategy (b)

1.5 MAGNETOCALORIC MATERIALS

In fact, MCE is an intrinsic property of all magnetic materials, but not all magnetic materials are magnetocaloric material (MCM). For different magnetic materials, MCE can only be induced within a certain temperature range, and it also differs from the intensity of the temperature change. Therefore, at this moment, only a range of materials which possess decent intensity of MCE at an applicable temperature range are considered as MCM.

Over the last century and especially the last decade an increasing amount of research has been done in the field of magnetocalorics. An important part of this research has been towards the development of tunable magnetocaloric materials for room temperature applications.

After the discovery of the 'giant' MCE, the search for promising magnetocaloric refrigerants focused on rare-earth compounds due to their high ordering temperatures. Intermetallic lanthanum based compounds, such as $\text{La}(\text{Fe,Si})_{13}$ which crystallize in the NaZn_{13} type structure (1:13 phase), and the transition metal-based compounds $\text{MnFe}(\text{P,As})$, which crystallize in the Fe_2P type structure [14] are among the most promising magnetic refrigerants for near room-temperature magnetic cooling. Detailed reviews of magnetocaloric materials for applications at room temperature have been carried out by Gschneidner Jr. et al. (2005), Liu et al. (2012), Franco et al. (2012) and Liu (2014). Fig.1-4 summarizes the maximum adiabatic temperature change (ΔT_{ad}), maximum magnetic entropy change (ΔS) under cycling applied field of 2 Tesla versus transition

temperature for different families of magnetocaloric materials[20].

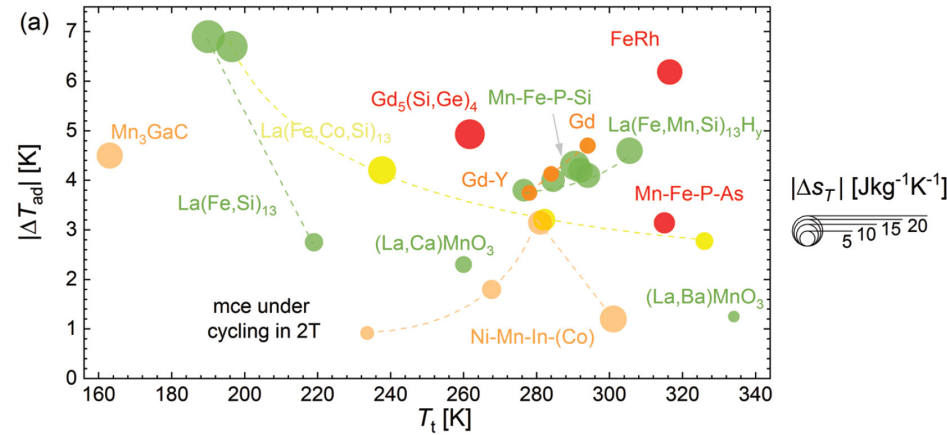


Figure 1.4: Ashby-like diagrams of magnetocaloric materials: maximum ΔT_{ad} and ΔS under cycling applied field of 2 tesla, versus transition temperature

1.5.1 Major magnetocaloric material families

Gadolinium and its compound

Gadolinium metal and gadolinium-based MCMs have been extensively studied for their MCE properties, mechanical stability, and shaping compatibility since the discovery of giant magnetocaloric effect (GMCE) in 1997[21]. Thanks to its easy applicability and availability, gadolinium has become a benchmark material in magnetocaloric communities around the world. Gadolinium exhibits a second-order magnetic transition due to the localized magnetic moment, with a Curie temperature around 293 K and an adiabatic temperature change (ΔT_{ad}) of 3 K for a magnetic field change of 1 T[13]. Substituting gadolinium with other rare-earth elements like dysprosium, terbium, and holmium in $Gd_{1-x}R_x$ alloys resulted in a table-like magnetocaloric effect over the temperature range of 210-300 K[22-24]. A significant temperature span of 40 K was achieved by making them into multilayer composites, such as the Gd-Ho-Y composite with a frequency of 0.4 Hz[25]. Due to its large magnetic moment, negligible hysteresis, good mechanical stability, and tuneable Curie temperature, gadolinium is still considered the standard material for magnetic refrigeration. However, its high cost limits its large-scale commercial application and, therefore, is of less interest.

La(Fe,Si)₁₃ alloy

The La(Fe,Si)₁₃ alloy is one of the most well-known pre-commercialized MCM. The LaFe_{13-x}Si_x alloy family[5, 26] have a NaZn₁₃-type structure. It exhibits a GMCE due to the itinerant electron meta-magnetic transition near a T_c of 200 K[27]. Efforts have been made to

shift the T_c to room temperature while maintaining the GMCE by changing the magnetic environment of the Fe atoms through the substitution of Co, Mn, Si, etc., or by introducing small atoms interstitial insertion like the C, N, B and H atoms. The most effective additions are the hydrides LaFe_{13-x}Si_xH_y and the substitution of Fe by Co[28, 29].

The Co substitution in La(Fe, Co)_{13-x}Si_x can increase the TC and retain the giant MCE due to the strong Fe-Co exchange interaction [30]. Increasing the Co content would transfer the FOMT to SOMT. Therefore, by optimizing the Co content, a low hysteresis and a giant MCE can be achieved in the La(Fe, Co)_{13-x}Si_x alloys. More stable mechanical properties make this family promising to be tested in a magnetic cooling system.

Hydrogenation of La(Fe,Si,Mn)₁₃ is effective to shift the TC to room temperature as a first-order-type material[31]. This is quite promising for practical applications. However, the mechanical brittleness and chemical instabilities hinder its application in magnetic refrigeration.

(Mn,Fe)₂(P,Si) alloy

MnFeP_{1-x}As_x alloys, with a hexagonal Fe₂P-type phase, exhibit a giant magnetocaloric effect (GMCE)[32]. However, the toxic element As hampers their application in real devices, leading researchers to discover a new family of MnFeP_{1-x}Gex alloys[33, 34]. Efforts to replace Ge led to the investigation of Mn_{1.25}Fe_{0.70}P_{1-x}Si_x and Mn_xFe_{1.95-x}P_{0.50}Si_{0.50} alloys[35, 36]. MnFeP_{1-x}Si_xB_y alloys [37] are promising magnetic refrigerants due to their excellent performance, cheap, abundantly available, non-toxic elements, and tuneable T_c . The doping of interstitial C and N atoms in the Mn-Fe-P-Si alloys tunes the FOMT to a SOMT[38, 39]. Co and Ni substitution in Mn-Fe-P-Si alloys also transfers the FOMT to a SOMT[40, 41]. BASF prepared spherical samples of Mn-Fe-P-Si alloys using the gas atomization process, which showed a magnetic entropy change of 12 to 18 J/kgK under a magnetic field change of 1.5 T. The MnFePSi product of BASF has been tested in several magnetic cooling devices, the results are promising[42, 43].

Heusler alloys

The X₂YZ Heusler alloys display the magnetocaloric effect (MCE), with Ni₂MnZ (Z = Sn, In, Sb) exhibiting an inversed MCE. This is due to the lower magnetization of the martensitic phase at lower temperatures and higher magnetization of the austenite phase at higher temperatures[44]. However, the transition requires a large magnetic field and the inversed MCE is irreversible[45]. Liu et al. [46] proposed a solution by using external stimuli. On the other hand, Ni₂Mn_{1.4}In_{0.6} with a single L₂₁ phase[47] exhibits a large ground-state magnetic moment and reversible MCE, making it a promising candidate for magnetic heat pump at room temperature.

Manganite and other materials

The perovskite system of manganite $R_{1-x}M_x\text{MnO}_3$ has a moderate magnetocaloric effect (MCE), mechanical and chemical stability, and high electrical resistance[48]. Iron-based amorphous alloys have a relatively large MCE due to SOMT and tuneable TC around room temperature but a low ΔT_{ad} value. Fe-Rh alloys exhibit a giant field-induced first-order magnetic transition (FOMT) and huge ΔT_{ad} but have large hysteresis, limiting their MCE performance[49]. A dual-stimulus magnetic-electric refrigeration cycle in FeRh thin films coupled with a ferroelectric BaTiO₃ substrate aimed to overcome the irreversibility problem[50]. However, the high cost of Rh still poses a severe disadvantage for large-scale application.

1.5.2 Order of phase transition

The phase transition order is an important factor to assess the MCE materials' performance. First Order Magnetocaloric phase Transition (FOMT) Materials have a large MCE over a small temperature window, while second Order Magnetocaloric phase Transition (SOMT) materials have a mild MCE over a wide temperature range. The FOMT can be defined by the discontinuity in the thermodynamic Gibbs free energy derivative [51]. The differences between the two types of phase transition for the entropy S , magnetization M , volume V , heat capacity C_p and entropy change ΔS are shown in Fig. 1.5.

One of well agreed method for distinguish the order of magnetic phase transition is: if the fourth-order coefficient of the Landau expansion is negative, then it results in a negative slope of the Arrott plot. As per the Banerjee criterion, a negative value of the fourth-order coefficient of the Landau expansion indicates a first-order magnetic transition[5], while a positive slope indicates a second-order magnetic transition[52]. The Arrott plots are widely used to determine the type of magnetic phase transition, using the isothermal magnetization (M - H) curves.

Clearly, the FOMT materials have a higher ΔS and a sharper dM/dT , but they also have a volume change and a big thermal hysteresis, which can compromise the structural stability and the thermal dynamic cycle. The FOMT materials can be classified into two groups: a magneto-structured transition and a magneto-elastic transition. The magneto-structured transition changes the lattice symmetry, which occurs in the Gd-Ge-Si,[62] Mn-(Co,Ni)-(Ge,Si),[63] and Ni-Mn-In Heusler alloys.[64] The magneto-elastic transition does not change the lattice symmetry during the phase transition, which happens in the La-Fe-Si,[65] Mn-Fe-P-Si [66] and Fe-Rh alloys. [67] the SOMT materials on the other hand, has a much lower ΔS a bord and flat dM/dT curve, which means they can be used in a wide temperature window. Moreover, they usually good structural stability and no hysteresis. One good example of SOMT MCM is gadolinium (Gd).

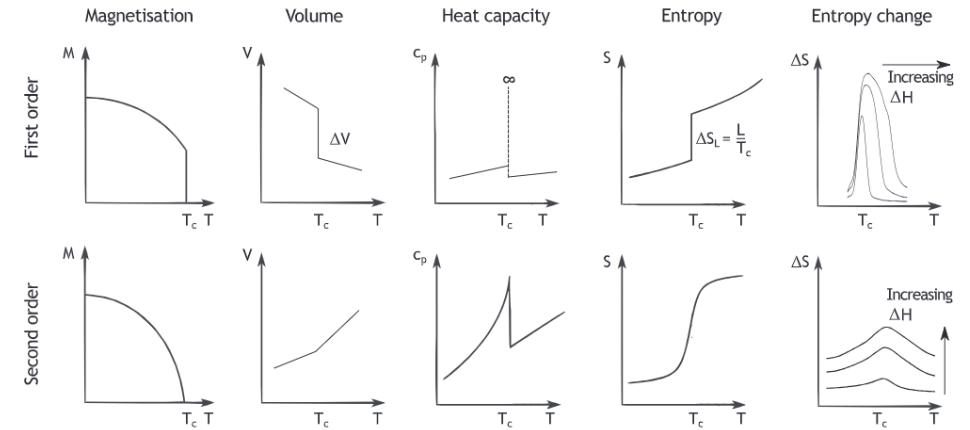


Figure 1.5: The entropy S , magnetization M , the volume V , the heat capacity C_p and the entropy change ΔS for the first order and second order phase transition [53].

1.5.3 Figure of merit for MCMs

In order for magnetic materials to be used in heating/cooling or energy conversion applications, they must possess certain properties and characteristics. There are many factors which determine if MCMs are interesting for future commercial application on room temperature, but most prominent is the amount of magnetocaloric effect they inhibit in their working temperature span. Based on these, MCM performance criterions like the refrigeration capacity (RC)[54] and the coefficient of refrigerant performance (CRP)[55, 56] has been proposed. However, when implement the MCM in the magnetocaloric device, other important factors have to be taken into consideration[2, 57], which includes:

- low Debye temperature values
- a Curie temperature that is close to the working temperature
- a large temperature change in the vicinity of phase transition
- low thermal or magnetic hysteresis
- low specific heat and high thermal conductivity
- high electrical resistance
- non-toxicity,
- resistance to corrosion
- good mechanical properties
- low manufacturing costs,
- minimal environmental impact

As we can tell, these requirements pose a high bar to the existing MCM/MCM families. Despite the well-developed field of magnetocaloric material, not many materials can fulfill these criteria. This is why up to today, only three types of magnetocaloric materials have been extensively applied in the magnetocaloric device prototypes. They are gadolinium and its compound, La-Fe-Si family and Mn-Fe-P-Si family.

In real application, compromise has to be made in order to utilize the MCMs which are available. A component which accommodates the MCM and make it functional in the magnetocaloric device is called a magnetocaloric heat exchanger or active magnetic regenerator (AMR) in magnetic heat pumps.

1.6 SHAPE OF THE MAGNETOCALORIC MATERIALS

In order to apply integrated the MCM into the thermodynamic cycle of a certain magnetocaloric device, the enabling of heat transfer between the MCM and the other part of the device is essential. Apparently, the MCM has to be shaped with some geometry in mind in order to promote the heat exchange between the HTF and the MCM. The typical MCM geometries that have been applied in the AMR or heat exchangers in magnetocaloric device prototypes are packed bed and parallel plates for their well-established design and shaping techniques. However, recently there are more and more prototypes with microchannel MCM geometry are developed to further improve the heat exchange efficiency [58-61]. We will focus on the use case of geometries based on the study of AMR, because the regenerator in magnetic refrigerator and heat pump are better studied comparing to the magnetocaloric heat exchanger for TMM or TMG.

1. Packed Bed Geometry:

In this type of geometry, the regenerator is filled with magnetocaloric material (MCM) in the form of densely packed irregular particles or spheres. Then bundles them together with epoxy binder or sintering method. The production MCM in the form of irregular particles is much easier comparing to the production of MCM spheres, which requires atomization process with low yield. However, the irregular particles can cost trouble in the bundling process. The irregular particles are difficult to be constrained, which can influence homogeneity of fluid flow and generating debris in presence of structural instability[62]. Therefore, most of current pack bed geometry are using spherical MCMs. After bundling process (especially epoxy bonding), the packed bed has the best structural stability amount these four geometries. However, even for the spherical MCMs, it is still difficult to make a homogeneous porous structural due to the inconsistency of binding or sintering process. Therefore, the actual performance results of packed bed geometry are usually worse than the design value.

In term of performance, the packed bed has the highest heat transfer coefficient thanks to its huge specific surface area, while its also has the highest pressure drop and viscous dissipation among all typical exchanger geometries[61]. Even in theory, the massive thermal loss from the pressure drop and viscous dissipation drag down the performance of the pack bed, makes it under perform other three geometries under similar conditions.

2. Parallel Plate Geometry:

Regenerators of this geometry involve the use of stacked thin plates of MCMs separated by spacers to provide regular flow channels for HTF. The MCM plates are typically shaped using traditional techniques like wire sawing, C&C milling, and mold casing. However, the technique has to be selected specifically to fit the mechanical and magnetocaloric properties of the target MCMs. Then, in the stacking process these thin plates are bundled together by epoxy bonding with plastic spacers or by simply welding at specially designed edges [63, 64]. Thanks to the decent precision of tradition shaping techniques, the dimensional specifications of the plates and the channels of this geometry type is the highest amount all four geometries. The difficulty of this geometry comes to the implementation. There is a delicate balance between the thickness of the plate and the its structural stability, especially in the presence of the magnetic force which is a variant differs from case to case. Moreover, it is very difficult to increase the specific surface area of the parallel plate geometry as the plate is quite bulky for a building element comparing to the ones like particles or fibers in other geometries.

In term of performance, the parallel plate geometry has the lowest pressure drop amount other geometries thanks to its simple, regular and smooth flow channels[59]. However, it also has the lowest heat transfer coefficient due the lack of specific surface area.

3. Micro-Channel Geometry:

This design involves the use of small, sub-millimeter hydraulic diameter porous structures, put them into an ordered-clustered block, and repeating this process to fill a compartment (usually AMRs) with these blocks. MCMs are not easy to be shaped due to the phase-transition induced structural instability. Therefore, the production method has to take into account not only the MCE, the flow dynamics but also the structural reinforcement. These new approaches come out of unique designs and techniques that are varying from case to case, each case tried to address the challenges with a different theory, this is also why micro-channel geometries have only various types of topologies. The prototype development of AMR with Micro-Channel Geometry is still in the early phase, there is not much systematic performance data available. Liang et al. fabricated regenerator with Micro-Channel geometry using freeze-casting method[65]. The process involves freezing a slurry of the magnetocaloric material and a liquid, then sublimating

the frozen liquid to leave behind a porous ceramic structure with well-defined micro-channels, as shown in Fig. 1.6(a). Navickaitė et al prepared and tested a type of micro-channel regenerator via three dimensional selective laser beam melting technique[66], see in Fig. 1.6(b) During EU-funded MicroChMag project, Liang et al also prepared and analyzed another type of micro-channel regenerator which consists aligned triangular patterns[67], see Fig. 1.6(c). Funk et al shaped LaFeCoSi MCM with powder-in-tube (PIT) technology, where the MCE powders were clad by a 100 μm thick seamless austenitic steel jacket [68], as shown in Fig. 1.6(d). In 2022, Magneto B.V. in the Netherlands developed an extrusion-based 3D printed fiber mesh structural (Fig. 1.6 e)), which has fully customizable pack-screen bed liked cross suction, the fiber thickness can be adjusted from 600 μm to 200 μm .

1.7 OTHER MAIN COMPONENTS OF A MAGNETOCALORIC DEVICE

1.7.1 Magnetic field source

There are three main types of magnets that can be used to generate the magnetic field in such a device: superconducting magnets, electromagnets and permanent magnets. All three types of magnets have been explored in the development of magnetocaloric devices. There is no champion of magnet for all magnetocaloric application, only most suitable type will be popular in certain application scenarios.

A superconducting magnet is an electromagnet that uses a coil of superconducting material, which has zero electrical resistance when cooled below a certain critical temperature. This allows the coil to carry very high currents and produce very high magnetic fields without dissipating heat or energy. A superconducting magnet can achieve fields of several Tesla, which can enhance the magnetocaloric effect of some MCM with high saturation magnetization. However, a superconducting magnet also requires a cryogenic system to maintain its low temperature, which adds to the complexity and cost of the device. Moreover, a superconducting magnet is sensitive to external disturbances that can cause a loss of superconductivity, known as quenching, which can damage the coil or the magnetocaloric material. This can be an issue in application with durability/reliability requirement. Superconducting magnets are mostly applied in the early development of the magnetocaloric devices, or for gas liquefier niche. An latest example of a magnetocaloric device using a superconducting magnet is the one reported by Kamiya et al [69], a 5 T superconducting coil has been applied to achieve a minimum temperature of 18.5 K and a cooling capacity of 1.2 W at 20 K.

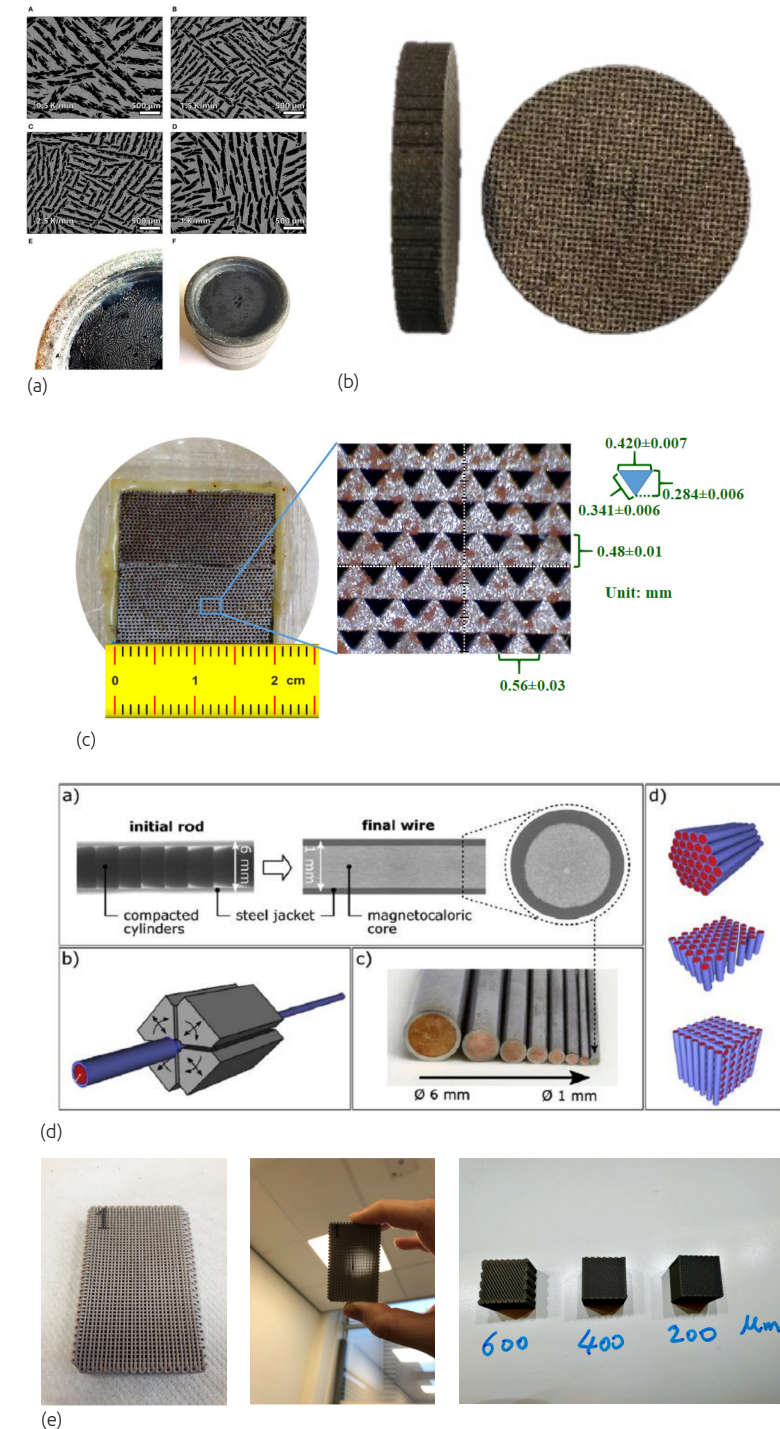


Figure 1.6: various magnetocaloric material heat exchanger prototypes with microchannel geometry

An electromagnet is an electric circuit that uses a coil of conventional conductive material, such as copper wire and iron core, which has a finite electrical resistance. This means that the coil generates heat and consumes energy when carrying current and producing magnetic field. An electromagnet can achieve fields of around one tesla, depending on the size and design of the coil. An electromagnet has the advantage of being able to control the magnetic field by varying the current, which can optimize the performance of the device [70]. Besides, the ability of varying the field without any moving part makes a more durable and quieter machine possible. However, an electromagnet also has the disadvantage of having high power consumption and heat generation, which reduces the efficiency and increases the cooling load of the device. As a solution of this issue, Urban et al [71] reported an electro-permanent magnet field source achieved over 80% energy efficiency and up to 50 Hz operating frequency with magnetic energy recovery. A permanent magnet is a magnet that uses a material that has a permanent magnetic moment, such as neodymium or samarium-cobalt alloys, which do not require electric current or cooling to maintain their magnetic field. A permanent magnet can achieve fields of up to 2 Tesla, depending on the grade of the permanent magnet and the geometry of the magnet assembly. A permanent magnet has the advantage of being robust, compact and energy-efficient, as it does not require any power supply or cooling system to function. However, a permanent magnet also has the disadvantage of having a fixed magnetic field, which cannot be adjusted or switched off, which limits the flexibility and safety of the device. Despite the disadvantages, the permanent magnet has been the most applied in room magnetocaloric applications. Bjørk et al [72] and Teyber et al [73] compared different designs of permanent magnetic field source for magnetic refrigeration from both performance and cost aspects.

1.7.2 Heat transfer fluid

Heat transfer fluids (HTFs) are important in magnetocaloric heat pumps (MHPs). These heating and cooling systems move heat from cold to hot environments by using the MCE of the MCMs. HTFs help transfer heat between the MCMs and the heat exchangers that connect to the cold and hot reservoirs. Choosing the right HTF depends on different factors. This includes the working temperature range, thermal conductivity, viscosity, compatibility with the MCMs and the system components, and environmental impact. Different HTFs have been tested for MHP applications, such as water, water-ethylene glycol mixtures, nanofluids, and liquid metals.

Water is commonly used as an HTF for MHPs operating near room temperature because it has high specific heat capacity, low viscosity, and low environmental impact. However, water has some drawbacks such as low thermal conductivity (only around $0.6 \text{ Wm}^{-1}\text{K}^{-1}$), high freezing point, and possible corrosion effect on some MCMs. Therefore, a mixture of water and antifreeze with corrosion inhibitors is typically used as the heat transfer

fluid in magnetic regenerators[74].

Water-ethylene glycol mixtures can be used to lower the freezing point and increase the thermal conductivity of water. Depending on the mixing ratio, the low end of its working temperature range can be as low as -50°C . However, they also increase the viscosity and reduce the specific heat capacity, especially at low temperature[75, 76].

Nanofluids are fluids with nanoparticles of different materials suspending in, such as metals or oxides. These nanoparticles enhance the thermal conductivity and the heat transfer coefficient of the base fluid. And a high thermal conductivity value will keep the entropy production rate low for a given heat power and mean temperature, this will improve the heat transfer efficiency of HTF. Nanofluids have been shown to improve the performance of MHPs in some cases. However, they also present some challenges, such as the stability, dispersion, and cost of the nanoparticles.

liquid metals like mercury, sodium-potassium (NaK), and GaInSn alloys have superior thermal properties and no risk of corrosion to the MCMs. However, their huge density makes it very hard to pump in the hydraulic loop, and the induced surface pressure on MCM cast big challenge on their durability. As one possible solution, Rajamani et al[77] developed a magnetic pump to drive the liquid metal with low frequency and low power consumption.

1.7.3 Control system

There are two major types of control systems applies to magnetocaloric devices: active and passive. An active control system employs a computer or MCU (Microcontroller Unit) assisted solenoid valve array to adjust the working cycle. This system offers more flexibility and control, making it ideal for experimental purposes. However, it also comes with higher energy consumption and cost implications.

On the other hand, a passive control system employs a mechanical valve array that synchronizes with the magnetic field to control the working cycle. This system is less flexible, but it is less complex and consumes less energy. As a result, it is preferred for commercial application where low cost and reliability are more important than flexibility. In summary, the choice between these two depends on the specific needs of the application. While an active control system may be more suitable for research and development purposes, a passive control system is often a better choice for commercial applications where efficiency and reliability are the top priorities.

1.8 PROTOTYPES OF MAGNETOCALORIC DEVICES

Magnetocaloric materials (MCMs) exhibiting a giant MCE significantly change their temperature when exposed to a changing magnetic field as shown in Fig. 1.7. Therefore, MCMs can be incorporated into thermodynamic cycles to pump heat from a reservoir temperature to an elevated temperature and vice versa either with the purpose of cooling or heating (Fig. 1.7, left). In an inverted cycle, cooling or heating across the magnetic phase transition activates or deactivates the magnetic state, which can be used to convert heat into mechanical energy or electrical energy (Fig. 1.7, right). Note that the MCE and energy conversion efficiency are maximal close to the magnetic phase transition, which is defined by the so-called Curie temperature (T_c). When the temperature crosses T_c the MCM switches between magnetic (below T_c) and non-magnetic state (above T_c). Therefore, the working temperature range of a MCM depends on its T_c .

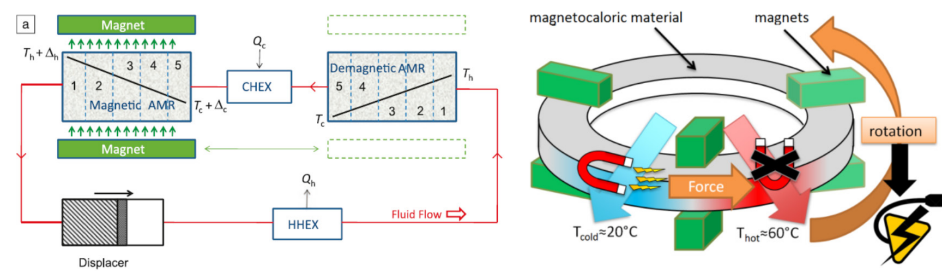


Figure 1.7: System schematics for magnetocaloric heat pump and thermomagnetic motor

The major difference between magnetocaloric heat pump and magnetocaloric energy converter is with or without regeneration cycle. Basically, in order to achieve high energy efficiency, the heat pump applications have to follow certain thermodynamic cycle to reuse a part of energy that stored in the system. However, this doesn't apply to the ADR cycle in cryogenic cooling and magnetocaloric power conversion, both applications are using a non-generative working cycle.

1.8.1 Magnetocaloric refrigerators and magnetocaloric heat pumps

The device makes use of the AMR to cool a certain space is usually called a magnetic refrigerator or magnetic cooler, while a device uses the AMR to heat a space is usually called a magnetic heat pump. In fact, the as introduced in section 1.5, the working principle of both application is to utilize the thermodynamic cycle to transfer the heat from one space to another, i.e. a heat pumping process. There are many of this kind of devices have been developed since the discovery of the MCE. Based on the application temperature

range, we can classify them into three categories: the cryogenic application, the room temperature application, and the heating application. Since the cryogenic application is not the focus of this work, and heating application has very few prototypes developed up to now, we will focus on the room temperature cooling/refrigeration application.

Room temperature application

After discovering the marvellous magnetocaloric property of gadolinium, which has its Curie temperature round 18°C , a wave of room temperature magnetocaloric refrigerator/cooler prototypes has been developed.

First generation devices: These devices used superconducting magnets and low-frequency operation. They were mainly based on Stirling or Brayton cycles with passive or active regeneration. Some examples are Brown et al. (1976)[4], Steyert (1978)[78], Barclay (1994)[79], and Zimm et al. (2003)[80]. The purposes of the research work in this period mainly focus on the proof-of-principle devices in which the function is the priority instead of the performance. These devices and work are well documented by many reviews like [81-83].

Second generation devices start mainly after the year 2000: These devices used permanent magnets and higher-operation frequency. They were mostly rotary devices with concentric Halbach cylinders/arrays or complicated magnet assemblies. These prototypes also implemented well-designed hydraulic system which insisted either passive or active valve systems to gain better control on the magnetocaloric working cycle. The purposes of the research work in this period mainly focus on the application and performance of these magnetocaloric refrigerator/heat pump. In the following section, we focus on the introduction of the second-generation prototypes.

There are two groups of devices, i.e., the ones operating in a reciprocating (linear motion) manner and the others operating in a rotary manner. The reciprocating and rotary operations of the magnetocaloric device are more or less related to the way how the AMR is exposed to the alternating magnetic field. This is a widely used classification principle of the magnetocaloric refrigerator/heat pumps.

Tura and Rowe (2011)[84] introduced PM-I, a rotary device with a magnetic field source based on permanent magnets that produced a maximum temperature span of 29 K and a maximum cooling power of 50 W. In 2014, the same group presented a new work PM-II[85], which provided a maximum temperature span of 33 K and a maximum cooling power of 2.5 W. Engelbrecht et al. (2011)[86] provided detailed experimental tests on their first prototype, which produced a maximum temperature span of 10.2 K under no-load conditions with gadolinium. In 2012, the same group introduced a rotary

regenerator refrigerator device that produced a maximum temperature span of 25.4 K under zero cooling load[87]. Lozano et al. (2014)[88] demonstrated that the device could produce 1 kW as cooling power. In 2015, Eriksen et al. (2015) [89] announced the building of a third prototype, a rotary refrigerator - MAGGIE, with a maximum magnetic field of 1.4 T for commercial refrigeration. This prototype obtained a maximum coefficient of performance (COP) of 3.6 at 7.2 K and 0.3 W cooling power, while reaches a maximum span of 20 K.

In 2018, MagQueen a magnetocaloric heat pump, was presented by Dall'Olio et al. Johra et al. (2019)[90] further explored the performance of MagQueen for building applications with a maximum operating frequency of 2 Hz and maximum COP of 5. MagQueen is the first develop that achieved kW scale cooling and heating power when used as a heat pump.

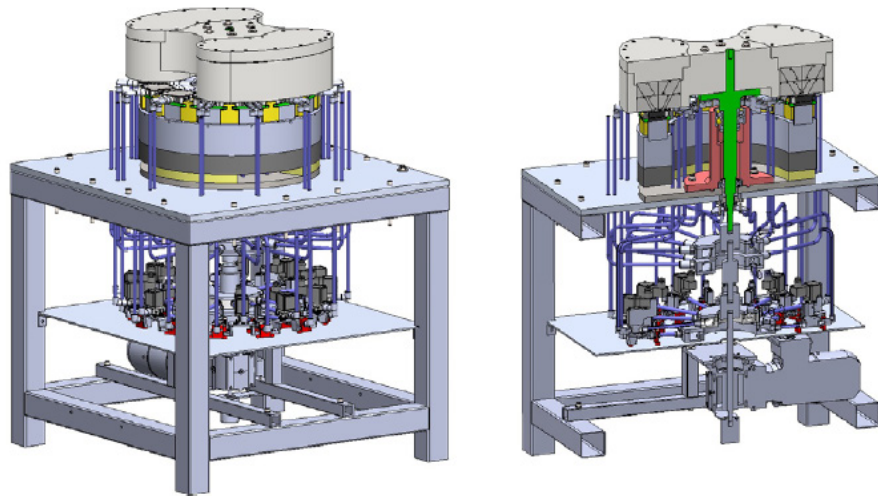


Figure 1.8 The external design and suction view of MagQueen

The Federal University of Santa Catarina research group developed refrigerator prototypes since 2011, which contains parallel-plates regenerator made of gadolinium. They also developed a novel rotary magnetic refrigerator (Lozano et al., 2016)[91] exhibiting a COP of 0.54 with 7.1 K as the maximum temperature span. Trevizoli et al. (2016) reported on a prototype that could reach a maximum cooling power of 53.7 W and a maximum temperature span of 30 K under zero cooling-load, with a COP of 4.6.

Aprea et al. (2014) [92] developed the first Italian rotary device, called 8-Mag, which uses a magnetic system with packed-bed regenerators crossed by distilled water. The device exhibited good performances, producing COP=1.8 under a cooling power of 163W and COP max=2.5 under a cooling load of 200W. In 2015, the device was tested in air-conditioning operation mode, producing 100W in correspondence of 6K and COP=0.6.

In 2013, the University of Coruna developed a magnetocaloric prototype that used permanent magnets[93]. The prototype had two AMR regenerators that were filled with gadolinium plates and flowed with distilled water. The prototype achieved a maximum temperature span of 3.5 K under zero-load conditions, and a specific cooling power of 16.7 W kg^{-1} at zero-temperature span. A year later, the University of Zaragoza built a magnetocaloric device with a magnetic system made of permanent magnets of Nd₂Fe₁₄B in Halbach configuration[94]. The device had a moving packed-bed regenerator filled with gadolinium spheres and was crossed by a mixture of water and ethylene glycol. During no-load tests, the device achieved a maximum temperature span of 19.3 K and had a reference cooling power of 6 W during zero-temperature span investigations. In 2014, Czernuszewicz et al from Wroclaw University of Technology introduced a magnetocaloric test stand that mounted a Halbach array of permanent magnets[95]. The magnets magnetized an AMR packed-bed regenerator made of gadolinium within an ethane-diol mixture. The device achieved a maximum temperature span of 6.9 K.

Also in 2014, Jacobs designed a rotary magnetic refrigeration system [96] for Astronautics Corporation of America based on permanent magnets. The system had 21 static regenerators assembled with LaFeSiH alloys and connected by water circuit. The magnetic prototype achieved a reference cooling power of 3042 W during zero-temperature span investigations and a promising cooling power of 2502 W at a temperature span of 11 K.

The KTH Royal Institute of Technology from Sweden introduced a prototype device with a rotating magnet system made of LaFeMnSiH and a packed bed AMR with 12 static irregular-shaped regenerators. The researchers investigated the prototype with only two of the regenerators filled and found a temperature span of around 18 K, with a flow rate of $8.3 \times 10^{-6} \text{ m}^3\text{s}^{-1}$ and working frequency of 0.5 Hz[97]. The Baotou Research Institute of Rare-earths from China presented a magnetic cabinet prototype for wine storage using two concentric Halbach array permanent magnets and a multi-layer AMR made of Gd and GdEr alloy particles[98]. They used demineralized water as the HTF and achieved a maximum temperature span of 25 K at zero-load while operating at the optimal frequency of 2 Hz and volumetric flow rate of 5.3 l min^{-1} .

One of the companies that have been actively involved in this field is Cooltech Application Company, which has developed various prototypes of magnetocaloric devices over the years. Their first prototype, a reciprocating AMR, was patented in 2009. In 2011, the company launched their second reciprocating device, which was made with Nd-Fe-B permanent magnets ($B = 1.27$ T) and was able to operate up to 1.5 Hz. This device mounted a parallel-plate AMR that was assembled with Gd and Gd-Tb and achieved a maximum heat load of 150 W and a maximum temperature span of 38 K. In subsequent years, Cooltech Application Company continued to develop their magnetocaloric devices. In 2013, they introduced their first rotary permanent magnets magnetic prototype ($B = 0.98$ T) that could reach 4 Hz by rotating on packed bed regenerators made with Gd or Gd-Tb[99]. This device produced a maximum temperature span of 42 K and a maximum heat load of 120 W. In 2014, the company introduced their second rotary prototype ($B = 1.17$ T), which mounted parallel-plates regenerators and was tested with Gd, Gd-Er/La-Fe-Si. This prototype achieved a maximum temperature span of 38 K and a maximum heat load of 300 W. The latest updates about Cooltech Application Company's magnetocaloric devices were presented by Lionte et al. (2018) [100, 101] during Thermag VIII. They introduced a rotary device that was designed for a possible replacement of Gd-based with LaFeSi-based alloys. The prototype had three thermal loops and a hydraulic system moved by an external pump. The magnetic system was made of permanent magnets ($B = 1$ T), and the device could operate between $f = 0.5$ -2 Hz and variable flow rates 1-6 l min⁻¹. During initial investigations, the prototype produced a maximum temperature span of 30.8 K.

To conclude this section, we find a summarizing plot from Kamran et al.[75] to list out the well documented performance data from the existing prototypes.

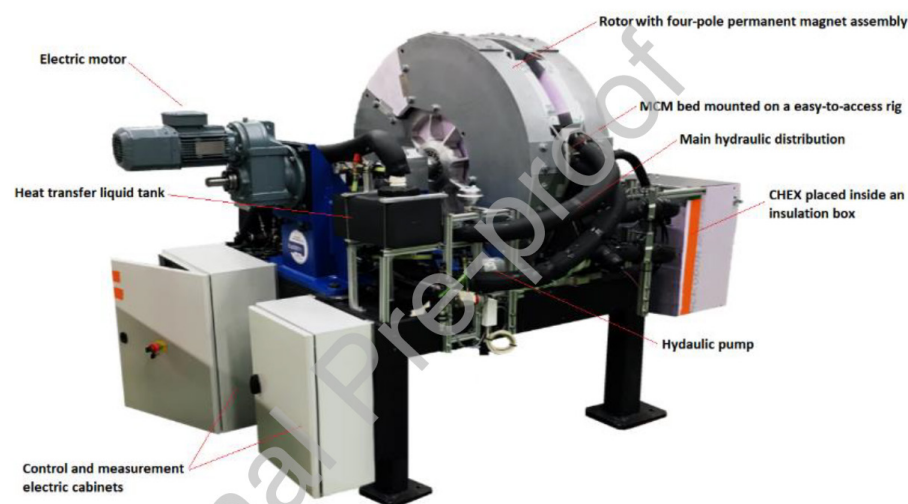


Figure 1.8 The last prototype built by Cooltech Application Company in 2020

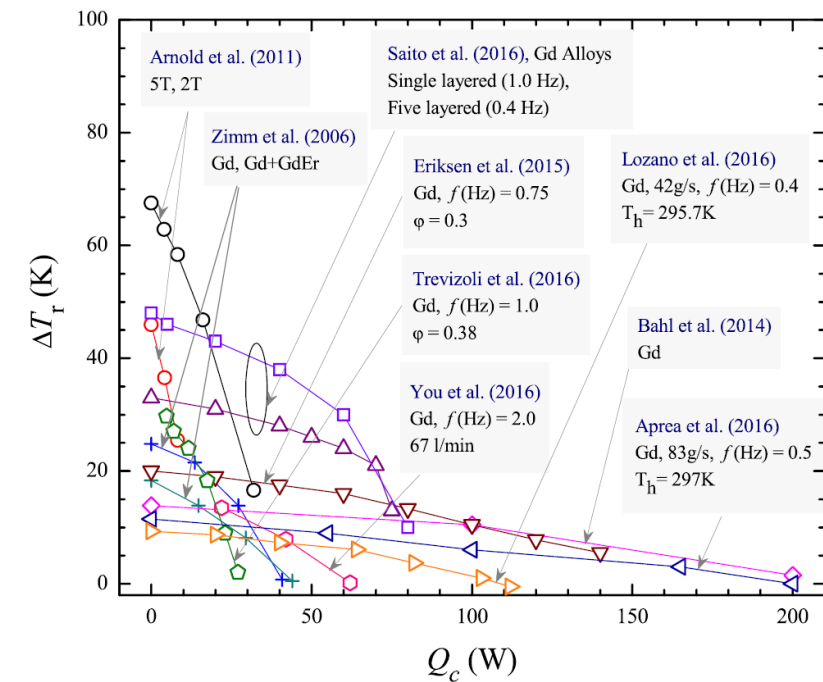


Figure 1.9 The temperature span vs cooling load performance of the magnetocaloric refrigerator prototypes according to data available[75]

1.8.2 Thermomagnetic motors and thermomagnetic generators

Utilizing Magnetocaloric (MC) material, a thermomagnetic generator (TMG) device converts a temperature difference into electrical power via the magnetocaloric effect (MCE) and Faraday law[102]. By changing the temperature of an MC material, which exhibits a large change of magnetization around its Curie temperature (T_c), the magnetic flux flowing through the MC material will also be changed. With this time-varying magnetic flux, an electric voltage can be generated in a coil. This concept results in great flexibility of magnetic circuits and heat transfer mechanisms to optimize the performance of TMGs. Gueltig et al. developed a TMG with resonant self-actuation, which uses thin films of Heusler alloys that vibrate resonantly due to the alternating magnetization and heat transfer. This design is the first implementation of TMG at miniature length scales (mm to cm-range) [103]. Liu et al. proposed an innovative design that uses a magnetocaloric switch, which controls the magnetic circuit by changing the reluctance of the parallel paths. The electrical power density per degree of temperature difference of this device is by 2 to 3 orders of magnitude higher than those of other active TMGs, and also much higher than existing TE and PE devices [104]. Although TMGs are proven to have higher efficiency than thermoelectric generators at small temperature differences and have

higher power density than pyroelectric generators, TMGs still face some challenges, such as the need for high-quality magnetic materials, reliable heat transfer systems, and effective magnetic shielding.

Another category of thermomagnetic device works with an indirect conversion method, which converts thermal energy first into other form of energy (mostly kinetic energy such as rotation, reciprocation, or swing), and then further converts into electricity with some additional device such as an electrical generator. Devices falling into this category are usually called thermomagnetic motor (TMM) or thermomagnetic actuator (TMA). A TMM converts thermal energy into mechanical energy in the form of rotational motion. The motor typically consists of a rotor with a soft magnetic material and a stator containing permanent or electrically driven magnets. When a temperature gradient is applied across the rotor, it creates a magnetization gradient across the rotor in response to the magnetic field generated by the stator, causing it to rotate. This rotation can be used to generate electrical power or perform mechanical work.[105] A TMA is a device that converts thermal energy into mechanical energy in the form of linear motion. The actuator typically consists of a soft magnetic core surrounded by a solenoid coil or a ring of permanent magnet. When a temperature gradient is applied across the core, it moves in a linear motion in response to the changing magnetization state. This linear motion is usually used for precision control or triggering mechanism[106, 107]. Both TMA and TMM can be used to convert low-temperature waste heat in the range from 35°C up to 100 °C from a wide range of heat sources into electricity.

Although TMMs have some disadvantages compared to TMAs, such as lower efficiency, bulky design, and limited precision[108], TMMs still represent the most promising approach for unlocking ultra-low-temperature heat as energy source for future zero-emission electricity supply. TMMs are among the best available alternatives for environmentally friendly thermal energy harvesting system [24]. The earliest development of the TMM is when Thomas Alva Edison and Nikola Tesla patented the first designs with the “Pyromagnetic Generator” (US patent 476,983, Thomas Alva Edison, 1888) and the “Thermo-Magnetic Motor” (US patent 396,121, Nikola Tesla, 1889), but none of them have built the device due to a lack of suitable material. After that, in 1972 Murakami and Nemoto[105] developed the first TMM prototype. The development had paused quite a while since there is no “temperature sensitive magnetic material” that can fill the gap. Then in 1997, with the discovery of room temperature Giant Magnetocaloric Effect (GMCE)[21], the development on TMM again started to move forward. From then on, several prototypes with various designs have been presented[109-111]. At Swiss Blue Energy AG, with 1 kW power output, the TMM prototype has almost reached industrial scale[112]. In 2022, Hey et al. [113] developed a TMM prototype with 88 W output power and 2.1% energy conversion efficiency, which marks the highest energy efficiency up-to-date.

1.9 THE SCOPE OF THE DISSERTATION

Throughout my PhD research, I delved deeply into the intricacies of magnetocaloric technology and its diverse applications. My focus centered on the development of magnetocaloric heat pumps and thermomagnetic motors, which represent highly efficient and eco-friendly technologies that can be utilized for refrigeration and power generation purposes. To maximize the performance of these systems, I integrated my knowledge of system engineering and material shaping techniques and devised innovative approaches to optimize the performance of magnetocaloric devices and materials under varying operating conditions. In pursuit of this goal, I conducted extensive experiments and simulations to analyze the system efficiency over variety of temperature spans, and applying optimizations on both the structural and controlling aspect of magnetocaloric devices. The outline of this dissertation is as following:

Chapter 2: explains experimental method and measurement techniques

Chapter 3: introduces the design, implementation and performance analysis of a reciprocating magnetocaloric refrigerator prototype -- MMFF Cooler.

Chapter 4: introduces the design, implementation and performance analysis of a rotary magnetocaloric heat pump prototype – FAME Cooler. Further performance optimization on FAME Cooler also included in this chapter.

Chapter 5: changes the focus to waste energy harvesting device. A thermomagnetic motor prototype (TMM0) is introduced, and followed up with a numerical modelling exploration for improving the system performance of TMM0.

REFERENCES

- [1] A. Smith, Who discovered the magnetocaloric effect?, *European Physical Journal H*, 38 (2013) 507-517.
- [2] B. Yu, M. Liu, P.W. Egolf, A. Kitanovski, A review of magnetic refrigerator and heat pump prototypes built before the year 2010, *International Journal of Refrigeration*, 33 (2010) 1029-1060.
- [3] W. Giauque, D. MacDougall, The production of temperatures below one degree absolute by adiabatic demagnetization of gadolinium sulfate, *Journal of the American Chemical Society*, 57 (1935) 1175-1185.
- [4] G.V. Brown, Magnetic Heat Pumping near Room-Temperature, *Journal of Applied Physics*, 47 (1976) 3673-3680.
- [5] A. Fujita, Y. Akamatsu, K. Fukamichi, Itinerant electron metamagnetic transition in La (Fe x Si 1– x) 13 intermetallic compounds, *Journal of Applied Physics*, 85 (1999) 4756-4758.
- [6] E. Brück, O. Tegus, X.W. Li, F.R. de Boer, K.H.J. Buschow, Magnetic refrigeration—towards room-temperature applications, *Physica B: Condensed Matter*, 327 (2003) 431-437.
- [7] V.K. Pecharsky, K.A. Gschneidner Jr, Magnetocaloric effect and magnetic refrigeration, *Journal of Magnetism and Magnetic Materials*, 200 (1999) 44-56.
- [8] N.A. de Oliveira, P.J. von Ranke, Theoretical aspects of the magnetocaloric effect, *Physics Reports*, 489 (2010) 89-159.
- [9] A.S. Arrott, Approximations to Brillouin functions for analytic descriptions of ferromagnetism, *Journal of Applied Physics*, 103 (2008).
- [10] V.K. Pecharsky, K.A. Gschneidner, Jr., Some common misconceptions concerning magnetic refrigerant materials, *Journal of Applied Physics*, 90 (2001) 4614-4622.
- [11] M. Foldeski, W. Schnelle, E. Gmelin, P. Benard, B. Koszegi, A. Giguere, R. Chahine, T.K. Bose, Comparison of magnetocaloric properties from magnetic and thermal measurements, *Journal of Applied Physics*, 82 (1997) 309-316.
- [12] Y.I. Spichkin, V.K. Pecharsky, K.A. Gschneidner, Jr., Preparation, crystal structure, magnetic and magnetothermal properties of (GdxR5–x)Si4, where R=Pr and Tb, alloys, *Journal of Applied Physics*, 89 (2001) 1738-1745.
- [13] A.M. Tishin, Y.I. Spichkin, *The magnetocaloric effect and its applications*, CRC Press, 2016.
- [14] S. Jeong, AMR (Active Magnetic Regenerative) refrigeration for low temperature, *Cryogenics*, 62 (2014) 193-201.
- [15] J. Romero Gómez, R. Ferreira Garcia, A. De Miguel Catoira, M. Romero Gómez, Magnetocaloric effect: A review of the thermodynamic cycles in magnetic refrigeration, *Renewable and Sustainable Energy Reviews*, 17 (2013) 74-82.
- [16] P. Govindappa, P.V. Trevizoli, O. Campbell, I. Niknia, T.V. Christiaanse, R. Teyber, S. Misra, M.A. Schwind, D. van Asten, L. Zhang, A. Rowe, Experimental investigation of MnFeP1–xAsx multilayer active magnetic regenerators, *Journal of Physics D-Applied Physics*, 50 (2017).
- [17] K. Navickaitė, H.N. Bez, T. Lei, A. Barcza, H. Vieyra, C.R. Bahl, K. Engelbrecht, Experimental and numerical comparison of multi-layered La (Fe, Si, Mn) 13Hy active magnetic regenerators, *International Journal of Refrigeration*, 86 (2018) 322-330.
- [18] D. Pineda Quijano, C. Infante Ferreira, E. Brück, Layering strategies for active magnetocaloric regenerators using MnFePSi for heat pump applications, *Applied Thermal Engineering*, 232 (2023) 120962.
- [19] I. Park, S. Jeong, Experimental investigation of 20 K two-stage layered active magnetic regenerative refrigerator, *IOP Conference Series: Materials Science and Engineering*, 101 (2015) 012106.
- [20] T. Gottschall, K.P. Skokov, M. Fries, A. Taubel, I. Radulov, F. Scheibel, D. Benke, S. Riegg, O. Gutfleisch, Making a Cool Choice: The Materials Library of Magnetic Refrigeration, *Advanced Energy Materials*, 9 (2019) 1901322.
- [21] V.K. Pecharsky, K.A. Gschneidner, Giant magnetocaloric effect in Gd-5(Si2Ge2), *Physical Review Letters*, 78 (1997) 4494-4497.
- [22] X. Hou, L. Shitao, Z. An, X. Hui, J. Ni, B. Zhou, Research for magnetocaloric effect of Gd1–xDyx alloy, *physica status solidi c*, 4 (2007) 4564-4568.
- [23] M. Balli, D. Fruchart, D. Gignoux, E. Hlil, S. Miraglia, P. Wolfers, Gd1– xTbx alloys for Ericsson-like magnetic refrigeration cycles, *Journal of Alloys and Compounds*, 442 (2007) 129-131.
- [24] Z. Xu, G. Lin, J. Chen, A GdxHo1– x-based composite and its performance characteristics in a regenerative Ericsson refrigeration cycle, *Journal of Alloys and Compounds*, 639 (2015) 520-525.
- [25] A.T. Saito, T. Kobayashi, S. Kaji, J. Li, H. Nakagome, Environmentally friendly magnetic refrigeration technology using ferromagnetic Gd alloys, *International Journal of Environmental Science and Development*, 7 (2016) 316.
- [26] T. Palstra, G. Nieuwenhuys, J. Mydosh, K. Buschow, Mictomagnetic, ferromagnetic, and antiferromagnetic transitions in La (Fe x Al 1– x) 13 intermetallic compounds, *Physical Review B*, 31 (1985) 4622.
- [27] A. Fujita, S. Fujieda, Y. Hasegawa, K. Fukamichi, Itinerant-electron metamagnetic transition and large magnetocaloric effects in La (Fe x Si 1– x) 13 compounds and their hydrides, *Physical Review B*, 67 (2003) 104416.
- [28] M. Balli, M. Rosca, D. Fruchart, D. Gignoux, Effect of interstitial nitrogen on magnetism and entropy change of LaFe11. 7Si1. 3 compound, *Journal of Magnetism and Magnetic Materials*, 321 (2009) 123-125.
- [29] Y.-f. Chen, F. Wang, B.-g. Shen, J.-r. Sun, G.-j. Wang, F.-x. Hu, Z.-h. Cheng, T. Zhu, Effects of carbon on magnetic properties and magnetic entropy change of the LaFe 11.5 Si 1.5 compound, *Journal of Applied Physics*, 93 (2003) 6981-6983.
- [30] A. Saito, T. Kobayashi, H. Tsuji, Magnetocaloric effect of new spherical magnetic refrigerant particles of La (Fe1– x– yCoxSiy) 13 compounds, *Journal of Magnetism and Magnetic Materials*, 310 (2007) 2808-2810.
- [31] S. Fujieda, A. Fujita, K. Fukamichi, Large magnetocaloric effects in NaZn13-type La (FexSi1– x) 13 compounds and their hydrides composed of icosahedral clusters, *Science and Technology of Advanced Materials*, 4 (2003) 339-346.
- [32] E. Brück, O. Tegus, L. Zhang, X. Li, F. De Boer, K. Buschow, Magnetic refrigeration near room temperature with Fe2P-based compounds, *Journal of Alloys and Compounds*, 383 (2004) 32-36.
- [33] D. Cam Thanh, E. Brück, O. Tegus, J. Klaasse, T. Gortenmulder, K. Buschow, Magnetocaloric effect in MnFe (P, Si, Ge) compounds, *Journal of Applied Physics*, 99 (2006).
- [34] N. Trung, J. Klaasse, O. Tegus, D.C. Thanh, K. Buschow, E. Brück, Determination of adiabatic temperature change in MnFe (P, Ge) compounds with pulse-field method, *Journal of Physics D: Applied Physics*, 43 (2009) 015002.
- [35] D. Cam Thanh, E. Brück, N. Trung, J. Klaasse, K. Buschow, Z. Ou, O. Tegus, L. Caron, Structure, magnetism, and magnetocaloric properties of MnFeP1– xSix compounds, *Journal of Applied Physics*, 103 (2008).
- [36] N.H. Dung, L. Zhang, Z. Ou, E. Brück, From first-order magneto-elastic to magneto-structural transition in (Mn, Fe) 1.95 P0. 50Si0. 50 compounds, *Applied Physics Letters*, 99 (2011).
- [37] F. Guillou, H. Yibole, N. Van Dijk, E. Brück, Effect of boron substitution on the ferromagnetic transition of MnFe0. 95P2/3Si1/3, *Journal of Alloys and Compounds*, 632 (2015) 717-722.
- [38] N. Thang, H. Yibole, X. Miao, K. Goubitz, L. Van Eijck, N. Van Dijk, E. Brück, Effect of Carbon Doping on the Structure and Magnetic Phase Transition in (Mn, Fe 2 (P, Si)), *Jom*, 69 (2017) 1432-1438.
- [39] N. Thang, X. Miao, N. Van Dijk, E. Brück, Structural and magnetocaloric properties of (Mn, Fe) 2 (P, Si) materials with added nitrogen, *Journal of Alloys and Compounds*, 670 (2016) 123-127.
- [40] N.V. Thang, N.H.v. Dijk, E. Brück, Tuneable giant magnetocaloric effect in (Mn, Fe) 2 (P, Si) materials by Co-B and Ni-B co-doping, *Materials*, 10 (2016) 14.
- [41] Z. Ou, N. Dung, L. Zhang, L. Caron, E. Torun, N. Van Dijk, O. Tegus, E. Brück, Transition metal substitution in Fe2P-based MnFe0. 95P0. 50Si0. 50 magnetocaloric compounds, *Journal of Alloys and Compounds*, 730 (2018) 392-398.
- [42] P. Govindappa, P. Trevizoli, O. Campbell, I. Niknia, T. Christiaanse, R. Teyber, S. Misra, M. Schwind, D. Van Asten, L. Zhang, Experimental investigation of MnFeP1– xAsx multilayer active magnetic regenerators, *Journal of Physics D: Applied Physics*, 50 (2017) 315001.
- [43] T. Christiaanse, P. Trevizoli, S. Misra, C. Carroll, D. van Asten, L. Zhang, R. Teyber, P. Govindappa, I. Niknia, A. Rowe, Experimental study of 2-layer regenerators using Mn–Fe–Si–P materials, *Journal of Physics D: Applied Physics*, 51 (2018) 105002.
- [44] T. Krenke, E. Duman, M. Acet, X. Moya, L. Mañosa, A. Planes, Effect of Co and Fe on the inverse magnetocaloric properties of Ni-Mn-Sn, *Journal of Applied Physics*, 102 (2007).
- [45] M. Ghorbani Zavareh, C. Salazar Mejía, A. Nayak, Y. Skourski, J. Wosnitzer, C. Felser, M. Nicklas, Direct measurements of the magnetocaloric effect in pulsed magnetic fields: The example of the Heusler alloy Ni50Mn35In15, *Applied Physics Letters*, 106 (2015).
- [46] J. Liu, T. Gottschall, K.P. Skokov, J.D. Moore, O. Gutfleisch, Giant magnetocaloric effect driven by structural transitions, *Nature Materials*, 11 (2012) 620-626.
- [47] S. Singh, L. Caron, S.W. D'Souza, T. Fichtner, G. Porcari, S. Fabbrici, C. Shekhar, S. Chadov, M. Solzi, C. Felser, Large Magnetization and Reversible Magnetocaloric Effect at the Second-Order Magnetic Transition in Heusler Materials, *Advanced Materials*, 28 (2016) 3321-3325.
- [48] M.-H. Phan, S.-C. Yu, Review of the magnetocaloric effect in manganite materials, *Journal of Magnetism*

- and Magnetic Materials, 308 (2007) 325-340.
- [49] E. Stern-Taulats, A. Planes, P. Lloveras, M. Barrio, J.-L. Tamarit, S. Pramanick, S. Majumdar, C. Frontera, L. Mañosa, Barocaloric and magnetocaloric effects in Fe₄₉Rh₅₁, *Physical Review B*, 89 (2014) 214105.
- [50] Y. Liu, L.C. Phillips, R. Mattana, M. Bibes, A. Barthélémy, B. Dkhil, Large reversible caloric effect in FeRh thin films via a dual-stimulus multicaloric cycle, *Nature Communications*, 7 (2016) 11614.
- [51] G. Castellano, Thermodynamic potentials for simple magnetic systems, *Journal of Magnetism and Magnetic Materials*, 260 (2003) 146-150.
- [52] Z. Zheng, Z. Zhu, H. Yu, D. Zeng, Y. Li, A. He, Y. Mozharivskiy, Large magnetic entropy change and magnetic phase transitions in rapidly quenched bulk Mn-Fe-P-Si alloys, *Journal of Alloys and Compounds*, 725 (2017) 1069-1076.
- [53] J. Lyubina, Magnetocaloric materials for energy efficient cooling, *Journal of Physics D: Applied Physics*, 50 (2017) 053002.
- [54] M. Wood, W. Potter, General analysis of magnetic refrigeration and its optimization using a new concept: maximization of refrigerant capacity, *Cryogenics*, 25 (1985) 667-683.
- [55] E. Brück, H. Yibole, L. Zhang, A universal metric for ferroic energy materials, *Philosophical Transactions of the Royal Society A: Mathematical, Physical and Engineering Sciences*, 374 (2016) 20150303.
- [56] F. Guillou, H. Yibole, G. Porcari, L. Zhang, N. Van Dijk, E. Brück, Magnetocaloric effect, cyclability and coefficient of refrigerant performance in the MnFe (P, Si, B) system, *Journal of Applied Physics*, 116 (2014).
- [57] K.A. Gschneidner, V.K. Pecharsky, A.O. Tsokol, Recent developments in magnetocaloric materials, *Reports on Progress in Physics*, 68 (2005) 1479-1539.
- [58] J. Li, T. Numazawa, K. Matsumoto, Y. Yanagisawa, H. Nakagome, A Modeling Study on the Geometry of Active Magnetic Regenerator, *Advances in Cryogenic Engineering*, Vols 57a and 57b, 1434 (2012) 327-334.
- [59] T. Lei, K. Engelbrecht, K.K. Nielsen, C.T. Veje, Study of geometries of active magnetic regenerators for room temperature magnetocaloric refrigeration, *Applied Thermal Engineering*, 111 (2017) 1232-1243.
- [60] J. Tušek, A. Kitanovski, A. Poredoš, Geometrical optimization of packed-bed and parallel-plate active magnetic regenerators, *International Journal of Refrigeration*, 36 (2013) 1456-1464.
- [61] P.V. Trevizoli, A.T. Nakashima, G.F. Peixer, J.R. Barbosa, Performance assessment of different porous matrix geometries for active magnetic regenerators, *Applied Energy*, 187 (2017) 847-861.
- [62] S. Ergun, A.A. Orning, Fluid Flow through Randomly Packed Columns and Fluidized Beds, *Industrial & Engineering Chemistry*, 41 (1949) 1179-1184.
- [63] C.R.H. Bahl, K. Navickaitė, H. Neves Bez, T. Lei, K. Engelbrecht, R. Bjørk, K. Li, Z. Li, J. Shen, W. Dai, J. Jia, Y. Wu, Y. Long, F. Hu, B. Shen, Operational test of bonded magnetocaloric plates, *International Journal of Refrigeration*, 76 (2017) 245-251.
- [64] B. Pulko, J. Tusek, J.D. Moore, B. Weise, K. Skokov, O. Mityashkin, A. Kitanovski, C. Favero, P. Fajfar, O. Gutfleisch, A. Waske, A. Foredos, Epoxy-bonded La-Fe-Co-Si magnetocaloric plates, *Journal of Magnetism and Magnetic Materials*, 375 (2015) 65-73.
- [65] J. Liang, C.D. Christiansen, K. Engelbrecht, K.K. Nielsen, R. Bjørk, C.R.H. Bahl, Characterization of Freeze-Cast Micro-Channel Monoliths as Active and Passive Regenerators, *Frontiers in Energy Research*, 8 (2020).
- [66] K. Navickaitė, J. Liang, C. Bahl, S. Wieland, T. Buchenau, K. Engelbrecht, Experimental characterization of active magnetic regenerators constructed using laser beam melting technique, *Applied Thermal Engineering*, 174 (2020) 115297.
- [67] J. Liang, K. Engelbrecht, K.K. Nielsen, K. Loewe, H. Vieyra, A. Barcza, C.R.H. Bahl, Performance assessment of a triangular microchannel active magnetic regenerator, *Applied Thermal Engineering*, 186 (2021) 116519.
- [68] A. Funk, J. Freudenberger, A. Waske, M. Krautz, Getting magnetocaloric materials into good shape: Cold-working of La (Fe, Co, Si) 13 by powder-in-tube-processing, *Materials today energy*, 9 (2018) 223-228.
- [69] K. Kamiya, K. Matsumoto, T. Numazawa, S. Masuyama, H. Takeya, A.T. Saito, N. Kumazawa, K. Futatsuka, K. Matsunaga, T. Shirai, S. Takada, T. Iida, Active magnetic regenerative refrigeration using superconducting solenoid for hydrogen liquefaction, *Applied Physics Express*, 15 (2022) 053001.
- [70] A. Rowe, A. Tura, Experimental investigation of a three-material layered active magnetic regenerator, *International Journal of Refrigeration*, 29 (2006) 1286-1293.
- [71] U. Tomc, S. Nosan, K. Klínar, A. Kitanovski, Towards powerful magnetocaloric devices with static electro-permanent magnets, *Journal of Advanced Research*, 45 (2023) 157-181.
- [72] R. Bjørk, C.R.H. Bahl, N. Pryds, A. Smith, Designing a magnet for magnetic refrigeration, Technical University of Denmark/Danmarks Tekniske Universitet, Department of Physics/Institut for Fysik, 2010.
- [73] R. Teyber, P.V. Trevizoli, T.V. Christiaanse, P. Govindappa, I. Niknia, A. Rowe, Permanent magnet design for magnetic heat pumps using total cost minimization, *Journal of Magnetism and Magnetic Materials*, 442 (2017) 87-96.
- [74] J. Forchelet, L. Zamni, S.E. El Alami, J. Hu, M. Balli, O. Sari, Corrosion behavior of gadolinium and La-Fe-Co-Si compounds in various heat conducting fluids, *International Journal of Refrigeration-Revue Internationale Du Froid*, 37 (2014) 307-313.
- [75] M.S. Kamran, H.O. Ahmad, H.S. Wang, Review on the developments of active magnetic regenerator refrigerators – Evaluated by performance, *Renewable and Sustainable Energy Reviews*, 133 (2020) 110247.
- [76] A. Greco, C. Aprea, A. Maiorino, C. Masselli, A review of the state of the art of solid-state caloric cooling processes at room-temperature before 2019, *International Journal of Refrigeration*, 106 (2019) 66-88.
- [77] K. Rajamani, E. Juffermans, L. Granelli, A. De Cuadra Rabaneda, W. Rohlf, M. ter Brake, T. van der Meer, M. Shahi, A low-frequency ferrohydrodynamic pump for a magneto-caloric refrigerator, *Applied Energy*, 355 (2024) 122253.
- [78] W.A. Steyert, Stirling-Cycle Rotating Magnetic Refrigerators and Heat Engines for Use near Room-Temperature, *Journal of Applied Physics*, 49 (1978) 1216-1226.
- [79] J.A. Barclay, Active and passive magnetic regenerators in gas/magnetic refrigerators, *Journal of Alloys and Compounds*, 207-208 (1994) 355-361.
- [80] C. Zimm, A. Boeder, J. Chell, A. Sternberg, A. Fujita, S. Fujieda, K. Fukamichi, Design and performance of a permanent-magnet rotary refrigerator, *International Journal of Refrigeration-Revue Internationale Du Froid*, 29 (2006) 1302-1306.
- [81] B.F. Yu, M. Liu, P.W. Egolf, A. Kitanovski, A review of magnetic refrigerator and heat pump prototypes built before the year 2010, *International Journal of Refrigeration-Revue Internationale Du Froid*, 33 (2010) 1029-1060.
- [82] C. Zimm, A. Boeder, B. Mueller, K. Rule, S.L. Russek, The evolution of magnetocaloric heat-pump devices, *Mrs Bulletin*, 43 (2018) 274-279.
- [83] F. Scarpa, G. Tagliafico, L.A. Tagliafico, A classification methodology applied to existing room temperature magnetic refrigerators up to the year 2014, *Renewable and Sustainable Energy Reviews*, 50 (2015) 497-503.
- [84] A. Tura, A. Rowe, Permanent magnet magnetic refrigerator design and experimental characterization, *International Journal of Refrigeration-Revue Internationale Du Froid*, 34 (2011) 628-639.
- [85] D.S. Arnold, A. Tura, A. Ruebsaat-Trott, A. Rowe, Design improvements of a permanent magnet active magnetic refrigerator, *International Journal of Refrigeration-Revue Internationale Du Froid*, 37 (2014) 99-105.
- [86] K. Engelbrecht, C.R.H. Bahl, K.K. Nielsen, Experimental results for a magnetic refrigerator using three different types of magnetocaloric material regenerators, *International Journal of Refrigeration-Revue Internationale Du Froid*, 34 (2011) 1132-1140.
- [87] K. Engelbrecht, D. Eriksen, C.R.H. Bahl, R. Bjørk, J. Geyti, J.A. Lozano, K.K. Nielsen, F. Saxild, A. Smith, N. Pryds, Experimental results for a novel rotary active magnetic regenerator, *International Journal of Refrigeration-Revue Internationale Du Froid*, 35 (2012) 1498-1505.
- [88] J.A. Lozano, K. Engelbrecht, C.R.H. Bahl, K.K. Nielsen, J.R. Barbosa Jr, A.T. Prata, N. Pryds, Experimental and numerical results of a high frequency rotating active magnetic refrigerator, *International Journal of Refrigeration*, 37 (2014) 92-98.
- [89] D. Eriksen, K. Engelbrecht, C.R.H. Bahl, R. Bjørk, K.K. Nielsen, A.R. Insinga, N. Pryds, Design and experimental tests of a rotary active magnetic regenerator prototype, *International Journal of Refrigeration-Revue Internationale Du Froid*, 58 (2015) 14-21.
- [90] H. Johra, K. Filonenko, P. Heiselberg, C. Veje, T. Lei, S. Dall'Olio, K. Engelbrecht, C. Bahl, Integration of a magnetocaloric heat pump in a low-energy residential building, *Building Simulation*, (2018).
- [91] J.A. Lozano, M.S. Capovilla, P.V. Trevizoli, K. Engelbrecht, C.R.H. Bahl, J.R. Barbosa, Development of a novel rotary magnetic refrigerator, *International Journal of Refrigeration-Revue Internationale Du Froid*, 68 (2016) 187-197.
- [92] C. Aprea, A. Greco, A. Maiorino, R. Mastrullo, A. Tura, Initial experimental results from a rotary permanent magnet magnetic refrigerator, *International Journal of Refrigeration*, (2014).
- [93] J.R. Gómez, R.F. García, J.C. Carril, M.R. Gómez, Experimental analysis of a reciprocating magnetic refrigeration prototype, *International Journal of Refrigeration*, 36 (2013) 1388-1398.
- [94] D. Velázquez, C. Estepa, E. Palacios, R. Burriel, A comprehensive study of a versatile magnetic refrigeration demonstrator, *International Journal of Refrigeration*, 63 (2016) 14-24.
- [95] A. Czernuszewicz, J. Kaleta, M. Królewicz, D. Lewandowski, R. Mech, P. Wiewióski, A test stand to study

- the possibility of using magnetocaloric materials for refrigerators, *International Journal of Refrigeration*, 37 (2014) 72-77.
- [96] S. Jacobs, J. Auringer, A. Boeder, J. Chell, L. Komorowski, J. Leonard, S. Russek, C. Zimm, The performance of a large-scale rotary magnetic refrigerator, *International Journal of Refrigeration-Revue Internationale Du Froid*, 37 (2014) 84-91.
- [97] B. Monfared, B. Palm, New magnetic refrigeration prototype with application in household and professional refrigerators, in: 7th International Conference on Magnetic Refrigeration at Room Temperature, 2016.
- [98] Z. Cheng, H. Jiaohong, Y. Hongwei, J. Peiyu, C. Juan, L. Cuilan, L. Zhaojie, Z. Yingde, Design and research of the room temperature magnetic wine cabinet, in: *Proceedings of the Seventh International Conference on Magnetic Refrigeration at Room Temperature*, Torino, Italy, 2016, pp. 63-66.
- [99] A. Kitanovski, U. Plaznik, U. Tomc, A. Poredoš, Present and future caloric refrigeration and heat-pump technologies, *International Journal of Refrigeration*, 57 (2015) 288-298.
- [100] S. Lionte, M. Risser, C. Muller, A 15 kW magnetocaloric proof-of-concept unit: initial development and first experimental results, *International Journal of Refrigeration*, (2020).
- [101] J.-B. Chaudron, C. Muller, M. Hittinger, M. Risser, S. Lionte, Performance measurements on a large-scale magnetocaloric cooling application at room temperature, in: *Proceedings of the Thermag VIII International Conference on Caloric Cooling*, 2018.
- [102] A. Waske, D. Dzekan, K. Sellschopp, D. Berger, A. Stork, K. Nielsch, S. Fähler, Energy harvesting near room temperature using a thermomagnetic generator with a pretzel-like magnetic flux topology, *Nature Energy*, 4 (2019) 68-74.
- [103] M. Gueltig, F. Wendler, H. Ossmer, M. Ohtsuka, H. Miki, T. Takagi, M. Kohl, High-Performance Thermomagnetic Generators Based on Heusler Alloy Films, *Advanced Energy Materials*, 7 (2017) 1601879.
- [104] X. Liu, H. Chen, J. Huang, K. Qiao, Z. Yu, L. Xie, R.V. Ramanujan, F. Hu, K. Chu, Y. Long, H. Zhang, High-performance thermomagnetic generator controlled by a magnetocaloric switch, *Nature Communications*, 14 (2023).
- [105] K. Murakami, M. Nemoto, Some experiments and considerations on the behavior of thermomagnetic motors, *IEEE Transactions on Magnetics*, 8 (1972) 387-389.
- [106] C.-C. Cheng, T.-K. Chung, C.-C. Chen, H.-M. Wang, A Rotational Actuator Using a Thermomagnetic-Induced Magnetic Force Interaction, *IEEE Transactions on Magnetics*, 54 (2018) 1-8.
- [107] M. Ujihara, G.P. Carman, D.G. Lee, Thermal energy harvesting device using ferromagnetic materials, *Applied Physics Letters*, 91 (2007) 093508.
- [108] E. Garofalo, M. Bevione, L. Cecchini, F. Mattiussi, A. Chiolerio, Waste Heat to Power: Technologies, Current Applications, and Future Potential, *Energy Technology*, (2020) 2000413.
- [109] G.H. Kaneko, A.C. Souza, F. Moro, F.C. Colman, W.A.S. Conceição, C.S. Alves, P.V. Trevizoli, Design and assembling of a magnetic circuit for a thermomagnetic motor apparatus, *Journal of the Brazilian Society of Mechanical Sciences and Engineering*, 41 (2019) 394.
- [110] m. almanza, morgan.almanza@gmail.com, A. Pasko, A. Bartok, F. Mazaleyrat, M. Lobue, Thermal energy harvesting: thermomagnetic versus thermoelectric generator, in: 7th International Conference on Magnetic Refrigeration at Room Temperature (Thermag VII), Turin, Italy, 2016.
- [111] C.S. Alves, F.C. Colman, G.L. Foleiss, G.T.F. Vieira, W. Szpak, Numerical simulation and design of a thermomagnetic motor, *Applied Thermal Engineering*, 61 (2013) 616-622.
- [112] P. Coray, D. Wymann, R. Brunner, N. Vida, Fully Operational Prototype of a 1kW Thermo-Magnetic Motor for Generating Electricity from < 80°C Heat, Abstract for the Delft Days on Magneto Calorics, DDMC, (2015).
- [113] J. Hey, M. Repaka, T. Li, J.L. Tan, Design Optimization of a Rotary Thermomagnetic Motor for More Efficient Heat Energy Harvesting, *Energies*, 15 (2022) 6334.

CHAPTER 2

Experimental Techniques

2.1 SQUID

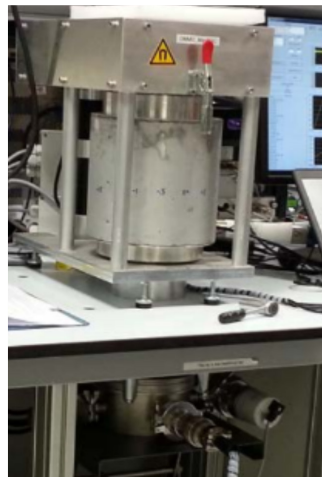
A Superconducting Quantum Interference Device (SQUID) is a highly sensitive device that can detect extremely small changes in magnetic flux.

The Squid operates through a superconducting loop that has two Josephson Junctions. It is made up of two superconducting electrodes that are separated by an insulating layer. As a magnetic sample moves through a series of magnetic coils, a current is produced in the Pickup coil. This current is then transferred to a magnetic field by a secondary coil, which penetrates the superconducting loop. The magnetic field is known as the modulation of the critical supercurrent through the junctions. To keep this current constant, a Feedback loop is used, which provides a signal proportional to the magnetization of the sample.

The SQUID used for magnetic measurement in dissertation is a Quantum Design MPMS-XL[1]. It can measure the Magnetic properties of various samples under temperature range from 4 to 370 K and a field range from 0 - 8 Tesla.

2.2 MDSC

Heat-flux based Differential Scanning Calorimetry (DSC) is a thermal analytical device that measures the difference in the amount of heat required to increase the temperature of a sample and a reference. In a DSC the temperature of the sample unit, formed by a sample and reference material, is varied in a specified program, and the temperature difference between the sample and the reference material is measured as a function of temperature. The DSC comprises the sample and reference holder, the heat resistor, the heat sink, and the heater. The heat of the heater is supplied into the sample and the reference through the heat sink and heat resistor.



The special DSC used in this work is an in-Magnetic-field DSC (MDSC) developed in house by BASF New Business. The features of this MDSC are:

- 0-1.5 T Halbach nested permanent magnet field source. The field strength is adjustable mechanically with program control.
- Thermoelectric heat flow sensors provide high sensitivity.

- Temperature is regulated between 230 and 350 K using Peltier heating and cooling with scanning rate up to 6 K/min.
- Turbo vacuum ($<10^{-5}$ mbar) is used to reduce heat loss and to avoid moisture condensation.

2.3 NI COMPACTRIO

CompactRIO[2] is a real-time embedded industrial controller made by National Instruments for industrial control systems. It consists of a controller, a chassis, and a set of I/O modules that can be customized for different applications. The controller runs the NI Linux Real-Time OS and executes LabVIEW Real-Time applications. The chassis contains a user-programmable FPGA that can interface with the I/O modules and perform high-speed logic and timing tasks. The I/O modules are sensor- or protocol-specific and provide signal conditioning and conversion. It supports various industrial I/O modules from both NI and third-party vendors.

The I/O modules used with CompactRIO in this work are:

- NI 9213: A thermocouple input module that can measure up to 16 channels of temperature with 24-bit resolution and 75 S/s sampling rate. It supports various thermocouple types and provides cold-junction compensation, open-thermocouple detection, and built-in noise filtering
- NI 9381: A multifunction I/O module that can perform analog input, analog output, digital input, and digital output operations. It has 8 channels of 16-bit analog input, 8 channels of 16-bit analog output, 32 channels of 5 V/TTL digital input/output, and two 32-bit counters. It can also generate PWM signals and measure frequency, period, pulse width, and quadrature encoder signals.

2.4 DELTA SM300-10 DC POWER SOURCE

The Delta SM300-10 D power source[3] is a programmable DC power supply that can deliver up to 300 V and 10 A. It is part of the SM6000 series of power supplies from Delta Elektronika, which are designed for long life, high accuracy, low noise and excellent dynamic response. The SM300-10 D power source has the following features:

It has a wide input voltage range of 85 to 264 VAC, and can deliver up to 300 W of output power with a single output voltage of 10 VDC. The power source features a high efficiency of up to 94%, and a low ripple and noise of less than 50 mVp-p. The power source also has various protection functions, such as overvoltage, overcurrent,

overtemperature, and short circuit protection, to ensure the safety and reliability of the connected devices. The communication protocols can be: Ethernet, RS232 or other isolated remote programming features can be factory installed.

2.5 SCHNEIDER SERVO DRIVE LXM32M

The Schneider Lexium 32M servo motor is a compact and powerful servo motor that can be used with the Lexium 32 servo drive[4]. The Lexium 32M servo motor has a high torque density and a low inertia, making it suitable for dynamic applications that require precise positioning and speed control. The Lexium 32M servo motor can operate in two control modes: speed profile and position profile. In speed profile mode, the servo drive controls the speed of the motor according to a predefined speed profile, which can be linear, trapezoidal, or S-shaped. In position profile mode, the servo drive controls the position of the motor according to a predefined position profile, which can be absolute or relative. The position profile can also include acceleration, deceleration, and dwell times. The Lexium 32M servo motor can communicate with the Lexium 32 servo drive via a digital encoder, which provides feedback on the motor speed and position. The Lexium 32M servo motor also has an optional integrated holding brake, which can prevent the motor from rotating when the power is off or in case of an emergency stop.

REFERENCES

- [1] Quantum Design MPMS, <https://qdusa.com/products/mpms3.html>.
- [2] NI CompactRIO, <https://www.ni.com/en/shop/compactrio.html>.
- [3] Delta SM300-10 DC power source, <https://www.delta-elektronika.nl/products>.
- [4] Schneider servo drive LXM32M, <https://www.se.com/nl/nl/download/document/0198441113767-EN/>.

CHAPTER 3

Prototype Heat Pump – MMFF cooler

3.1 BACKGROUND OF DESIGN

The first-hand experience of prototyping magnetic refrigerator began in 2009: Zheng et al. of the research group of Magnetic Materials and Functional Thin Films (MMFF) of South China University of Technology developed a magnetic refrigerator setup[1]. This system has a reciprocating operation design, 1.5 T magnetic field, and Gd sphere sized in the range of 0.5-1.5 mm. As the first attempt of such research, a temperature span of 1.6 K has been reached after 50 minutes of operation.

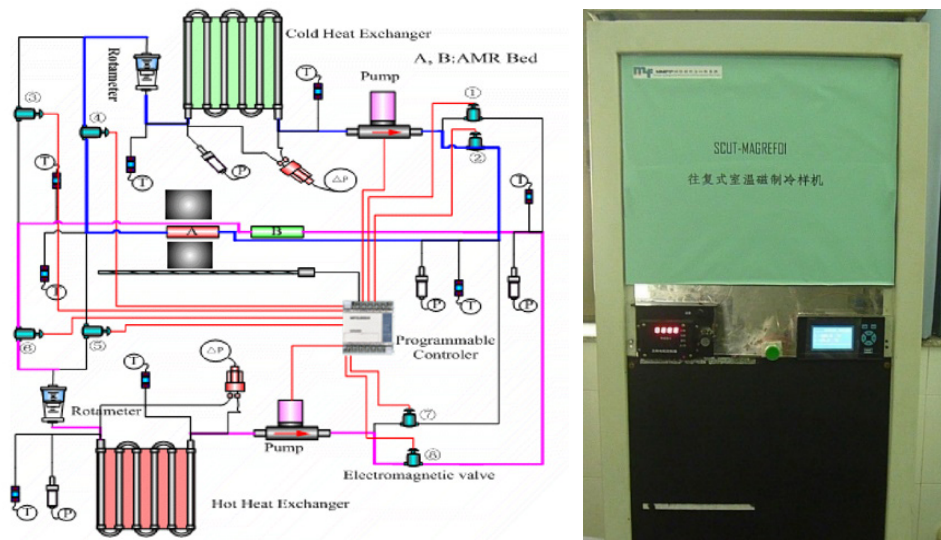


Figure 3.1: The magnetic refrigerator setup developed by Zheng et. al 2009

In the same period, the development of magnetic refrigerator prototype had set off a boom all around the world[2]. Most of newly developed (between 2006-2011) prototypes to be rotary type, for maximizing the utilization of the permanent magnet, and improve the cooling power and COP, in order to make them more commercial-ready[3-6]. Despite the advantages, magnetic refrigerator of rotary type has also disadvantages such as, bulky structure, complicated hydraulic system and high demand of control system[7-9]. On the other hand, although limited on performance, the magnetic refrigerator of reciprocating type has usually confined design, simple hydraulic system, and highly flexible operation[10, 11].

To avoid complication and to gain more experience on system development, the second prototyping attempt of MMFF was decided to be a reciprocation type, which can make use of the gained experience from its predecessor and avoid the possible complication

on the magnetic field source and hydraulic system. However, as a step forward, the new prototype should adopt the advantage of the rotary type to the reciprocating type. "If possible, make a hybrid!" this was the decision quoted from one progress meeting. The main system of MMFF cooler was built in June of 2013 and followed by a few times of partial upgrade since then. As a second attempt of MMFF, this prototype continues the reciprocating design, while improving the performance by increasing the working frequency, simplifying the hydraulic system, and optimizing the control and measurement system. This prototype was also built for exploring the different packing method of the MCM and the control strategy of a magnetic refrigerator.

3.2 SYSTEM FEATURES

Usually, to simplify the system and limit the cost, typical proof-of-principle magnetic heat pump setups usually have only one regenerator. Due to the nature of the AMR cycle, one regenerator can only work in the magnetization stage or demagnetization stage. Therefore, if there is only one regenerator, neither the heating cycle nor the cooling cycle is continuous. To address this problem, the MMFF cooler was developed with the idea of a continuous regeneration cycle. The combination of two pairs of mirror symmetrically placed regenerator and permanent magnet assemblies enabled high working frequency while the magnetic force was well balanced. Four linear rails can ensure the regenerators only reciprocating in x-y plane while has no freedom in z-direction, to avoid unexpected contact with magnet assemblies. A servo motor Panasonic MINAS A5 has been applied to generate the reciprocating movement, this will also enable the self-adaptive control of speed toward the position varying magnetic force. The operation principal schematic of the MMFF cooler was shown in Fig. 3.2.

A 2D magnetic field simulation has been performed with Ansys, as shown in Fig. 3.3 (a) the magnetic flux in high field region of the airgap of the magnet assembly is focused and homogenous. Fig. 3.3 (b) shows the internal configuration of the magnet assembly. As can see, the red arrows indicate the magnetization direction of the N50M NdFeB permanent magnet parts, while all the rest of the parts are DT4E pure iron. Note that the layout of the permanent magnets has followed the rule of Halbach array. Fig.3.3 (c) shows the field density measured with a Gaussmeter and 2D Hall probe. The colored arrow symbols in Fig.3.3 (b) indicate the direction of the field density measurement.

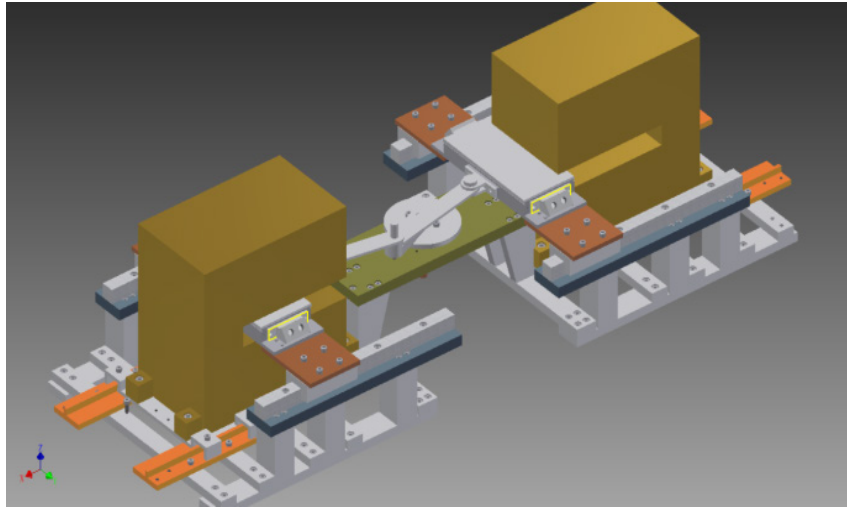
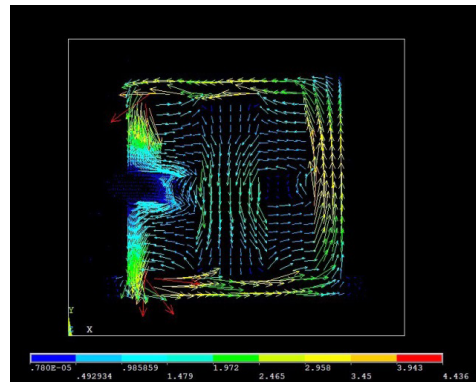
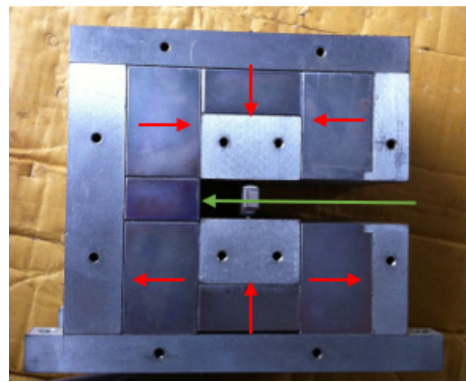


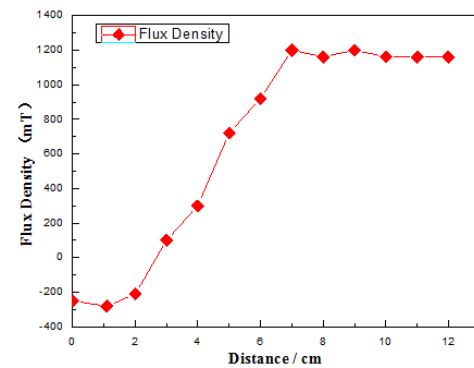
Figure 3.2: Operation principle of MMFF Cooler



(a)



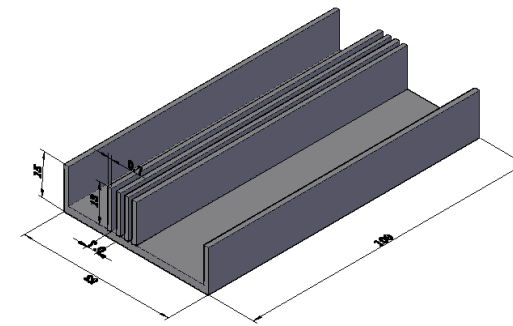
(b)



(c)

Figure 3.3: The permanent magnet assembly of MMFF Cooler

This prototype used gadolinium plates with a 99.9% purity as working material. With a dimension 100x13x0.7 mm each, the parallel plate regenerator has in total 53 pieces of gadolinium plate with a spacing of 0.3 mm. Thus, the overall porosity of each regenerator is 23.07%. The gadolinium plates have been processed with a wire saw, with a subsequential polishing process to make a smooth finishing. Two pieces of SUS304 stainless steel plates of 1mm are used as guiding plates, which are carved with notches for the gadolinium plates and then glued to the top and bottom of the chamber of regenerators. The gadolinium plates can then be slid into the regenerator easily and will be supported by the guiding plates to avoid the deformation caused by magnetic force.



(a)



(b)

Figure 3.4: Magnetocaloric material in the regenerator

The two regenerators have an internal dimension of 130x13x53 mm, thus, a volume of 89.57 ml each. There are two connecting holes on the side lid, one for tubing and the other for Pt100 temperature sensor.

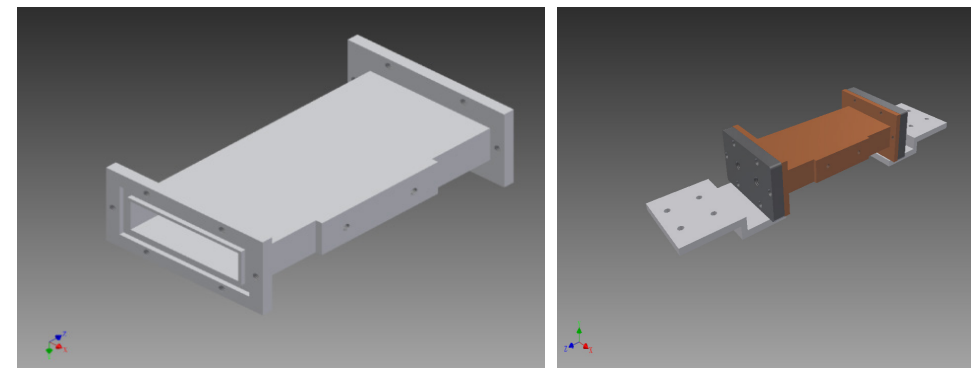


Figure 3.5: Regenerator

The hot heat exchanger of MMFF Cooler is inspired by spray cooling, which requires the evaporation of water to remove heat. The spray cooling chamber of the MMFF Cooler enhances the cooling efficiency by adding forced convection of air in the chamber with two DC electric fans. A DC diaphragm pump was used to cycle the water in the chamber between the water tank and the nozzles. In the trials, the spray cooling chamber can keep the hot heat exchanger only 1~2 degrees above ambient temperature.

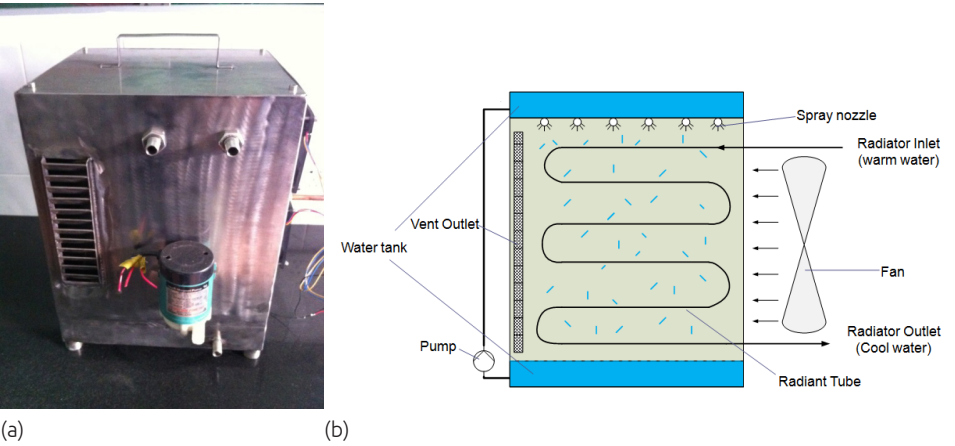


Figure 3.6: the Hot end heat exchanger

The cold end of MMFF cooler was basically an insulation industrial foam box with warded copper tube inside, as shown in Fig. 3.7(a). The Pt100 was attached to the surface of the copper tube. The insulation elastomer foam in Fig. 3.7(b) was added after the first experiment run of the system, which significantly improved the temperature span of the system in the experiments later. Note that the inner diameter of the copper tube was 6mm, while the inner diameter of the connection tube between all other parts of the system was 9mm. Therefore, the velocity of the HTF in the cold end was much faster than in other parts of the system.

The overall operation control of this prototype is handled by a programmable logic controller (PLC) unit FX1N-40MR from Mitsubishi. With 24 bits digital input and 16 relay output available, the PLC unit receives signal from both the sensors and manual control interface while sends control signals to the servo motor and the solenoid valves. The response time for both input and output signals are 10 ms, which ensures the synchronization for all the operations. The logical control flow chart is as Fig. 3.8: the initiation process includes configuration of motor speed, pump speed, and start the data logging; then the system enters automatic process, the valve switching is synchronized with the regenerator movement; the system will only stop when “stop” command is triggered.

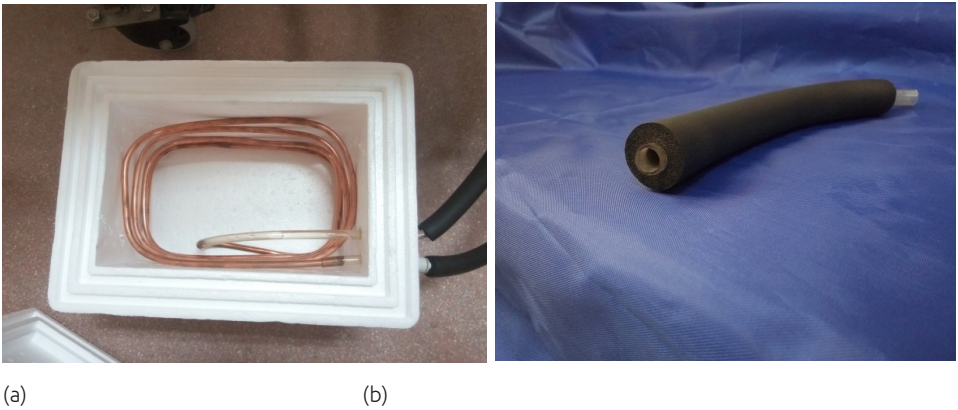


Figure 3.7: the Cold end of the system

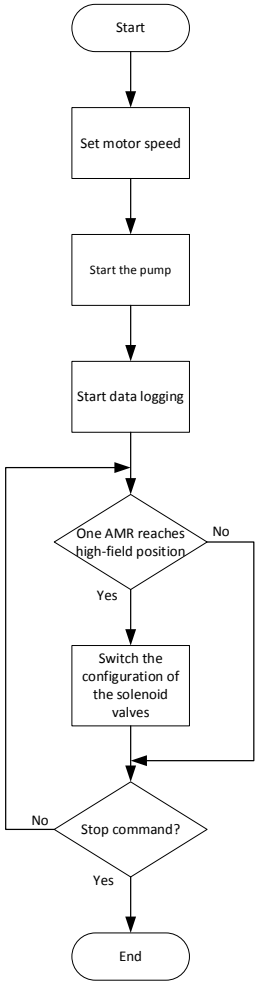


Figure 3.8: control flow chart of MMFF prototype

The hydraulic system of MMFF Cooler is shown in Fig. 2.7, which consists: two permanent magnet assembly: 1 and 4; three PT100 temperature sensors: 2, 6, and 17; cold heat exchanger: 3; two proximity switches: 5 and 16; hot heat exchangers (in the same compartment): 7 and 13; four solenoid valves: 8, 9, 11, and 12; DC gear pump: 10; Programmable Logic Controller (PLC): 14; servo motor: 15; active magnetic regenerators: A and B. All tubing in the hydraulic system is PVC tube with an inner diameter of 9mm.

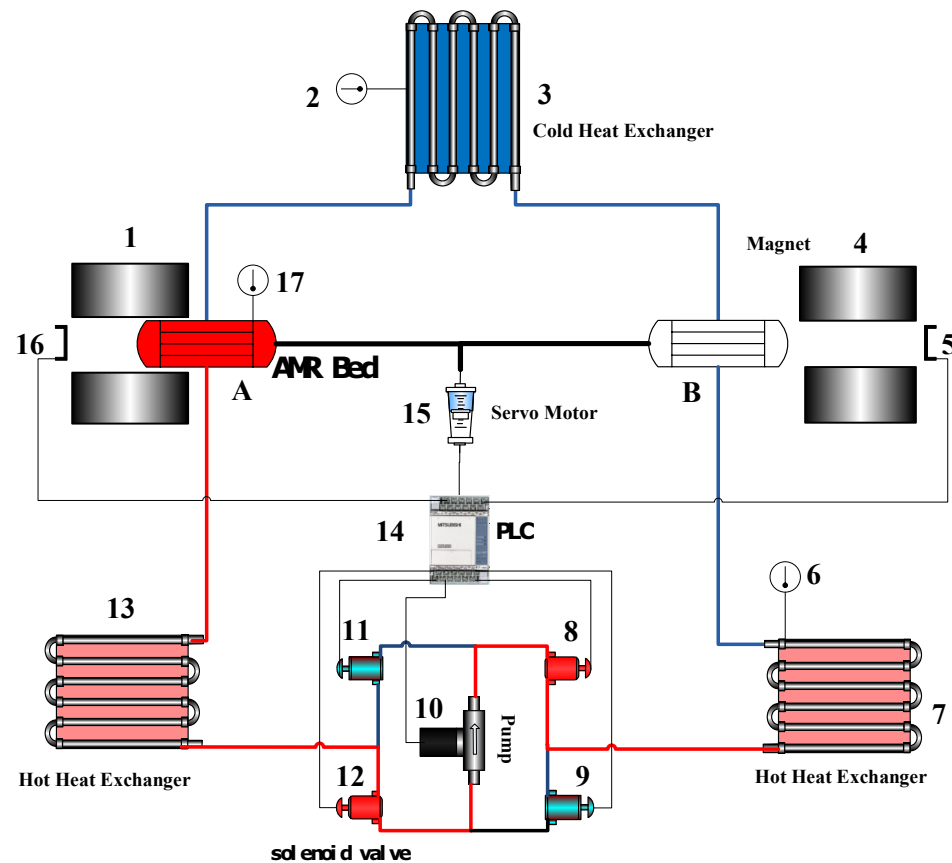


Figure 3.9: Schematic of Hydraulic system

The position of the AMRs was determined by two proximity switches (5 and 16). Whenever one AMR enters the high-field region of the magnet, the proximity switch on that side will be triggered and the configuration of the solenoid valves will be changed via PLC. When valve pair 8 and 12 are opened while valve pair 9 and 11 are closed, the cooled HTF flow from demagnetized AMR A will flow into the cold heat exchanger 3,

while the heated HTF from magnetized AMR B will flow into the hot heat exchanger 7; When valve pair 9 and 11 are opened while valve pair 8 and 12 are closed, the cooled HTF from demagnetized AMR B will flow into the cold heat exchanger while the heated HTF from magnetized AMR A will flow into hot heat exchanger 13. Thanks to the proximity switches, the timing for valve switching in this system is directly triggered by the position of the AMR.

An overview of the completed MMFF Cooler can be found in Fig. 2.8



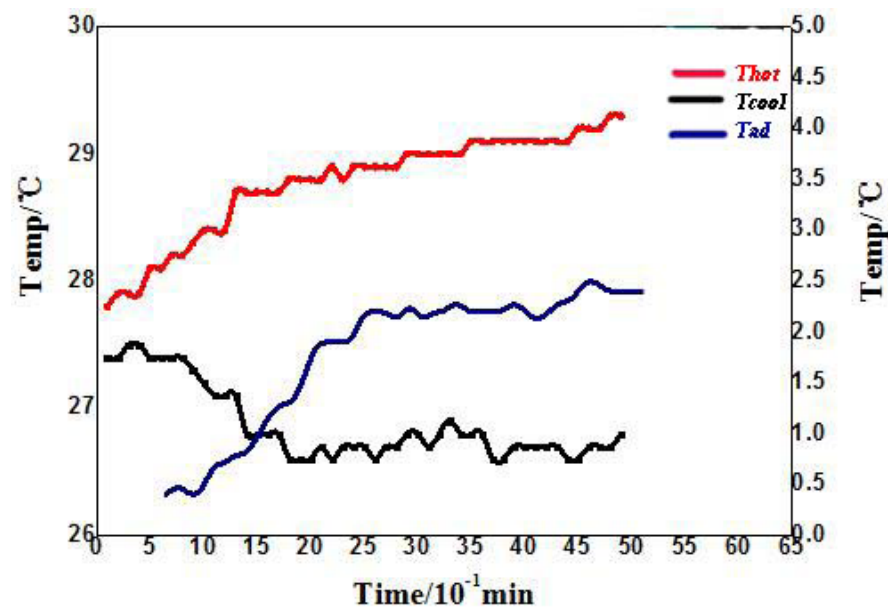
Figure 3.10: overview of the MMFF Cooler

3.3 EXPERIMENT AND RESULTS

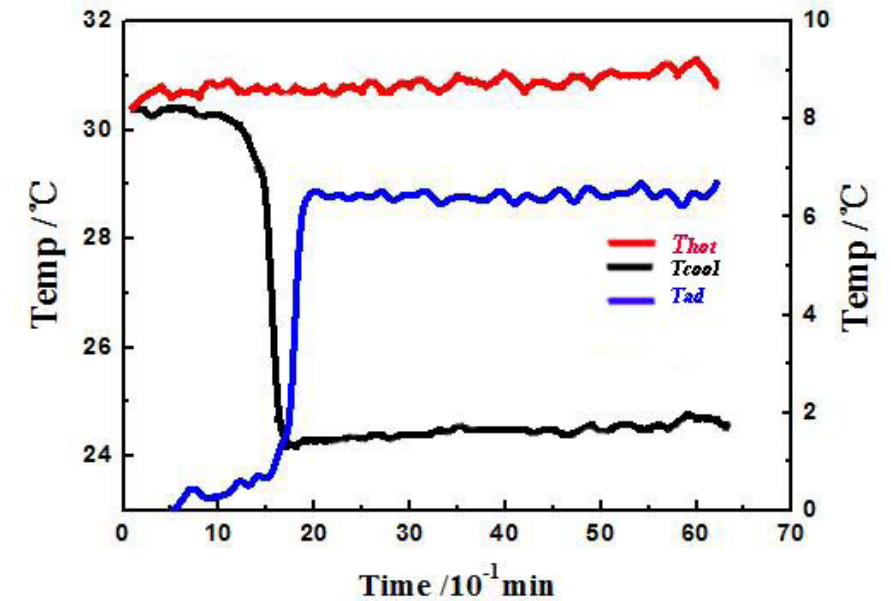
Not many experiments on MMFF Cooler were successful due to the not optimized design. The common failures were leakage at customized connectors, flow channels blocked by deformed Gd plates, or broken draft coupling. After solving these critical problems, a few performance measurements have been performed. The experimental conditions are as followed:

The results were measured under the condition of 1 Hz system frequency, which equalled to 2 Hz AMR frequency as the two regenerators were in their independent AMR cycle. The volumetric flow rate was fixed at 1400 ml/min flow rate, controlled by a PWM motor driver. During the experiment room temperature was maintained at 27.5 °C by air conditioner. The HTF used in the experiments was a solution of demi-water with 2% (weight percent) of NaOH, which served as a corrosion inhibitor.

In the first trial run, the temperature span develop is quite small. As one can see in Fig. 3.11 (a) the major part of the temperature span was developed in the first 15 to 20 minutes, and since then only the temperature of hot side was slightly increased. The temperature of the cold end was cooled from 27.4°C to 26.6°C, while the temperature of the hot end was heated from 27.8°C to 29.1°C, the maximum temperature span is 2.5°C. One can notice that the cooling power of the system was very small and the temperature span at the cold end seemed to be suppressed more the temperature span at the hot end. One most possible reason for this was the large dead volume at the cold heat exchanger. The two regenerators share the sample CHEX, however, since there was only one piece of tube for both the inflow and outflow, almost all the volume contained in the tube became dead volume. Besides, due to the long distance between the CHEX and the two regenerators, it took a long time before the temperature in the CHEX started to respond the cooling power generated by the regenerators.



(a)



(b)

Figure 3.11: Performance data of the two trials

The temperature span in the second trial was significantly improved, while maintaining the hot end temperature at around 31°C, a maximum temperature span of 6.2 K has been reached at steady state, as shown in Fig 3.11 (b). However, there was an unusual step in the temperature profile of the cold end. From 0 minute to 15 minute, the temperature span developing was as little as 0 to 0.5 K. Then in just 4 minutes, a temperature span of 6.1 K was developed, but only 0.1 K more span was developed in the rest of the experiment. The long delay was probably caused by the long tube between the AMRs and the cold end of the system, which was a big dead volume between the cold side of the AMRs and the system cold end. In the second experiment, this part of tubing was better insulated with industrial foam sleeves compared to the first experiment. Therefore, the cooled HTF could accumulate in the dead volume. When the volumetric flow rate was not high enough, it would take quite some cycles before the cooled HTF from the cold side of the AMR to reach the cold end of the system. Besides, since the total volume of copper tube in the cold heat exchanger is very small compare to the dead volume, the cooling down process was respectively short.

3.4 CONCLUSION

A proof-of-principle magnetic refrigerator prototype – MMFF Cooler has been developed. The system was a reciprocating type, equipped with two permanent magnetic field sources of 1.2 T, the working material in the system is gadolinium plate. With 2 Hz AMR frequency, 1400 ml/min Volumatic flow rate, and hot end temperature 31°C, MMFF Cooler can reach a zero load maximum temperature span of 6.1 K. This result proved the AMR cycle has been successfully applied, though the system efficiency is far from optimal.

The result of the performance tests indicated that the design of the prototype can fulfil the requirement of a proof-of-principle prototype device. the performance of the system can be tuned by adjust the control parameters via the servo motor and the gear pump. Improved thermal insulation along the tubing results better temperature span. however, the system design is still quite immature as heat leak and dead volume significantly limited the cooling power, which is indicated by extended cooling time. Too many customized components are used, which suppresses the system performance and makes modification and expansion very difficult. Last but not least, the shaping and assembly mechanism of gadolinium plate needs improvement. The big thickness of Gd plate reduced the heat transfer efficiency and the lack of the supporting structure caused signification deformation when leaving field region.

REFERENCES

- [1] Z.G. Zheng, H.Y. Yu, X.C. Zhong, D.C. Zeng, Z.W. Liu, Design and performance study of the active magnetic refrigerator for room-temperature application, *International Journal of Refrigeration-Revue Internationale Du Froid*, 32 (2009) 78-86.
- [2] B. Yu, M. Liu, P.W. Egolf, A. Kitanovski, A review of magnetic refrigerator and heat pump prototypes built before the year 2010, *International Journal of Refrigeration*, 33 (2010) 1029-1060.
- [3] K. Engelbrecht, C.R.H. Bahl, K.K. Nielsen, Experimental results for a magnetic refrigerator using three different types of magnetocaloric material regenerators, *International Journal of Refrigeration-Revue Internationale Du Froid*, 34 (2011) 1132-1140.
- [4] J. Tušek, S. Zupan, A. Šarlah, I. Prebil, A. Poredoš, Development of a rotary magnetic refrigerator, *International Journal of Refrigeration*, 33 (2010) 294-300.
- [5] A. Kitanovski, P.W. Egolf, Application of magnetic refrigeration and its assessment, *Journal of Magnetism and Magnetic Materials*, 321 (2009) 777-781.
- [6] C. Zimm, A. Boeder, J. Chell, A. Sternberg, A. Fujita, S. Fujieda, K. Fukamichi, Design and performance of a permanent-magnet rotary refrigerator, *International Journal of Refrigeration-Revue Internationale Du Froid*, 29 (2006) 1302-1306.
- [7] F. Scarpa, G. Tagliafico, L.A. Tagliafico, Classification proposal for room temperature magnetic refrigerators, *International Journal of Refrigeration-Revue Internationale Du Froid*, 35 (2012) 453-458.
- [8] O. Gutfleisch, M.A. Willard, E. Bruck, C.H. Chen, S.G. Sankar, J.P. Liu, Magnetic Materials and Devices for the 21st Century: Stronger, Lighter, and More Energy Efficient, *Advanced Materials*, 23 (2011) 821-842.
- [9] A. Kitanovski, P.W. Egolf, Innovative ideas for future research on magnetocaloric technologies, *International Journal of Refrigeration-Revue Internationale Du Froid*, 33 (2010) 449-464.
- [10] P.V. Trevizoli, J.R. Barbosa, R.T.S. Ferreira, Experimental evaluation of a Gd-based linear reciprocating active magnetic regenerator test apparatus, *International Journal of Refrigeration-Revue Internationale Du Froid*, 34 (2011) 1518-1526.
- [11] A. Rowe, A. Tura, Experimental investigation of a three-material layered active magnetic regenerator, *International Journal of Refrigeration-Revue Internationale Du Froid*, 29 (2006) 1286-1293.

CHAPTER 4

**Experimental Rotary Magnetic
Refrigerator Prototype and its
performance optimization**

4.1 INTRODUCTION

Magnetic refrigeration (MR) at room temperature (RT) is considered as a competitive alternative of conventional vapor compression technology, which has led to various studies on RT MR devices since the first prototype at RT was developed by Brown [1]. Different thermal dynamic cycles such as the Stirling, Ericsson, Brayton cycles, have been invoked (for a review see e.g. [2]) to explore the magnetocaloric effect (MCE) until the active magnetic regeneration (AMR) cycle was proposed by [3], which is nowadays still the most promising cycle for magnetocaloric devices. Except for some early applications which are driven by exorbitant superconducting magnets [4, 5] as the magnetic field source, most MR devices today use permanent magnets, for its energy efficiency and spatial compactness. Different magnetic field sources, from the simple “C” shaped magnet to the complicated concentric Halbach cylinder, are developed for unique prototypes [6]. The configurations of the existing devices can generally be divided into two types depending on their magnetization and demagnetization operation: the reciprocating type and the rotary type [7]. The reciprocating type devices, which are usually with a simple structure and a low working frequency, are ideal for demonstrating the principle of the MR or testing the properties of the materials [8-10]. The rotary type devices are more compact, faster, performance oriented, and are thereby candidates for pre-commercial applications [11-18]. The hydraulic system is a circuit in which an energy storage and exchange medium called the heat transfer fluid (HTF) is implemented for transferring heat between different parts. Generally, the HTF should be a liquid-state material that is environmental friendly and has good heat transfer properties. Therefore, water and water/ethylene glycol are widely accepted. However, helium [19], silicon oil [20] and ferrofluid [21] are also used in a few applications. For the flow control system, as it is essential to change the flow path according to the magnetization/demagnetization condition during the working procedure, reliable automatic valves are widely employed. Mechanical valves like poppet valve are preferred by rotary systems for their mechanically synchronized switching and almost zero heat generation. However, the electrical valves like solenoid valves are widely used in the reciprocating designs [22], as they can be programmed for different purposes and are flexible to changes. Magnetocaloric material (MCM), employed as the refrigerant in MR devices, is the critical factor that decides the performance of the system. While most MR devices are still using gadolinium as a standard reference material, some have already explored new systems like layered magnetocaloric alloys such as Mn-Fe-P-Si(As) [23], La-Fe-Si [24], or Gd-X [25].

Significant progress has been made in the RT MR technology. Nevertheless, there are still fields that deserve more study. For instance, many reciprocating type experimental devices and many rotary type pre-commercial prototypes already exist, few of them can provide a pre-commercial environment for performance tests on different MCMs. In this paper, we present a new MR prototype for experimental proposes, named the FAME

Cooler. With a flexible and extendable configuration, it possesses large potential for MCM performance tests, and also capable of some MR studies toward commercialization.

4.2 DESIGN OVERVIEW

This prototype is designed specially for testing MCMs with different shapes and properties. Therefore, the setup leaves great freedom for alterations on the regenerator and working procedure while remaining a stable structure for pre-commercial scale experiments. To achieve this target, a specific scheme for moving magnetic field source, static regenerator/tubing and programmable solenoid valves are selected. The appearance of the system is shown in Fig. 4.1.

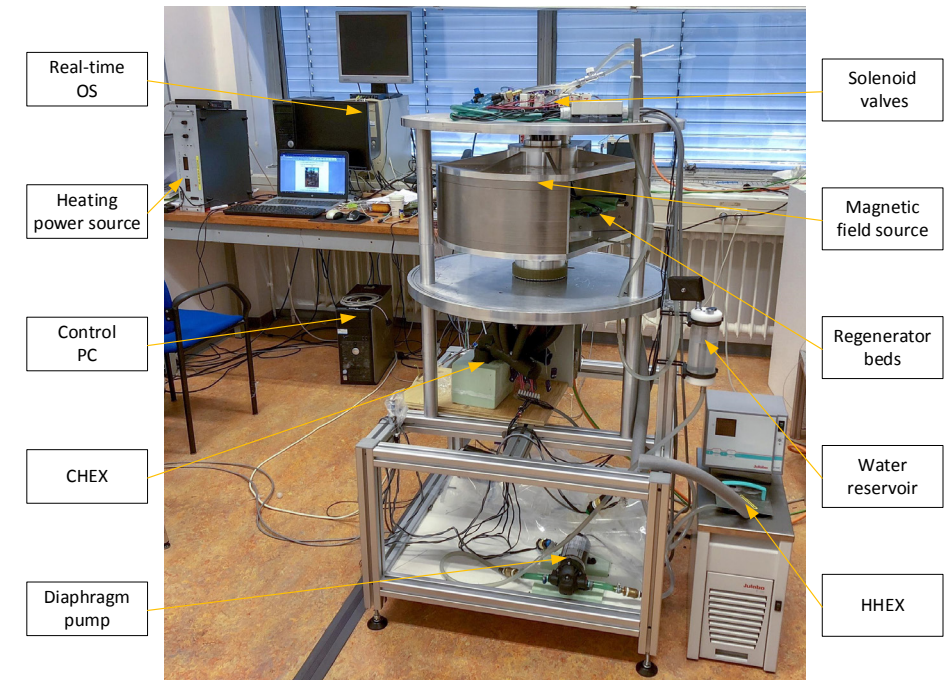


Figure 4.1: Configuration of FAME Cooler.

Different from the horizontal designs [13, 26], the architecture of the FAME Cooler employs a vertical orientation [14, 16, 27-29]. Thus, the mechanical components are stacked around a central shaft, and the HTF in the hydraulic system flows within a loop with a height difference. This design benefits both the current intensive experimental

works and the future extensions. For instance, all components in the hydraulic system such as the regenerator, the hydraulic tubes, the sensors, and even the valves can be accessed easily, and modification can be done in minutes.

The core system of the FAME Cooler consists of a magnetic field source, an AMR regenerator, and a hydraulic system, as shown in Fig. 4.2. The magnetic field source which is the rotary part of this prototype is driven by a DC servo motor with a gearbox via a timing belt-pulley structure (total gear ratio is 1:48), while a belt tensioner is applied for accurate positioning. This structure can generate a periodic magnetic field for the AMR cycle with a frequency up to 3 Hz. The regenerator is fixed on the central shaft and sited right in the middle of the air gap of the magnetic field source. Seven compartments which are called regenerator beds are mounted on the bracket of the regenerator, with an angular interval of 51.4° . Both the bracket and the regenerator beds are made of fiberglass epoxy laminate in order to avoid the formation of eddy current and provide better thermal insulation. The hydraulic system is shown on the right side of Fig. 2. On both sides of each regenerator bed, a pair of programmable DC solenoid valves are installed to control the working cycle of the bed, which is synchronized with the rotary frequency of the magnetic field source. Under the working condition, the solenoid valves sequence maintains a cyclic reciprocating flow within the AMR regenerator but continuous unidirectional flow in the outside stream. At the cold end of the system, a heat exchanger (CHEX) with a cartridge heater as the insert is insulated with polystyrene foam. The cartridge heater here is used to mimic the heat load for performance analysis. At the hot end of the system, a heat exchanger (HHEX) with a thermostatic bath is invoked to regulate both the initial temperature and the hot end temperature of the hydraulic system, which is also the sink of the rejected heat from the regenerator. A DC diaphragm pump with an attached flow meter can generate a volume flow rate up to 5 l min^{-1} under working conditions. Thermocouples are attached to both sides of each regenerator bed, as well as the cold and hot end of the system. Two pressure gauges are placed at the outlet of the pump and the outlet of the regenerator cold side, to measure the pressure drop across the regenerator. The HTF used in this prototype is deionized water with 1% of Sentinel X100 corrosion inhibitor, as suggested by Forchelet and coworkers [30]

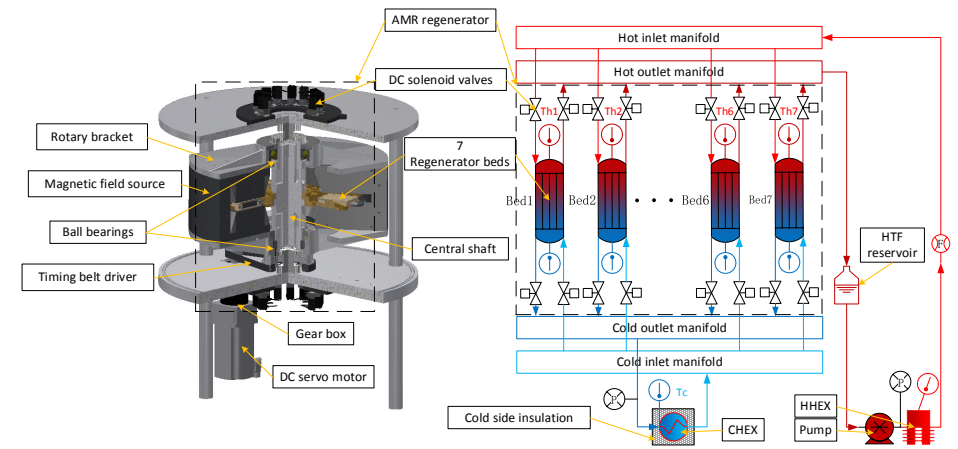


Figure 4.2: Architecture of the FAME Cooler.

4.2.1 Magnetic field source

The magnetic field source consists of two fan-shaped magnet assemblies that are symmetrically placed in an aluminum rotary bracket as shown in Fig. 4.3.

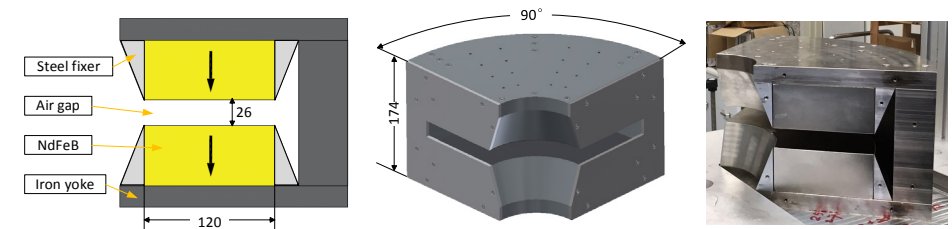


Figure 4.3: Magnet field source.

Two pieces of grade N50m NdFeB magnets with the same magnetization direction are glued in parallel into a field-conducting electric soft iron yoke. Four pieces of stainless-steel frames are placed in front and behind the NdFeB magnet pieces to fix its horizontal position. Two stainless steel side plates are used to support the whole structure. The two magnet assemblies divide the whole rotary plane into four sectors of 90° , with two high-field, and two low-field ranges. When rotated, the four sectors will sweep on each regenerator bed, resulting in alternating magnetic fields. For each assembly, an average field density of 0.875 T over an air gap of 26 mm height and 120 mm deep with a volume of 0.71 l is generated. The detailed field distribution can be seen in Fig. 4.4. This dotted profile of the magnetic field density is measured with a 2D Hall probe as a function of

azimuthal angle, while the solid curve is a simulation result from the FEM measurement of Ansys. Although the peak value of the field density within high field range is lower than most of the existing designs (such as 1.5 T for the device of UF [31], 1.47 T for UVic [8], 1.25 T for UNISA [32], 1.24 T for DTU [33], 1 T for UFSC [13]), the field plateaus are more stable and extended. For the high field region of this design, the largest variation is only 6.5% from the maximal field density through the whole high field range (60 degrees) for FAME Cooler. However, this number exceeds 15% over 60 degrees for the device of UNISA (Aprea et al., 2014), 72% for the device of UFSC (Lozano et al., 2016). For the low field range of the this design, due to the open space between two magnetic assemblies, the field density remains zero (only background magnetic field of the earth), but for all the Halbach type magnets, this is unachievable. This feature can improve the timing of the AMR cycle, as the boundary between high and low field range is sharper, so that the magnetization/demagnetization process can be completed before the flow of HTF starts. Moreover, because of the simple design, the cost and the complexity of construction are greatly reduced, compared to devices with Halbach type magnets [34].

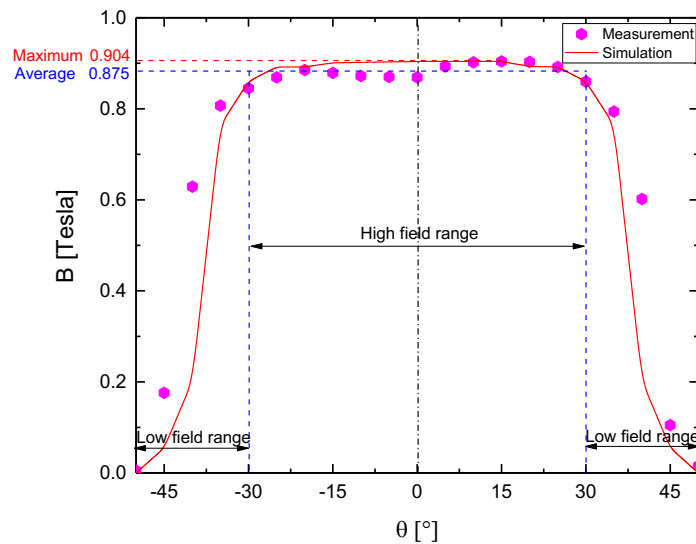


Figure 4.4: Density profile of the magnetic field in the air gap.

4.2.2 Regenerator

The regenerator is designed in an asymmetric layout with consideration of both performance and usability. As shown in Fig. 4.5, seven regenerator beds made of fiberglass with a capacity of 35.1 ml are mounted on a dish like bracket, as the odd number can significantly reduce sudden changes in the magnetic torque [12], when the regenerator

is entering and exiting the high field range. Each bed has four tube connectors attached, which significantly reduce the dead volume between the regenerator and the cold and hot end of the system. All the seven beds can be installed or removed, either in groups or individually, so that different material combinations and different working procedures can be implemented. The current MCM packed bed is fabricated from epoxy bonded gadolinium spheres with a porosity of 36%, the ratio between the epoxy (Three Bond 2273D Thixotropic Single Component Epoxy Resin) and the MCM is 5:1000. This ensures a good packing density, while the pressure drop across the regenerators stays at a low level, the detailed value of system pressure will be shown in experiment section. For each regenerator bed, two type-E thermocouples are attached to both sides of the bed to measure the resulting temperature of each AMR cycle.

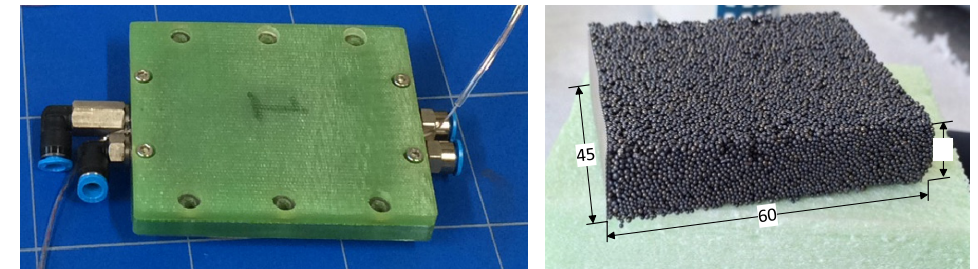


Figure 4.5: Regenerator bed and the bonded MCM.

4.2.3 Flow control system

The flow control system is the part which brings the greatest potential to the whole device. As shown in Fig. 4.6, 28 DC solenoid valves are mounted on the two disks which are placed opposite to each other. The on/off state of the valves are controlled by a Phar Lap ETS real-time controller communicating with the optical encoder of the servo motor. In the meantime, the pump speed is also real-timely adjusted by the real-time controller via Pulse-Width Modulation (PWM) method to ensure a constant flow rate. Regarding the working process, the motor is continuously working at a fixed speed, and each regenerator bed undergoes an independent AMR cycle, in which the operational timing and duration of any valve can be changed by the program or manually, while the pumping power output is adjusted according to the real-time pressure. This configuration allows a comprehensive control of the flow profile of each regenerator bed. This function is not only limited to the blow fraction mentioned by [35], but also includes the phase difference between the magnetic field profile and the flow profile, and even reversing the cold and hot end of the system. This feature enables easy switching between a refrigerator and a heating heat pump operation.

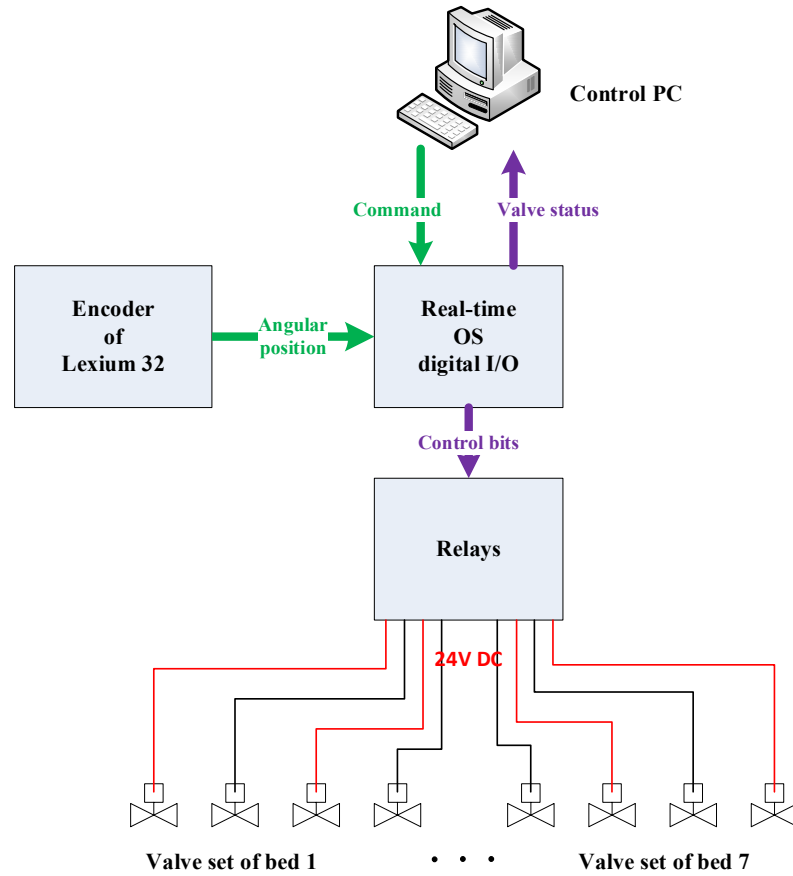


Figure 4.6: control system block diagram of FAME Cooler

4.2.4 MCM properties

In the regenerator of the FAME Cooler, each bed has been filled with 169 g gadolinium spheres with a size in the range of 400-800 μm , which are provided by Baotou research institute of rare earth, China.

The properties of the gadolinium spheres are shown in Fig. 4.7. Under an applied field of 1 T, a peak entropy change of $2.97 \text{ J kg}^{-1} \text{ K}^{-1}$ has been measured directly, and a peak adiabatic temperature change of 3.54 K has been calculated from the measured entropy and specific heat. The lower property values of the employed gadolinium in comparison with the pure Gd measured by Dan'kov and coworkers [36], may be due to a lesser purity. The specific heat and entropy change data are measured with a Halbach cylinder based in-field DSC setup, which is similar to the device built by Porcari and coworkers [37]. In this setup, the iso-field calorimetric scans were performed at a rate of 20 mK min^{-1} under different applied magnetic fields.

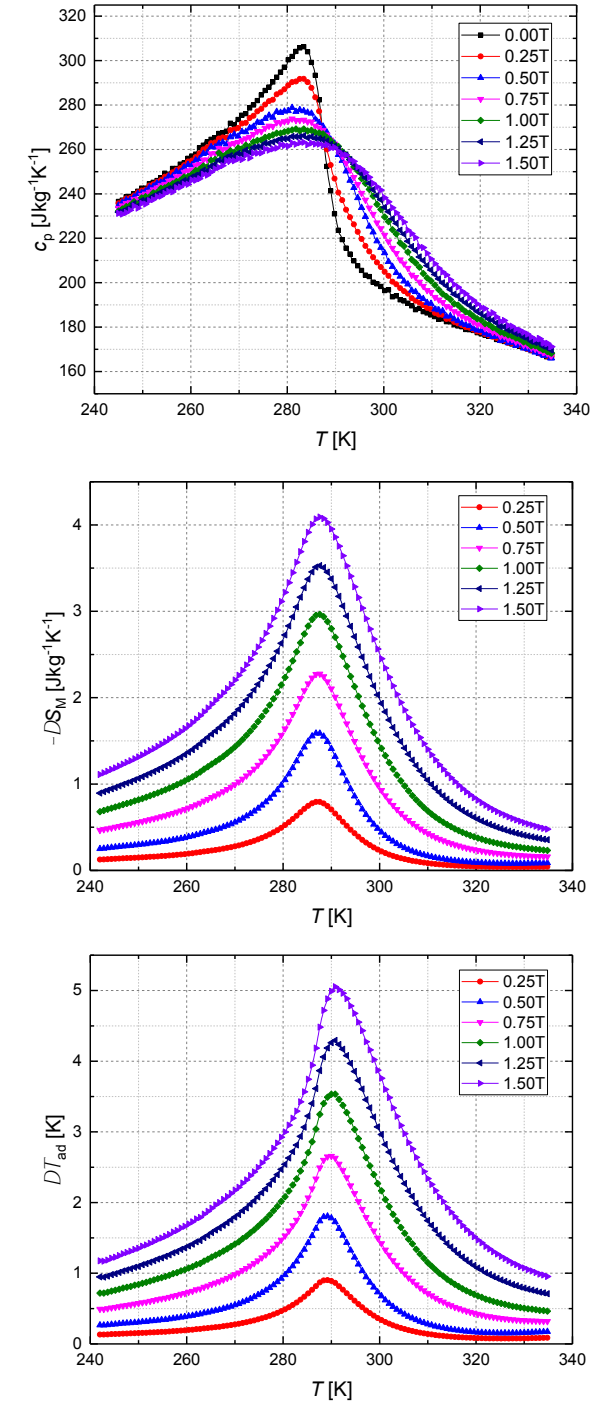


Figure 4.7 Properties of the Gd spheres: (a) specific heat from direct measurements, (b) entropy change from the integration of the specific heat, (c) adiabatic temperature change calculated from the above two.

4.3 PERFORMANCE METRICS

Table 1 summarizes the specifications of the FAME Cooler. Based on this, the performance metrics are defined. In this study, the temperature span ΔT_{span} is always referring to the system temperature span,

$$\Delta T_{span} = T_H - T_C \quad (4-1)$$

where T_H and T_C represent the outlet temperature of the system hot end and cold end, respectively. As tested in the developing stage, the flow rate difference between each regenerator bed is less than 4%, and there is always measurement error for each hot side temperature of the regenerator beds, for a more representative evaluation, here we consider

$$T_H = \frac{\sum_{i=1}^7 T_{hi}}{7} \quad (4-2)$$

The temperature of system hot end is calculated by an average over all hot side outlets temperatures of all beds for each time step, while the temperature of the system cold end T_C is directly measured by the thermocouple, see Fig. 2. All the temperature data are acquired with a National Instruments DAQ system (NI 9213) combined with Omega type-E thermocouples.

Table 1 FAME Cooler specifications.

Property	Range/content	Units
Magnetic field (average)	0-0.875	T
AMR frequency	0-3	Hz
Volume flow rate	0-5	lmin^{-1}
Available regenerator bed	7	-
Regenerator bed volume (each)	35.1	cm^3
Heat transfer fluid	water (with 1% of Sentinel X100)	-
MCM properties for current experiments:		
Composition	Gadolinium	-
Geometry	Spheres	-
Diameter	400-800	μm
Porosity	36%	-
Mass (total)	1.18	kg

As an experimental platform, the motor and pump for this prototype have been selected with the scalability taken into consideration. Therefore, it is not accurate to use energy consumption directly for performance calculation. To achieve higher reliability, the output power of the motor is calculated as the work on the shaft with a steady rotary

frequency,

$$P_{motor} = \omega \Gamma R = 2\pi f_{mag} \Gamma R = \pi f_{AMR} \Gamma R \quad (4-3)$$

where Γ is the torque applied on the motor shaft, $f_{AMR} = 2f_{mag}$ is the rotary frequency of the magnet, and $f_{AMR} = 2f_{mag}$ (as two high field and low field ranges are generated for one revolution of the magnetic field source), R is the speed ratio between the motor and the rotary magnetic field source. The torque of the motor is measured by the inbuilt torque sensor of the servo driver (Schneider Lexium 32).

The work done by the pump is calculated as the work for generating the pressure difference while maintaining the volume flow rate,

$$P_{pump} = \Delta P \dot{V}_{HTF} \quad (4-4)$$

Here the pressure difference ΔP is measured as the difference between the readings of the two pressure gauges (AB Elektronik 96760, 0-6 bar), which are placed at the cold and hot end, respectively. The HTF flow rate \dot{V}_{HTF} is the total volume flow rate of the system, which is measured at the outlet of the pump with a Hall effect flow meter (Digiten FL-S402B 0.3-10 lmin^{-1}).

The system coefficient of performance, COP is defined as,

$$COP = \frac{P_{cool}}{P_{motor} + P_{pump}} \quad (4-5)$$

where the cooling power P_{cool} is measured as the input power of the insulated cartridge heater at the system cold end when energy equilibrium is reached. Besides, the COP here is simplified by ignoring the mechanical efficiency of the motor and pump.

The data measurement system and the driving system are plugged on different power supplies to reduce the high-frequency noise in the measurement data. A detailed summary of the measured data and the sensors are listed in table 2.

Table 2 Characteristics of the sensors used and their precision.

Quantity	Characteristic	Precision
Mass	Electronic balance	± 0.1 [g]
Temperature	Type-E thermal couple and NI 9213	± 0.15 [K]
Volume flow rate	Hall effect flowmeter	$\pm 2\%$
Pressure drop	Pressure gauge	$\pm 3\%$
Torque	Torque transducer	$\pm 1\%$
AMR frequency	Optical encoder	± 0.001 [$^\circ\text{s}^{-1}$]
Cooling power	Cartridge heater and Delta SM300-10 D	$\pm 0.5\%$

4.4 EXPERIMENT AND DISCUSSION

For mapping the performance of the prototype, three groups of different utilization conditions coupled with the most representative control parameters have been selected, together with the resulting system characteristics as listed in table 3. The utilization here is calculated as

$$\Phi = \frac{\rho_{HTF} c_{HTF} \dot{V}_{HTF}}{f_{AMR} m_{MCM, tot} c_{MCM}} \quad (4-6)$$

where for the HTF, density ρ_{HTF} is 1000 kg m⁻³, specific heat c_{HTF} is 4200 Jkg⁻¹K⁻¹. For the MCM, specific heat c_{MCM} is 235 Jkg⁻¹K⁻¹ and the total mass of the MCM $m_{MCM, tot}$ is 1.18 kg.

Table 3 Experimental conditions for the three selected conditions (A, B and C) with Φ the utilization, f_{AMR} the AMR frequency, \dot{V}_{HTF} the volume flow rate of HTF, Γ the torque of the motor, and ΔP the system pressure drop

Groups	Φ	f_{AMR} (Hz)	\dot{V}_{HTF} (lmin ⁻¹)	Γ (Nm)	ΔP (Bar)
A	0.06	0.5	1.18	0.34	1.12
B	0.15	1.2	1.84	0.29	1.31
C	0.25	1.7	4.34	0.34	2.26

Different experiments were then performed by varying the hot end temperature or applying different thermal loads on the CHEX. The room temperature was maintained within a range between 296 and 300 K with a ventilation system. To show the results in a steady-state condition, all the data points presented here were average values over the last 300 seconds, which were measured after the fluctuations of signals were of the same amplitude as the measurement accuracy. As suggested by Fortkamp and coworkers [35], the blow fraction (a time fraction of the AMR cycle during which there is flow in the regenerator) of the HTF has a significant influence on the performance, therefore, for simplifying the result comparison, the flow fraction in the experiments mentioned in this paper was fixed at 60%.

The experiments start with the condition of zero load at the cold end, the temperature of the hot end is set at the designated temperature with the assistance of a thermostatic bath (T_{bath}). Then, all the regenerator beds are flushed with a cyclic flow until the temperature in each bed is as close to T_{bath} as possible. Here, the cyclic flow means the same flow profile and the same valve switching procedure as during the normal working process, but without rotation of the magnetic field source. After that, FAME Cooler is started with one of the three specified utilization conditions, and will continuously work until the temperature span between the cold end T_C and hot end T_H no longer changes.

Throughout the whole process, the hot end temperature T_H is maintained within a small range (a mean absolute deviation less than 0.5 K) around the designated temperature. Finally, the HTF flow and the rotation of the magnetic field source are both stopped, then the regenerator beds are cooled to room temperature with a cyclic flow.

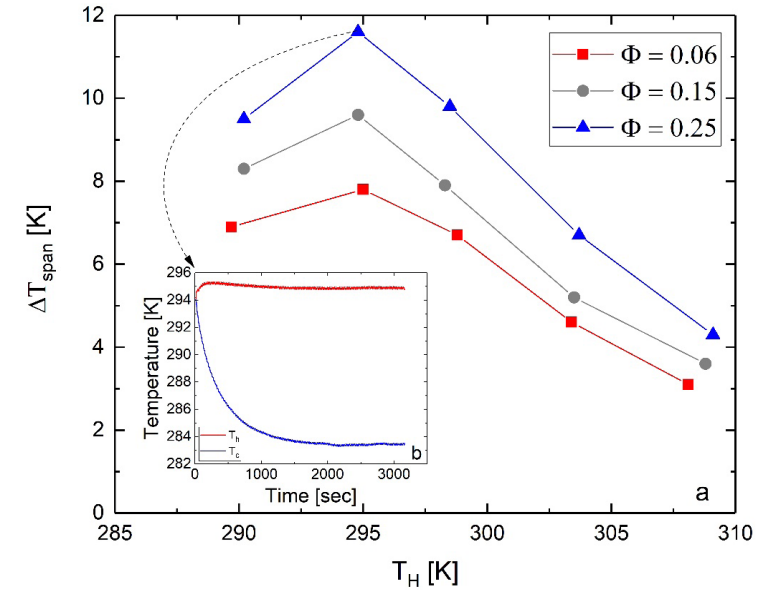


Figure 4.8 Temperature span as a function of the hot-end temperature under different utilization conditions: (a) temperature span versus hot-end temperature, (b) development profile of temperature span over time at $\Phi = 0.25, T_H = 294.8$ K

As can be seen from Fig. 4.8 (a), the temperature span increases with increasing utilization for each hot-end temperature T_H , due to a larger cooling power being achieved at a higher working frequency and with a larger flow rate. Besides, the maximum zero-load temperature span is observed for all three utilizations when the temperature of the hot end T_H is around 295 K with values of 11.6 K at $\Phi = 0.25$, 9.6 K at $\Phi = 0.15$, 7.8 K at $\Phi = 0.06$, respectively. This hot-end temperature is higher than the Curie temperature of the MCM indicated in Fig. 7. As suggested by Nielsen and coworkers [38], there is an offset between the maxima of the curves for temperature dependent adiabatic temperature-change under magnetization and demagnetization condition. Therefore, a higher T_H can result in a better temperature profile distribution in the regenerator between magnetization and demagnetization process. Evolution with the time of the temperature span under the condition of $\Phi = 0.25, T_H = 294.8$ K is shown in Fig. 4.8 (b) as an insert.

To further explore the performance of the FAME Cooler, the cooling power is measured by applying the cartridge heater in the CHEX. In this case, the hot end temperature is maintained at 295 K, the optimized temperature of the hot end determined from the earlier experiments. Then, we followed the same procedure as in the previous experiment until the system reaches the maximum temperature span. Additionally, a series of thermal loads are applied on the CCEX by energizing the cartridge heater, starting from 25 W with an increment of 25 W until the zero-span cooling power of the prototype is reached. After each thermal load is applied, the temperature profile of the FAME Cooler is continuously measured until the temperature fluctuations are of the same amplitude as the measurement accuracy. Then the next thermal load is applied.

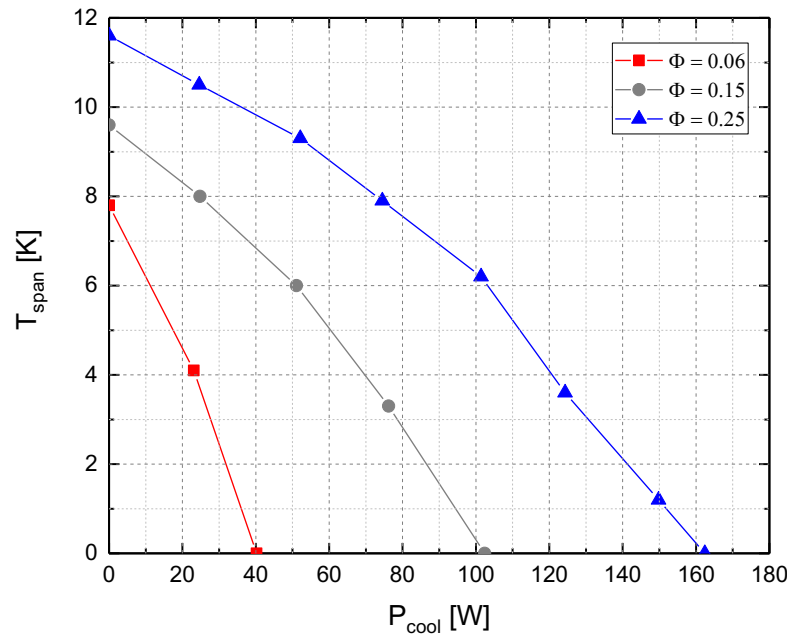


Figure 4.9 Temperature span as a function of the cooling power under different utilization conditions.

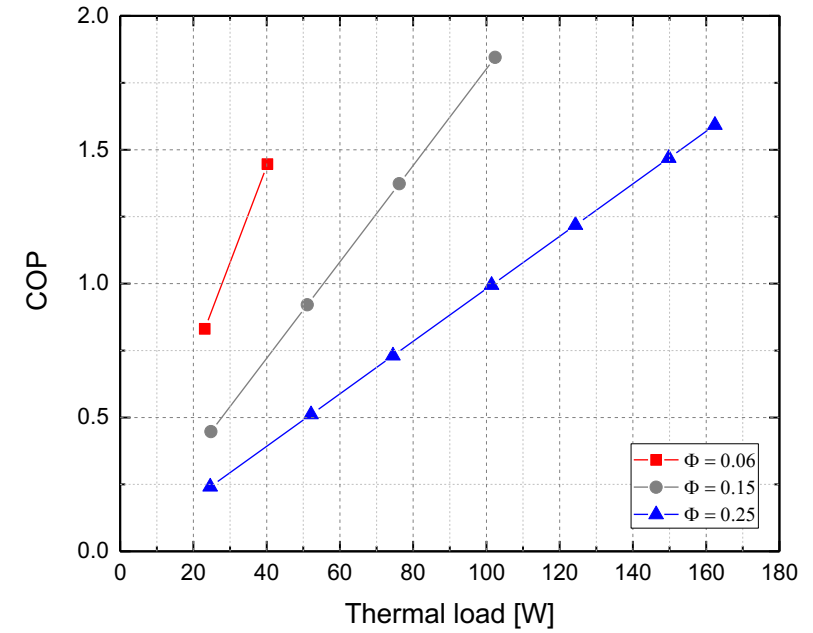


Figure 4.10 COP as a function of the thermal load under different utilization conditions.

From Fig. 4.9 and 4.10 it is clear that the temperature span decreases when the heat load increases. For group A with $\Phi = 0.06$, the zero-span cooling power is 40.2 W, with a COP of 1.45, for group B with $\Phi = 0.15$, the zero-span cooling power is 102.4 W, with a COP of 1.85, and for group C with $\Phi = 0.25$, the zero-span cooling power is 162.4 W, with a COP of 1.59, respectively. It can be seen that the case with the highest cooling power does not have the highest COP, which is caused by the increased dissipation due to the hydraulic resistance and mechanical friction. Together with the high AMR frequency and larger flow rate, the torque on the shaft of the motor and the pressure drop across the hydraulic system also becomes large. This causes a reduction in the efficiency of the mechanical system. Therefore, the result indicates that the system has a better energy conversion rate under the conditions of group B. Besides, in Fig. 9, the nonlinear relation between the cooling power and the temperature span, which is more significant at the higher temperature span value, indicates that parasitic losses [39] become higher due to a larger temperature span (a larger difference between the room temperature T_{room} and the temperature of the cold end T_c).

Above all, although the maximum temperature span of this device is not maximized due to the relatively low magnetic field density, the performance parameters like the cooling power and the COP are still comparable to other devices that are considered

to be innovative in the world. For example, a maximum temperature span of 7.1 K and a cooling power of 80.4 W for the device of UFSC [13]; a maximum temperature span of 11.9 K and a maximum COP of 2.5 with a cooling power of 200 W for the device of UNISA [11]; a maximum temperature span of 21 K and the maximum cooling power of 26 W at a span of 1 K for the device of UF [31].

It should however be noted that the usage of solenoid valves (2 W each) is a complementary source of heat input and energy consumption which increases with the working frequency. However, the solenoid valves used here are normal closed valves, which means they are energized only when opened. Therefore, the 2 W energy consumption is valid only when the valve is switched on, otherwise, the valves use zero energy. Normally, there are 2-4 regenerator beds (depends on the angular position of the magnetic field source and the duration of the opening) connected to the main hydraulic loop, for each bed, there are two valves opened. Therefore, in the worst situation, eight valves are energized simultaneously, which is 16 W, but most of the time, the value is less. Besides, the solenoid valves implemented in this prototype are for experimental flexibility reason, but not for an efficiency point of view. As a result, the small part of heat input/energy consumption is neglect from system efficiency calculation.

Besides, because of the open design of the magnet assembly, the thermal insulation for the regenerator is incomplete, the influence of the room temperature can be much more than in compact designs [13, 26]. Therefore, in future experiments, a climatic lab condition will be prepared for better performance and improved precision. The relation between the flow profile and the performance of the system will be further explored in future experiments.

4.5 SYSTEM FINE-TUNING AND THE RESULT

The advantage of the combination of real-time system, servo motor, and the solenoid valves is the control flexibility of the working cycle. As shown in Fig. 4.11 the phase difference between the magnetic field profile and the HTF flow profile can be easily adjusted, while the shape of flow profile itself can also be adjusted, which makes the exploration of the influence of different working cycle possible for the FAME Cooler.

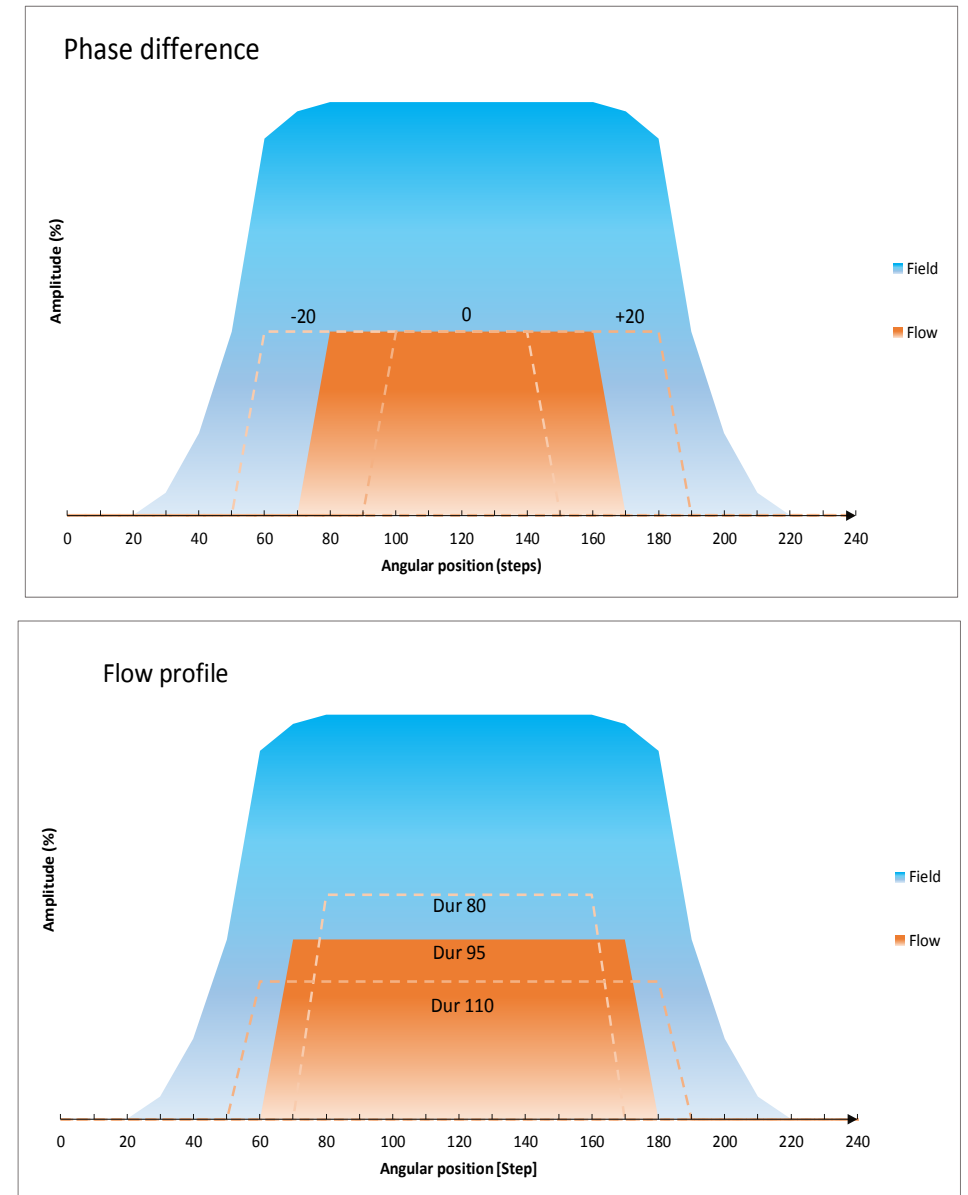


Figure 4.11 control parameter configuration for fine-tuning the FAME Cooler

As shown in Fig. 4.11 (a) the full coverage of the high field region is 196 position steps (equals to 100° in angular position), which is shown with the blue area. The default control setting is, the flow profile central aligned with the high field region and has a duration of 95 position steps, which is shown with the orange area. In the tuning experiment, we compared the performance results by offsetting the timing of flow region 20 position steps early and 20 position steps with regard to the field profile. In the other set of experiment shown in Fig. 4.11(b), we kept the center of the flow region the same and changing the timing and duration of the flow region. To make a fair comparison, the total displacement of HTF was kept constant, which is shown with the changing shape of flow region, the region is shorter when the flow rate is higher, while the region is longer when the flow rate is lower. All experiments have been configured with the working frequency 1 Hz and 26°C hot side temperature, while flow rate is notified with utilization (U), the timing difference is notified with phase differences. The results are shown in Fig. 4.12 as temperature span vs cooling power plots, where subplot a, b, and c show the result of duration from 85 to 110, respectively.

From Fig. 4.12(a), we can see that when the duration fixed at 85 position steps, high utilization results in best overall performance, both in temperature span and cooling power. Regarding the timing of the flow, the delayed flow (phase +20) has the best performance, while the hasted (phase -20) flow results in the worst performance in both medium and higher utilization. However, in the low utilization case the trend is not the same, where delayed flow (phase +20) performs the worst.

From Fig. 4.12(b) we can see that when the duration increases to 95 position steps, the performance of all cases is a bit worse than the previous cases. Timing wise, however, the default setting (phase 0) has the best performance, while the delayed (phase +20) flow results in the worst performance in all the cases, especially when the heat load is high. In Fig. 4.12(c) the cases widely spread over the plot. This time, in all cases, the hasted (phase -20) flow results the best performance in all utilization cases, while the delayed (phase +20) flow results in the worst performance in all the cases. Moreover, in this set of experiment, most of the control parameter sets cannot generate cooling power above 60W, while this doesn't happen to the experiment set with duration 80 and 95.

We can conclude from the result above that, the longer the duration of the flow, the more sensitive the performance affected by the control parameters. This phenomenal is more pronounced while the heat load is low, but become irrelevant when the heat load is high. When the flow duration is shorter, the timing for starting the flow during the magnetization better to be latter, while when the duration is longer, the starting of the flow should be early. Besides, with shorter flow duration, one can tune the heat pump systems more precisely better performance (temperature span and cooling power). However, when the

heat load is high, the tuning becomes less effective. When the flow duration is too long, the system become less efficient due the worse timing between magnetic and flow profile. There is also some inconsistency with the experimental dataset listed above. This is mainly due to the utilization control is not very accurate with diaphragm pump.

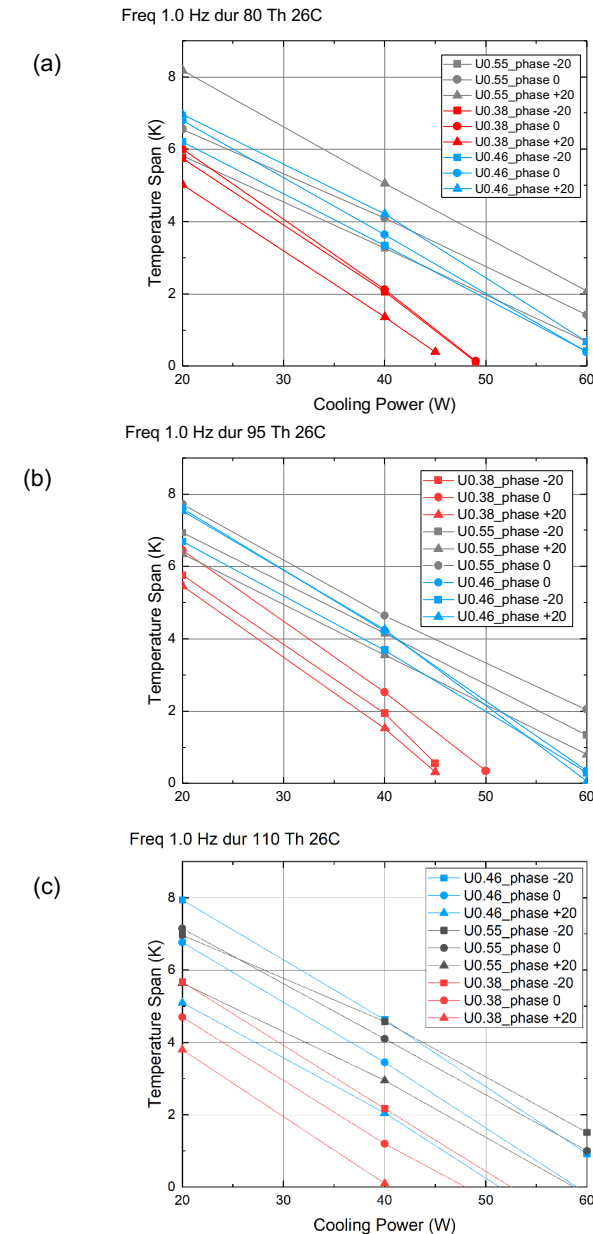


Figure 4.12 Fine-tuning results of the FAME Cooler

4.6 CONCLUSIONS

A rotary room-temperature AMR prototype named the FAME Cooler was developed to investigate the magnetocaloric properties of different materials, as well as to further explore the RT MR technology. This device maximizes the control flexibility of the AMR cycles, not only the well-known working frequency, flow rate, and the temperature of the hot end, but also the blow fraction, the phase offset, and even the switching between cooling or heat-pump operation. As an experimental platform, the device gives great freedom to modify the regenerator. For instance, it is simple to replace the MCM in the regenerator beds and to change the number of beds installed. The performance of this device is found to be promising compared to other devices of the same scale around the world. With gadolinium as the MCM, on the condition of an AMR frequency of 1.7 Hz, a flow rate of 4.34 lmin^{-1} , a hot end temperature of 295 K and a utilization of 0.25, the maximum zero power temperature span is 11.6 K, the maximum zero-span cooling power is 162.4 W, and the simplified COP is 1.59. The maximum simplified COP of 1.85 is found for a utilization of 0.15, an AMR frequency of 1.2 Hz and a flow rate of 1.84 lmin^{-1} . Fine-tuning system control parameters can further optimize performance. The duration of the flow significantly affects performance, especially at low heat loads. Shorter flow duration allows for precise tuning towards larger temperature spans. However, tuning with flow control parameters becomes more difficult under high heat load.

REFERENCE

- [1] G.V. Brown, Magnetic Heat Pumping near Room-Temperature, *Journal of Applied Physics*, 47 (1976) 3673-3680.
- [2] A. Kitanovski, U. Plaznik, J. Tusek, A. Poredos, New thermodynamic cycles for magnetic refrigeration, *International Journal of Refrigeration-Revue Internationale Du Froid*, 37 (2014) 28-35.
- [3] W.A. Steyert, Stirling-Cycle Rotating Magnetic Refrigerators and Heat Engines for Use near Room-Temperature, *Journal of Applied Physics*, 49 (1978) 1216-1226.
- [4] G. Green, J. Chafe, J. Stevens, J. Humphrey, Gadolinium-terbium active regenerator, 1990.
- [5] N. Hirano, S. Nagaya, M. Takahashi, T. Kuriyama, K. Ito, S. Nomura, Development of magnetic refrigerator for room temperature application, *Advances in Cryogenic Engineering*, Vol 47, Pts a and B, 613 (2002) 1027-1034.
- [6] R. Bjork, C.R.H. Bahl, A. Smith, N. Pryds, Review and comparison of magnet designs for magnetic refrigeration, *International Journal of Refrigeration-Revue Internationale Du Froid*, 33 (2010) 437-448.
- [7] B.F. Yu, M. Liu, P.W. Egolf, A. Kitanovski, A review of magnetic refrigerator and heat pump prototypes built before the year 2010, *International Journal of Refrigeration-Revue Internationale Du Froid*, 33 (2010) 1029-1060.
- [8] A. Rowe, A. Tura, Experimental investigation of a three-material layered active magnetic regenerator, *International Journal of Refrigeration-Revue Internationale Du Froid*, 29 (2006) 1286-1293.
- [9] Z.G. Zheng, H.Y. Yu, X.C. Zhong, D.C. Zeng, Z.W. Liu, Design and performance study of the active magnetic refrigerator for room-temperature application, *International Journal of Refrigeration-Revue Internationale Du Froid*, 32 (2009) 78-86.
- [10] I. Park, Y. Kim, S. Jeong, Development of the tandem reciprocating magnetic regenerative refrigerator and numerical simulation for the dead volume effect, *International Journal of Refrigeration-Revue Internationale Du Froid*, 36 (2013) 1741-1749.
- [11] C. Aprea, A. Greco, A. Maiorino, C. Masselli, The energy performances of a rotary permanent magnet magnetic refrigerator, *International Journal of Refrigeration-Revue Internationale Du Froid*, 61 (2016) 1-11.
- [12] D. Eriksen, K. Engelbrecht, C.R.H. Bahl, R. Bjork, K.K. Nielsen, A.R. Insinga, N. Pryds, Design and experimental tests of a rotary active magnetic regenerator prototype, *International Journal of Refrigeration-Revue Internationale Du Froid*, 58 (2015) 14-21.
- [13] J.A. Lozano, M.S. Capovilla, P.V. Trevizoli, K. Engelbrecht, C.R.H. Bahl, J.R. Barbosa, Development of a novel rotary magnetic refrigerator, *International Journal of Refrigeration-Revue Internationale Du Froid*, 68 (2016) 187-197.
- [14] T. Okamura, K. Yamada, N. Hirano, S. Nagaya, Performance of a room-temperature rotary magnetic refrigerator, *International Journal of Refrigeration-Revue Internationale Du Froid*, 29 (2006) 1327-1331.
- [15] C. Zimm, A. Boeder, J. Chell, A. Sternberg, A. Fujita, S. Fujieda, K. Fukamichi, Design and performance of a permanent-magnet rotary refrigerator, *International Journal of Refrigeration-Revue Internationale Du Froid*, 29 (2006) 1302-1306.
- [16] J. Tusek, S. Zupan, A. Sarlah, I. Prebil, A. Poredos, Development of a rotary magnetic refrigerator, *International Journal of Refrigeration-Revue Internationale Du Froid*, 33 (2010) 294-300.
- [17] S. Jacobs, J. Auringer, A. Boeder, J. Chell, L. Komorowski, J. Leonard, S. Russek, C. Zimm, The performance of a large-scale rotary magnetic refrigerator, *International Journal of Refrigeration-Revue Internationale Du Froid*, 37 (2014) 84-91.
- [18] C. Aprea, A. Greco, A. Maiorino, An application of the artificial neural network to optimise the energy performances of a magnetic refrigerator, *International Journal of Refrigeration-Revue Internationale Du Froid*, 82 (2017) 238-251.
- [19] X.N. He, M.Q. Gong, H. Zhang, W. Dai, J. Shen, J.F. Wu, Design and performance of a room-temperature hybrid magnetic refrigerator combined with Stirling gas refrigeration effect, *International Journal of Refrigeration-Revue Internationale Du Froid*, 36 (2013) 1465-1471.
- [20] M. Balli, O. Sari, C. Mahmed, C. Besson, P. Bonhote, D. Duc, J. Forchelet, A pre-industrial magnetic cooling system for room temperature application, *Applied Energy*, 98 (2012) 556-561.
- [21] J.A. Barclay, Use of a Ferrofluid as the Heat-Exchange Fluid in a Magnetic Refrigerator, *Journal of Applied Physics*, 53 (1982) 2887-2894.
- [22] J.R. Gomez, R.F. Garcia, J.C. Carril, M.R. Gomez, A review of room temperature linear reciprocating

- magnetic refrigerators, *Renewable & Sustainable Energy Reviews*, 21 (2013) 1-12.
- [23] E. Bruck, O. Tegus, D.T.C. Thanh, K.H.J. Buschow, Magnetocaloric refrigeration near room temperature (invited), *Journal of Magnetism and Magnetic Materials*, 310 (2007) 2793-2799.
- [24] S. Fujieda, A. Fujita, K. Fukamichi, Large magnetocaloric effect in $\text{La}(\text{Fe}_{1-x}\text{Si}_x)_{13}$ itinerant-electron metamagnetic compounds, *Applied Physics Letters*, 81 (2002) 1276-1278.
- [25] V.K. Pecharsky, K.A. Gschneidner, Giant magnetocaloric effect in $\text{Gd}_5(\text{Si}_2\text{Ge}_2)$, *Physical Review Letters*, 78 (1997) 4494-4497.
- [26] C.R.H. Bahl, K. Engelbrecht, D. Eriksen, J.A. Lozano, R. Bjork, J. Geyti, K.K. Nielsen, A. Smith, N. Pryds, Development and experimental results from a 1 kW prototype AMR, *International Journal of Refrigeration-Revue Internationale Du Froid*, 37 (2014) 78-83.
- [27] C. Aprea, A. Greco, A. Maiorino, GeoThermag: A geothermal magnetic refrigerator, *International Journal of Refrigeration-Revue Internationale Du Froid*, 59 (2015) 75-83.
- [28] D.S. Arnold, A. Tura, A. Ruebsaat-Trott, A. Rowe, Design improvements of a permanent magnet active magnetic refrigerator, *International Journal of Refrigeration-Revue Internationale Du Froid*, 37 (2014) 99-105.
- [29] P. Govindappa, P.V. Trevizoli, I. Niknia, T.V. Christiaan, R. Teyber, A. Rowe, Experimental characterization of multilayer active magnetic regenerators using first order materials: Multiple points of equilibrium, *Journal of Applied Physics*, 124 (2018) 134901.
- [30] J. Forchelet, L. Zamni, S.E. El Alami, J. Hu, M. Balli, O. Sari, Corrosion behavior of gadolinium and La-Fe-Co-Si compounds in various heat conducting fluids, *International Journal of Refrigeration-Revue Internationale Du Froid*, 37 (2014) 307-313.
- [31] M.A. Benedict, S.A. Sherif, D.G. Beers, M.G. Schroeder, Design and performance of a novel magnetocaloric heat pump, *Science and Technology for the Built Environment*, 22 (2016) 520-526.
- [32] C. Aprea, A. Greco, A. Maiorino, R. Mastrullo, A. Tura, Initial experimental results from a rotary permanent magnet magnetic refrigerator, *International Journal of Refrigeration-Revue Internationale Du Froid*, 43 (2014) 111-122.
- [33] C.R.H. Bahl, K. Engelbrecht, R. Bjork, D. Eriksen, A. Smith, K.K. Nielsen, N. Pryds, Design concepts for a continuously rotating active magnetic regenerator, *International Journal of Refrigeration-Revue Internationale Du Froid*, 34 (2011) 1792-1796.
- [34] A. Tura, A. Rowe, Permanent magnet magnetic refrigerator design and experimental characterization, *International Journal of Refrigeration-Revue Internationale Du Froid*, 34 (2011) 628-639.
- [35] F.P. Fortkamp, D. Eriksen, K. Engelbrecht, C.R.H. Bahl, J.A. Lozano, J.R. Barbosa, Experimental investigation of different fluid flow profiles in a rotary multi-bed active magnetic regenerator device, *International Journal of Refrigeration-Revue Internationale Du Froid*, 91 (2018) 46-54.
- [36] S.Y. Dan'kov, A.M. Tishin, V.K. Pecharsky, K.A. Gschneidner, Magnetic phase transitions and the magnetothermal properties of gadolinium, *Physical Review B*, 57 (1998) 3478-3490.
- [37] G. Porcari, M. Buzzi, F. Cugini, R. Pellicelli, C. Pernechele, L. Caron, E. Bruck, M. Solzi, Direct magnetocaloric characterization and simulation of thermomagnetic cycles, *Review of Scientific Instruments*, 84 (2013) 073907.
- [38] K.K. Nielsen, C.R.H. Bahl, A. Smith, Constraints on the adiabatic temperature change in magnetocaloric materials, *Physical Review B*, 81 (2010) 054423.
- [39] J.A. Lozano, K. Engelbrecht, C.R.H. Bahl, K.K. Nielsen, D. Eriksen, U.L. Olsen, J.R. Barbosa, A. Smith, A.T. Prata, N. Pryds, Performance analysis of a rotary active magnetic refrigerator, *Applied Energy*, 111 (2013) 669-680.

CHAPTER 5

**Development of a proof-of-concept
Thermomagnetic Motor**

5.1 INTRODUCTION

Activities in cities produce a large amount of heat approximately 300TWh per year within the EU[1] — but little of that heat is used properly today, resulting in high emissions and low energy efficiency. High-temperature industrial waste heat is typically used for industrial and residential heating, for instance redistributed in heat networks. By contrast, low- and medium-temperature waste heat below 100°C, accounting for over 63% of the total waste heat[2], cannot be utilised efficiently by the industry using conventional technologies like Organic Rankine cycle (ORC) or Kalina cycle, providing a market niche with a huge potential for innovations that can use this kind of waste heat. To address this niche, middle temperature (70°C - 100°C) to low temperature (30°C - 70°C) waste-heat-to-power (WHP) technology has been extensively studied. Together with the breakthrough in advanced materials, researchers successfully extended the low temperature limit of WHP devices.

There are conventionally two categories of such devices which differentiate with their conversion mechanism. A WHP device which converts thermal energy directly into electricity is called WHP generator. In this category, usually Thermoelectric (TE), pyroelectric (PE), or Magnetocaloric (MC) technology is applied. Thermoelectric (TE) generators are devices that convert thermal energy into electrical energy through the Seebeck effect. They are based on the principle that a temperature difference between a junction of two different conductive materials can generate an electrical potential. The absence of moving parts makes TE devices easy to install and reliable, suitable to be applied to almost any WHP application where media with different temperatures are present. With large scale assembly and large working temperature difference, the power output of TE system can reach the kilo watts range[3], but it is usually much lower(at the order of 0.5 – 1W per TE module[4-6]) for practical applications due to high costs and lower temperature differences. Besides, the efficiency of TE devices at middle temperature (~5%) to low temperature (<1%) is not so impressive[7].

Like TE devices Pyroelectric (PE) materials respond with a change of polarization on a change in temperature. However, instead of a temperature difference, the pyroelectric effect generates an electrical charge with a change in temperature or heat flux over time. PE materials are conventionally used as sensing component in sensors like infrared radiation detectors or thermographic cameras. Moreover, the spontaneous polarization and the dielectric permittivity can also benefit the application of WHP generation[8]. Thanks to the high sensitivity of PE materials, the PE device nowadays can easily convert heat from sources with rather low temperature, such as the body temperature of humans (~36°C). Also, PE devices can usually be very small. For example, Yu et al.[9] explored PE in a nanogenerator which serves as self-sustain power source for wearables. Potnuru

et al.[10] designed a PC-mouse powered by human heat. Surmenev et al.[11] proposed an anodic aluminium oxide (AAO) membrane based nanogenerator for biomedical applications. According to the latest analysis, the efficiency of PE devices can be as high as 15% in the middle to low temperature region, and possibly can be further improved by combining with other caloric technology (like pyro-, thermo- or magnetocaloric)[12]. The disadvantages of PE technology are, the power output is difficult to scale up, output can have stability issue when subjected to a fluctuating heat source, and a high impedance. Utilizing Magnetocaloric (MC) material, a thermomagnetic generator (TMG) device converts a temperature difference into electrical power via the magnetocaloric effect (MCE) and Faraday law[13]. By changing the temperature of an MC material, which exhibits a large change of magnetization around its Curie temperature (T_c), the magnetic flux flowing through the MC material will also be changed. With this time-varying magnetic flux, an electric voltage can be generated in a coil. This concept results in great flexibility of magnetic circuits and heat transfer mechanisms to optimize the performance of TMGs. Gueltig et al. developed a TMG with resonant self-actuation, which uses thin films of Heusler alloys that vibrate resonantly due to the alternating magnetization and heat transfer. This design is the first implementation of TMG at miniature length scales (mm to cm-range) [14]. Liu et al. proposed an innovative design that uses a magnetocaloric switch, which controls the magnetic circuit by changing the reluctance of the parallel paths. The electrical power density per degree of temperature difference of this device is by 2 to 3 orders of magnitude higher than those of other active TMGs, and also much higher than existing TE and PE devices [15]. Although TMGs are proven to have higher efficiency than thermoelectric generators at small temperature differences and have higher power density than pyroelectric generators, TMGs still face some challenges, such as the need for high-quality magnetic materials, reliable heat transfer systems, and effective magnetic shielding.

Another category of thermomagnetic device works with an indirect conversion method, which converts thermal energy first into other form of energy (mostly kinetic energy such as rotation, reciprocation, or swing), and then further converts into electricity with some additional device such as an electrical generator. Devices falling into this category are usually called thermomagnetic motor (TMM) or thermomagnetic actuator (TMA).

A TMM converts thermal energy into mechanical energy in the form of rotational motion. The motor typically consists of a rotor with a soft magnetic material and a stator containing permanent or electrically driven magnets. When a temperature gradient is applied across the rotor, it creates a magnetization gradient across the rotor in response to the magnetic field generated by the stator, causing it to rotate. This rotation can be used to generate electrical power or perform mechanical work.[16] A TMA is a device that converts thermal energy into mechanical energy in the form of linear motion. The

actuator typically consists of a soft magnetic core surrounded by a solenoid coil or a ring of permanent magnet. When a temperature gradient is applied across the core, it moves in a linear motion in response to the changing magnetization state. This linear motion is usually used for precision control or triggering mechanism[17, 18]. Both TMA and TMM can be used to convert low-temperature waste heat in the range from 35°C up to 100 °C from a wide range of heat sources into electricity.

Although TMMs have some disadvantages compared to TMAs, such as lower efficiency, bulky design, and limited precision[12], TMMs still represent the most promising approach for unlocking ultra-low-temperature heat as energy source for future zero-emission electricity supply. TMMs are among the best available alternatives for environmentally friendly thermal energy harvesting system [24]. because compared to TMA, TMM have the following advantages:

Wider material compatibility: TMMs usually have a relatively big and mechanically robust working unit – the rotor, which has the capacity to be equipped with working material with any shape, microstructure and working temperature range. On the other hand, TMAs have a small and light weight structure. Therefore, being more demanding on the working material to fill its precious internal space.

Higher power output: TMMs are designed to produce rotational motion, which is continuous and can generate higher power output due to the inertia when compared to the linear (reciprocating) motion produced by TMAs.

Greater versatility: TMMs, similar to typical motor, can be designed to produce torque in any direction via transmission structure; while TMAs are typically limited to producing linear motion along a specific axis.

Potential for use in larger systems: TMMs can be designed to produce sufficient power to drive larger systems, such as vehicles or power plants, while TMAs are typically used in smaller systems, such as microelectromechanical systems (MEMS) or sensors.

Continuous power output: this is the major advantage compared to most renewable energy technologies which often have an intermittent power output or is limited by certain geographic factor (such as hydropower). With this technology, it is possible to produce electricity with low cost by utilizing freely available heat from industrial processes that would otherwise be discarded. This may significantly increase energy efficiency of power plants and industrial processes resulting in lower costs of production. The compact and modular design allows a site independent and decentralized generation of electricity world-wide. Due to an emission-free operation there is no negative impact

on the environment.

The earliest development of the TMM is when Thomas Alva Edison and Nikola Tesla patented the first designs with the “Pyromagnetic Generator” [19] and the “Thermo-Magnetic Motor” [20], but none of them have built the device due to a lack of suitable material. After that, in 1972 Murakami and Nemoto[16] developed the first TMM prototype. The development had paused quite a while since there is no “temperature sensitive magnetic material” that can fill the gap. Then in 1997, with the discovery of room temperature Giant Magnetocaloric Effect (GMCE)[21], the development on TMM again started to move forward. From then on, several prototypes with various designs have been presented[22-24]. At Swiss Blue Energy AG, with 1 kW power output, the TMM prototype has almost reached industrial scale[25]. In 2022, Hey et al. [26] developed a TMM prototype with 88 W output power and 2.1% energy conversion efficiency, which marks the highest energy efficiency up-to-date.

While we see the design of the TMM prototype is improving over time, the working principle has barely changed. Just as the development in magnetocaloric heat pumps, active magnetic regenerator with multilayer magnetocaloric materials replacing the gadolinium-based regenerator and greatly expanding the performance of the device, for TMM to develop further, the working material selection and the working principle has to be innovated.

In this work, we developed a proof-of-concept TMM prototype Thermomagnetic Motor MK0 (TMM0), which serves as a demonstration setup for showcasing the WHP technology as well as a material testing platform for the quality control of the 3D printed MCMs. After that, we propose a work cycle with a magnetocaloric heat exchanger geometry selection to improve the system efficiency of the TMM. An explicit numerical analysis is used to show the advantage of the proposed method.

5.2 DESIGN AND FEATURES

The Thermomagnetic Motor MK0 (TMM0) is an experimental prototype that utilizes the soft magnetic property by continuously magnetizing and demagnetizing a magnetocaloric material (MCM) wheel to create a rotating movement. The magnetic force between the magnet and the MCM can be activated and deactivated by changing the MCM’s temperature with the flow of cold and hot water. A rotary wheel with 24 units of Magnetocaloric heat exchanger (MCHE) mounted along its outer edge. The wheel has a part inserted into the air gap of the magnet so that the MCHEs near the inserted section are in the magnetic field. While a MCHE on one side of the magnet is in the magnetizing

state and a MCHC on the other side is in the demagnetizing state, a net magnetic force is applied, the wheel will start to rotate and all MCHCs will enter and exit the magnetic field successively. By continuously applying a constant flow of cold and hot water to the MCHC at the two sides of the magnet, the rotating movement of the wheel will be stabilized. The major components of the TMM are: the heat exchanger units with MCM, the permanent magnet assembly as magnetic field source, the rotary wheel to convert the magnetic force into rotational torque and movement, and the hydraulic system for heating and cooling the MCHCs.

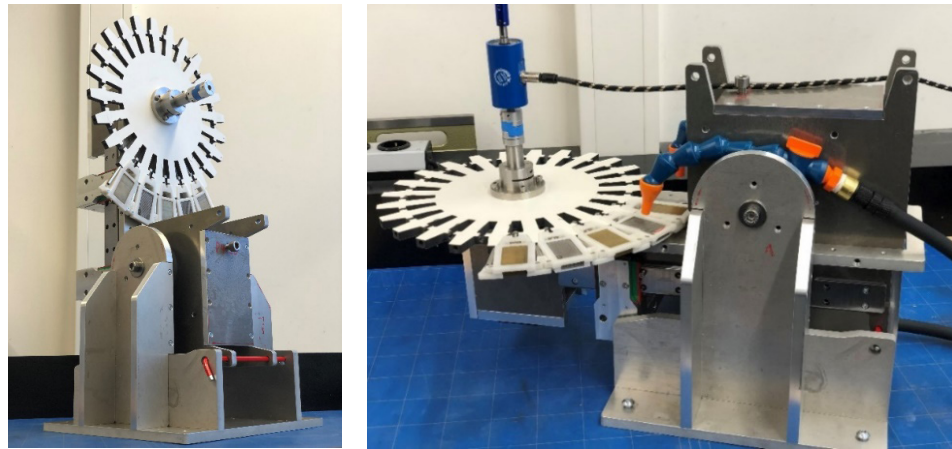


Figure 5.1: the demo mode (Left) and the measurement mode (right) of the TMM0

As the purpose of TMM0 are both a demonstrator and a material test platform. We equipped TMM0 with two working modes: the demo mode and measurement mode, which are shown in Fig. 5.1.

5.2.1 the 3D mesh heat exchanger

Magneto produced several kilograms of magnetocaloric material (MCM) by atomization using chemical compositions suitable for waste heat to power conversion in a thermomagnetic motor. Atomization is a production method suitable for mass production of powders of magnetocaloric materials.

The atomized spherical particles were mixed with an organic binder to make a paste. The paste was 3D printed to create heat exchanger units in form of 3D mesh structures (Fig. 5.2). After printing, the 3D mesh structure was put into a furnace for heat treatment to form the magnetocaloric phase and activate the magnetic properties. The external dimension of the blocks after heat treatment is around 50x30x10 mm (Length x width x

height), the fibre diameter is about 500 μm and porosity $\sim 50\%$ (Fig. 5.2, middle).

The 3D mesh structure is then mounted in the 3D printed sample holder and then becomes a heat exchanger. The glycolized polyester (PETG) sample holder is rigid enough to handle the out of plane magnetic force on the MCM. Also, thanks to the low conductivity no eddy current will be generated from the AC magnetic field. Besides, the hollow design of the sample holder can ensure the hot/cold water stream can exchange heat with the MCM efficiently.

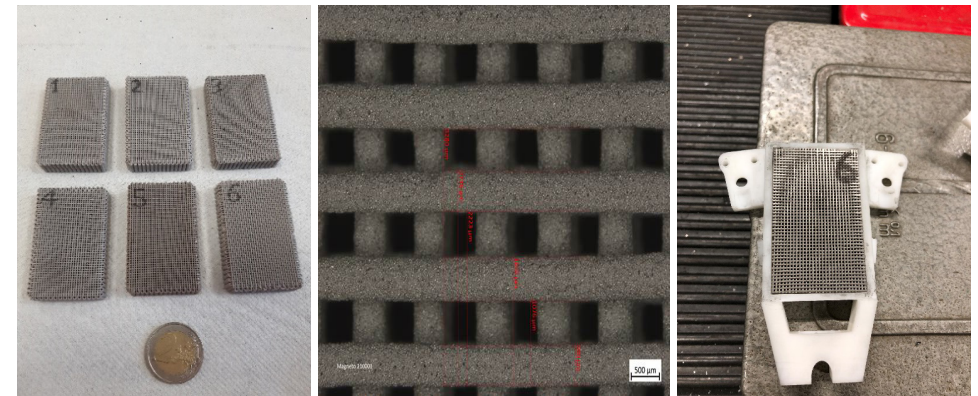


Figure 5.2: (Left) Pictures of 3D printed 3D mesh structures. (middle) Optical microscopy image of the 3D mesh structure. (Right) 3D mesh structure mounted in sample holder of the thermomagnetic motor

The magnetization as a function of temperature ($M(T)$) of the MCM 3D meshes are measured by a superconducting quantum interference device (SQUID). $M(T)$ is a key property to evaluate the performance of MCMs. The MCM has a magnetic phase transition marked by the Curie temperature (T_c). At T_c the MCM changes from a magnetic state (ferromagnetic, below T_c) with large magnetization to a practically non-magnetic state (paramagnetic, above T_c) state with low magnetization. The magnetization change $\Delta M = M(T_{\text{ferromagnetic}}) - M(T_{\text{paramagnetic}})$ across T_c is directly linked to the power output for waste heat to power conversion in a thermomagnetic motor (TMM). Therefore, a large ΔM between hot and cold source temperatures is preferable.

In the 3D meshes 210001 and 210003 (Fig. 5.3) we observe a large magnetization change with large thermal hysteresis of $\sim 18\text{K}$. The original powder without binder has been heat treated in quartz ampoules and has a $T_c = 269.2\text{ K}$. After processing with 3D printing the T_c increases and shifts to a higher temperature of 292.8K .

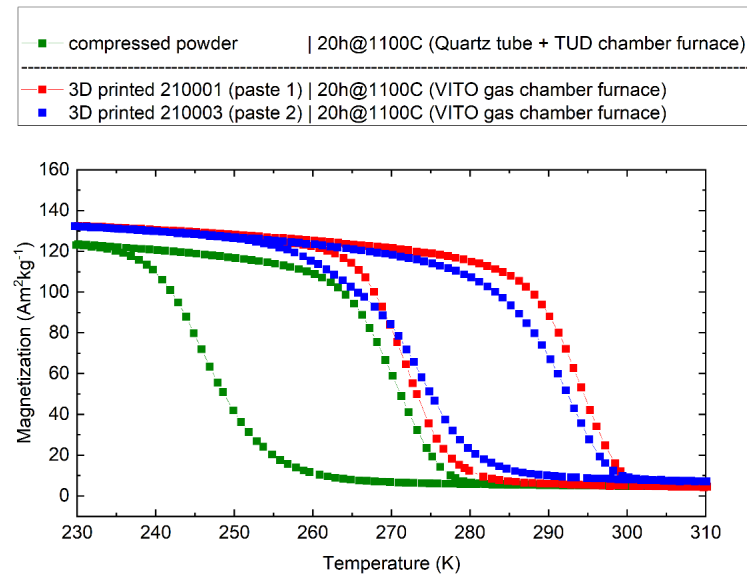


Figure 5.3: Temperature dependent magnetization of 3D mesh structures.

In the next batch, the original powder (21007) without organic binder shows $T_c = 284.2$ K (11°C). When this powder was processed into 3D printed meshes (21007), the T_c decreased by 6.0°C to $T_c = 278.2$ K (5°C) (see Fig. 5.3 and 5.4). This is in contrast to the first batch (210001, 210003), where the T_c increased after processing the powder with 3D printing.

3D printing has significant impact on the magnetocaloric properties of the MCM. The different chemical compositions have impact on the behavior of the T_c after 3D printing and increase in batch 1 (210001, 210003), whereas it decreases in batch 2 (21007).

5.2.2 Rotary wheel

The rotary wheel is the key component which supports the MCM and converts the magnetic force into rotational torque. The body material for the wheel is High Pressure Laminate (HPL), which is a non-magnetic laminate material both rigid enough to support the heat exchangers against magnetic force and easy to shape. The wheel is mounted between two sets of ball bearings, which lock the wheel right in the middle of the air gap of the magnetic field source, as shown in Fig. 5.5.

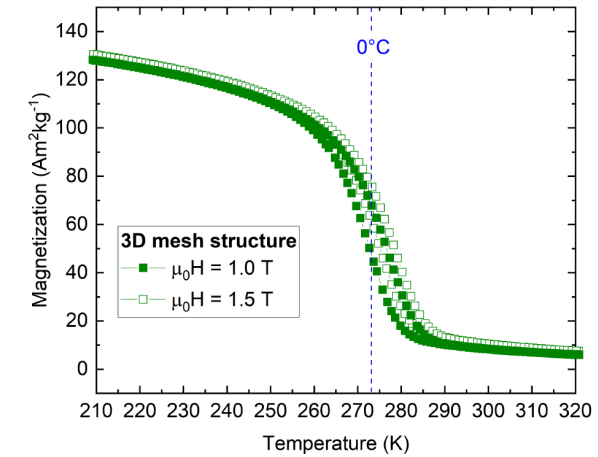


Figure 5.4: Temperature dependent magnetization of the 3D mesh structure.

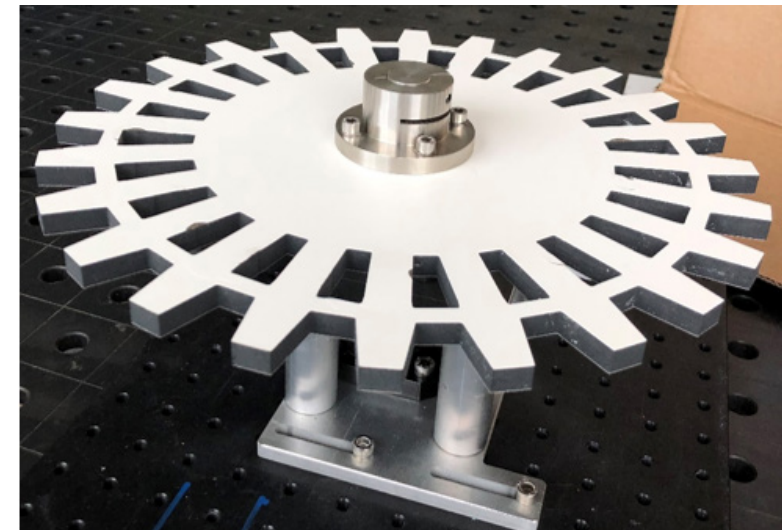


Figure 5.5: the rotary wheel

5.2.3 Permanent magnetic field source

The permanent magnetic field source is the origin of the magnetic force in this system. A "n" shape iron yoke combined with a set of NdFeB permanent magnet blocks forming a Halbach array, which generates a 1.5 T magnetic field in the gap. A photo of the device is shown in Fig. 5.6 (left). The Magnetic field is well contained near the air gap of the magnet. Therefore, no stray field will endanger anybody even people with a pacemaker. The magnetic field distribution is shown in Fig. 5.6 (right). The maximum field density

generated by the field source is right in the middle of the air gap, which is 1.57 T. From the central to the edge of the air gap, the field density decreases gradually. However, in a tiny zone from the edge to the outside the airgap, the gradient of field density changes dramatically from 1.34 T to ~0.43 T, which means that the highest magnetic force can be induced in this region. Once the distance from the edge of the air gap exceeds 5 cm, the field density decreases under 0.026 T, which produces negligible forces.

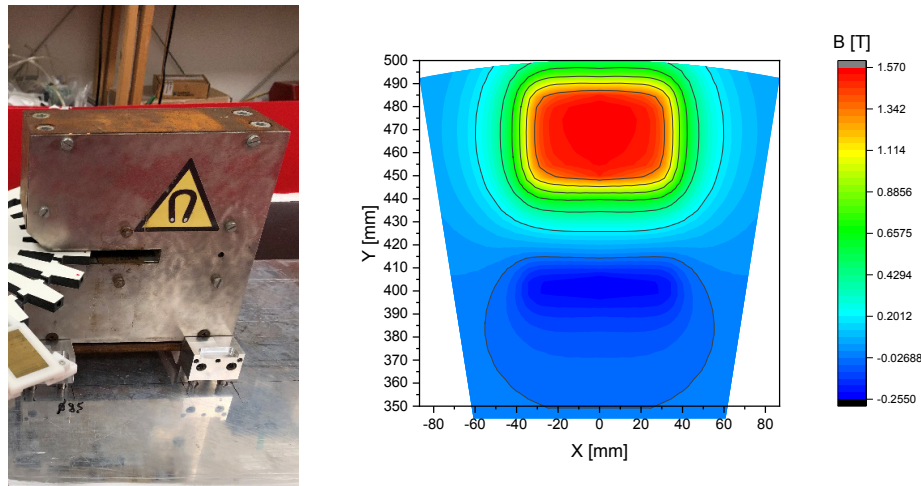


Figure 5.6: the magnetic field source (Left) and its magnetic field profile (right)

5.2.4 The hydraulic system

The core components of the hydraulic system are, two sets of thermostatic baths, diaphragm pumps, Hall effect liquid flowmeters and water reservoirs (as bubble trap), see Fig. 5.7. With the thermostatic bath, we can accurately control the temperature for magnetizing and demagnetizing the MCMs, and if necessary, simulate the time-varying temperature in the city environment. The DC diaphragm pump is controlled by a close-loop PWM method, which results in an adjustable flow rate of 0.1 – 6.5 Lpm. The Hall effect flow meter generates zero resistance to the water flow, while it has a quantitative accuracy of 1%. The bubble trap is used to eliminate the air bubble formed in the water stream due to pressure changes.

To enable independent control of the cold and warm side, we have a duplicate hydraulic system for the cold and hot water cycle, respectively. The water with desired temperature and flow rate will be injected to the MCM block by flexible nozzles, and flow back to the hydraulic system through separate sinks.

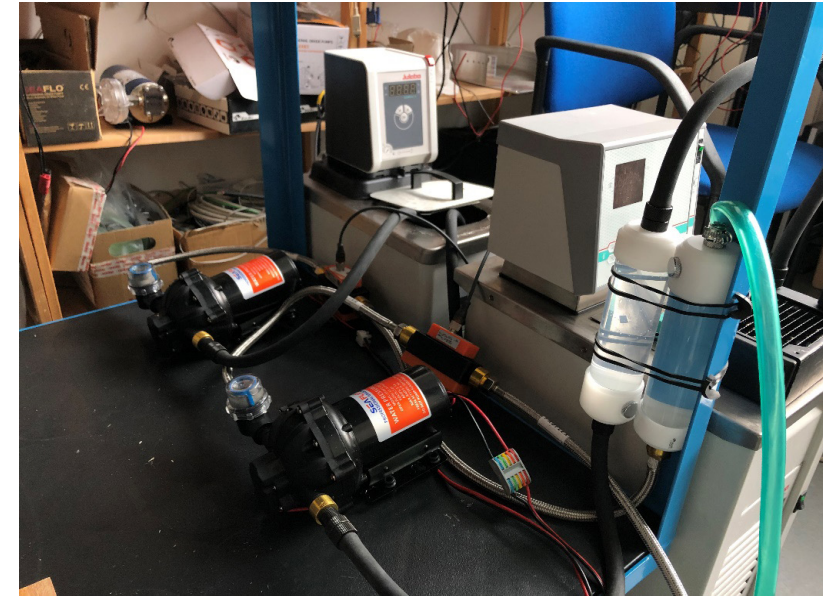


Figure 5.7: the hydraulic system includes pumps reservoirs and thermostatic baths

5.3 EXPERIMENT AND RESULT

The performance of the thermomagnetic motor is determined from the torque of the system, which is caused by the difference of magnetization between heated and cooled MCMs. In the measurement mode of TMM0, there are three major sensors for the performance measurement, i.e., the NCTE 2300 non-contact torque & speed transmitter, the PT-100 temperature sensor, and the Kobold MIK -5NA20-A-F300 hall effect liquid flowmeter. As for output, we get the angular speed (ω), axial rotary torque (Γ), temperature of cold and hot water stream (T_c and T_h), and their volumetric flow rates (\dot{V}).

The performance metric of the TMM can be evaluated by measuring the net axial torque generated by the MCM under certain temperature differences, and the power generated by the rotary movement of the wheel with some working load as torque. The power generation of the TMM can be calculated with $\overline{P}_{motor} = \omega \Gamma$.

Based on the MCM properties we learned, the performance analysis procedure for TMM0 is as followed:

Three pairs of hot and cold source temperature are selected in order to utilize the magnetocaloric property of the MCM 210003, and try to mimic the temperature profile

from the user cases that we learned from our previous investigation (Climate-KIC: Local, Magnetocaloric Power Conversion Opportunities for Cities):

- Hot source temperature at 303.15 K (30°C, waste water from industry like chemistry, data center), $\Delta T = 50$ K;
- Hot source temperature at 293.15 K (20°C, waste water from household), $\Delta T = 40$ K;
- Hot source temperature at 283.15 K (10°C, natural canal/lake water), $\Delta T = 30$ K.

Note that the temperature of cold source stays at 253.15 K (-20°C) to be able to cool the MCMs' down to the ferromagnetic state. The flow rates for both the hot and cold streams are keeping at 3.2 Lpm. Due to the limited number of MCM 3D meshes, we can only populate the rotary wheel with 3 heat exchangers. Therefore, the recorded angular position range is set to 16° to show the torque profile pattern which has a rotary symmetry of ~15.7°. After applying the hot and cold-water stream on the MCMs, a torque load is applied on the NCTE 2300 to stop the rotary wheel, and the torque value indicated by the NCTE 2300 is recorded.

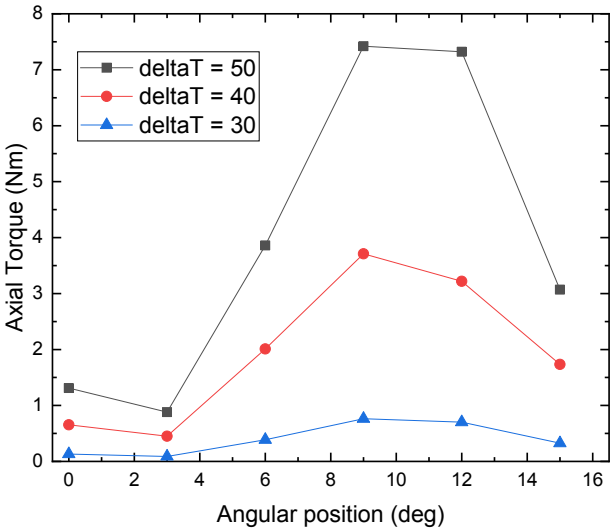


Figure 5.8: Performance of TMM0 derived from torque of the systems for different temperature profiles.

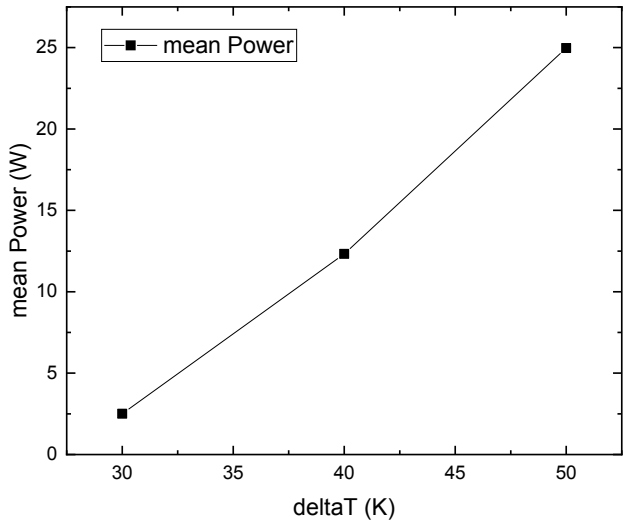


Figure 5.9: the mean power output of TMM0 for different temperature profiles.

We can see from Fig. 5.8 and Fig. 5.9, although the magnetocaloric property of the MCM 210003 is not ideal, axial torques that are large enough to rotate the wheel can still be generated. However, the axial torque decreased faster with a descending temperature profile. This is in line with the fact that the smaller temperature span will depress the efficiency of the TMM system. Note that, even for the highest temperature profile, the mean power generation from the TMM0 is only around 25W, which is lower than the energy consumption of the pumps (~50W). Therefore, at this moment, the TMM0 cannot generate any net power by harvesting the heat from the water streams.

5.4 IMPROVE THE PERFORMANCE OF TMM WITH MNFEPSIV

5.4.1 Working cycle design

As mentioned in 5.1, although the TMM has already become a “nostalgic classic” application, the attempts of innovation are quite limited. Most improvements focused on either the MCM properties, the magnetic field source, or the heat transfer fluid flow. Besides, in many studies the MCE is considered as a negligible or even negative property as its contribution to the temperature change is too small and has reverse effect compared to the simple heat transfer from HTF[26, 27]. Most of the current

TMM prototypes are gadolinium based due to availability and its decent mechanical and thermodynamic properties. However, given the broad magnetocaloric phase transition and the fixed T_c , Gd may not be a suitable working material for a TMM under various conditions[28]. To explore the possible advantage that can be brought by a tuneable first order material system like MnFePSiV and the impact of the geometry of the MCM we performed a numerical analysis as follows:

Consider a working cycle of the TMM as shown in Fig. 5.10: Assume the magnetocaloric heat exchanger on the wheel of the TMM starts from a low field B_0 at initial temperature T_1 . During the magnetization process in stage ①, the MCM in the heat exchanger is exposed to an elevated field B_1 , the temperature of the MCM rises to T_2 due to the adiabatic heating ΔT_{ad} caused by the MCE effect; The Magnetization of the MCM first reaches M_0 and then decreases to M_1 due to the elevated temperature. Then, during the heat transfer process in stage ②, by applying flow of hot HTF, the MCM heats up a ΔT_{tran} to T_4 , which further reduce the magnetization to M_2 , suppress the magnetic force and let the MCM leave the Magnet. The magnetization difference between the MCM entering the high field region and the MCM exiting the high field region is ΔM . Afterwards, during the demagnetization process in stage ③, the heat exchanger moves from high field region B_1 back to low field region B_0 while the temperature of the MCM in the heat exchange decreases to T_3 due to the MCE, the magnetization is greatly suppressed due the low field B_0 ; Last but not least, during the cooling process in stage ④, the temperature of the MCM is cooled down to T_1 , again. The heat exchange rotates back to its initial position with the wheel, ready to enter the high field region.

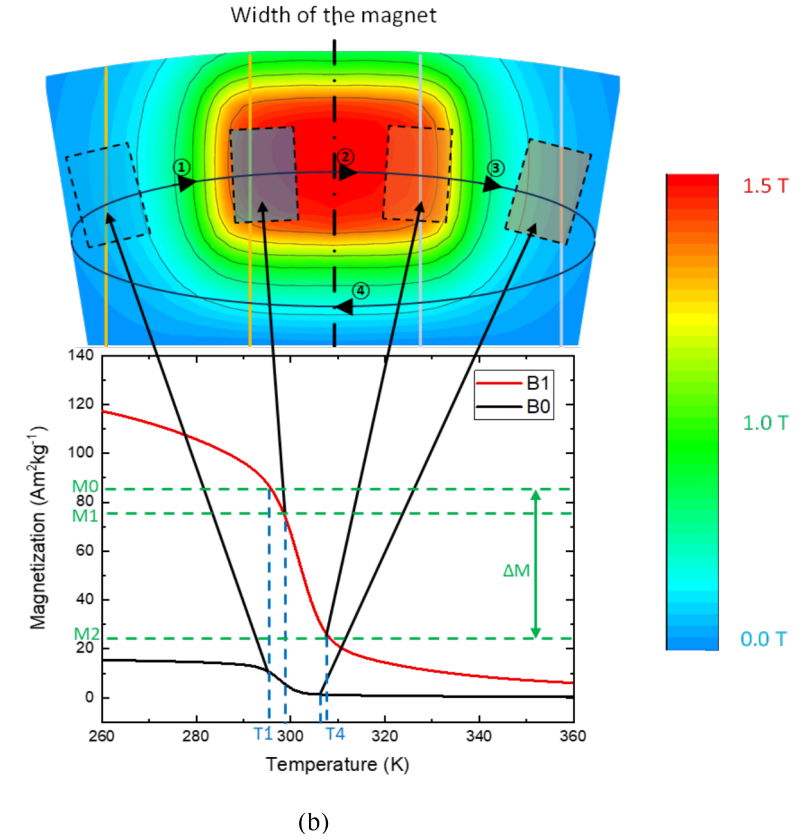
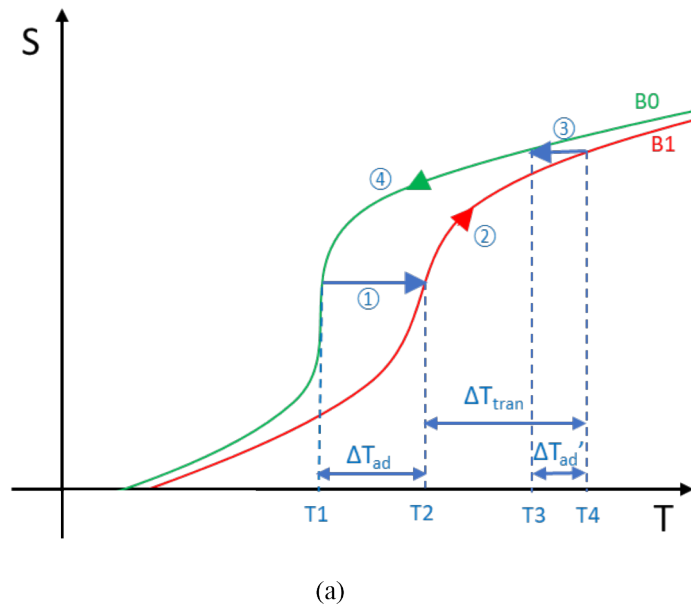


Figure 5.10: the operation cycle for the TMM numerical analysis: (a) cycle indicated in an entropy vs. temperature diagram; (b) cycle indicate in a magnetization vs. temperature diagram

5.4.2 Performance analysis with a TMM model

To explore the possibility to improve the performance of the TMM, we built a numerical model of a TMM based on explicit method. With this model, we will demonstrate the influence of various control parameters like magnetocaloric effect and flow rate, configuration parameters like heat source temperature, feature size, and porosity.

In this numerical model, we choose gadolinium as the benchmark of second order magnetic phase transition (SOMT) material. Then, we select a recipe from MnFePSiV series, which has a typical first order magnetic phase transition (FOMT). For a fair comparison, we selected a composition of MnFePSiV with its T_c very close to that of Gd ($T_{c_Gd} = 288.9$ K, $T_{c_MnFePSiV} = 297.9$ K). The magnetic and thermodynamic properties of both materials are shown in Fig. 5.11

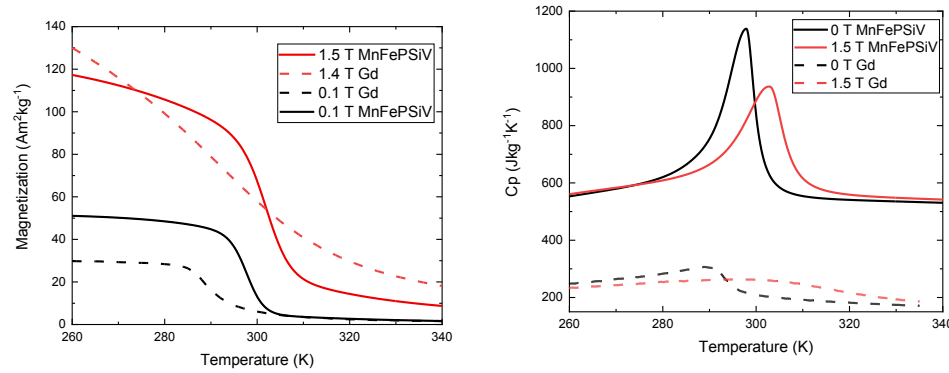


Figure 5.11: the material property used in this analysis: (a) cycle indicated in an entropy vs. temperature diagram; (b) cycle indicate in a magnetization vs. temperature diagram

Table 5.1 Main system parameters

Parameter	Value
Maximum applied field B	1.5 T
Working frequency f	2 Hz
Heat exchange duration t	10 ms
Heat exchanger dimension (LxWxH)	60x30x10 mm
Density of Gd ρ_{Gd}	$7.90 \times 10^3 \text{ kg/m}^3$
Density of MnFePSiV ρ_{Mn}	$6.50 \times 10^3 \text{ kg/m}^3$
Gd thermal conductivity κ_{Gd}	$11 \text{ Wm}^{-1}\text{K}^{-1}$
MnFePSiV thermal conductivity κ_{Mn}	$6.7 \text{ Wm}^{-1}\text{K}^{-1}$
Permeability of free space μ_0	$1.26 \times 10^{-6} \text{ NA}^{-2}$
Heat transfer fluid (HTF)	Aqueous solution with 40% v/v ethylene glycol

The system parameters for the simulation are listed in table 5.1. As for the geometry of the heat exchange, three popular geometries are studied, namely: packed screen bed (PSB), packed sphere bed (PB) and parallel plate matrix (PP). A PSB is a type of packed bed that consists of a series of screens made by fibers or strips that are arranged in parallel and staggered. The screens create channels for the fluid flow and enhance the heat transfer between the fluid and the solid material i.e. the MCM. A spherical packed bed is a type of packed bed that consists of spherical MCM particles that are randomly packed in a container. The spherical particles provide a large surface area for the fluid-solid contact but introduce large pressure drop across the bed. A parallel plate heat exchanger geometry is a type of heat exchanger that consists of thin MCM plates that are stacked in parallel and separated by a small gap. The plates create channels for the hot and cold fluids to flow in alternate directions and exchange heat through conduction.

Various fluid dynamic and heat transfer correlation functions exist for these typical geometries, we made a selection based on their accuracy and wide applicability. Basically, heat transfer coefficient h of all geometries can be calculated as:

$$h = Nu k_f / D_g \quad (5-1)$$

where Nu is the Nusselt number of given geometry, k_f is the thermal conductivity of fluid, and D_g is the geometry feature size (diameter of the sphere, thickness of the plate or fiber, etc.).

For packed screen bed (PSB), a flow friction correlation was developed by Armour and Cannon[29] that can be applied to the flow through most types of these woven screens with varying porosities.

$$\frac{dP_{PSB}}{dx} = \left[\frac{8.61}{\left(\frac{\rho_f v_s}{a_s^2 \mu_f D_g} \right)} + 0.52 \right] \left[\frac{\rho_f (v_s/\varepsilon)^2}{D_g} \right] \quad (5-2)$$

On the other hand, Park et al.[30] presented a heat transfer correlation based on experiments conducted on this geometry, which demonstrated the highest level of precision when compared to others.

$$Nu_{PSB} = 1.315 \left(\frac{\mu_f c_{pf}}{k_f} \right)^{1/3} \left(\frac{\rho_f (v_s/\varepsilon) D_g}{\mu_f} \right)^{0.35} \left(\frac{1-\varepsilon}{\varepsilon} \right)^{0.2} \quad (5-3)$$

For packed bed (PB), the Ergun equation[31] is used to describe the friction factor,

$$\frac{dP_{PB}}{dx} = 2\alpha \frac{(1-\varepsilon)^2 \mu_f v_s S_v^2}{\varepsilon^3} + \frac{\beta (1-\varepsilon) \rho_f v_s S_v}{\varepsilon^3} \quad (5-4)$$

Where $\alpha = \left(\frac{\pi}{2} \right)^2$, $\beta = 2.4$, and $S_v = 6/D_g$.

and the correlation presented by Wakao et al.[32] is used to calculate the Nusselt number for its higher accuracy at low porosity and higher specific surface area.

$$Nu_{PB} = 2 + 1.1 \left(\frac{\rho_f v_s D_g}{\mu_f} \right)^{0.6} \left(\frac{\mu_f c_{pf}}{k_f} \right)^{1/3} \quad (5-5)$$

For the parallel plate geometry Nickolay and Martin's[33] correlation for overall Nusselt number produced the most accurate estimations.

$$Nu_{PP} = \left[7.541^n + (1.84 Gz^{1/3})^n \right]^{1/n} \quad (5-6)$$

where $Gz = \frac{2v_s A_c \rho_f c_{pf} D_g}{k_f W_n L}$ and $n = 3.592$.

Fanning developed the friction factor for laminar flow through parallel-plates heat exchangers, which is presented as $f_f = 24/Re$ [34]. Therefore, the correlation function for pressure drop calculation can be written as:

$$\frac{dP_{PP}}{dx} = 4 \left[24 / \left(\frac{\rho_f (v_s/\varepsilon) D_g}{\mu_f} \right) \right] \left[\frac{\rho_f (v_s/\varepsilon)^2}{2D_g} \right] \quad (5-7)$$

This is further supported by similar expressions found in other related works.

In this simulation, the MCMs' time-dependent temperature response was investigated using a lumped parameter analysis approach. This particular approach assumes that the object has a uniform internal temperature, which is a reasonable assumption if the Biot number for the given geometric shape of the material is small enough. The Biot number is calculated with:

$$Bi = \frac{h}{k} L \quad (5-8)$$

Where, h , k and L are the heat transfer coefficient, thermal conductivity and the length along the flow channel, respectively.

The adiabatic temperature change of the MCM is calculated with:

$$\Delta T_{ad} = - \int_{B_0}^{B_1} \frac{T}{c_p(B,T)} \left(\frac{\partial M(B,T)}{\partial T} \right) dB \quad (5-9)$$

Where B_0 , B_1 , T , c_p are initial applied field density, final applied field density, temperature of MCM, specific heat capacity of the MCM. Note here, both the temperature change of magnetization process (heating) and that of demagnetization process (cooling) can be calculated with the same equation, the only difference is the starting temperature.

The temperature change caused by the heat transfer from the HTF is calculated with:

$$\ln \frac{T_{tran}(t) - T_{HTF}}{T_i - T_{HTF}} = - \frac{hA_s}{\rho V c_p(B,T)} t \quad (5-10)$$

Where $T_{tran}(t)$ is the temperature of the MCM after applying HTF flow for a duration t . The final change of the temperature in the MCM is:

$$\Delta T_{tot} = \Delta T_{ad,h} + \Delta T_{tran}(t) + \Delta T_{ad,c} \quad (5-11)$$

Where $\Delta T_{ad,h}$ and $\Delta T_{ad,c}$ is the adiabatic temperature change for heating and cooling respectively.

The resulting magnetization change is:

$$\Delta M = |M(B, T_{ini}) - M(B, T_{ini} + \Delta T_{tot})| \quad (5-12)$$

Note that this is an iso-field demagnetization process, therefore B is uniform.

The magnetization change percentage is a direct parameter which reflects the net magnetic force induced by the magnetization change. It is calculated as:

$$R_{mag} = \frac{\Delta M}{M(H, T_{ini})} \times 100\% = \left| \frac{M(H, T_{ini} + \Delta T_{tot}) - M(H, T_{ini})}{M(H, T_{ini})} \right| \times 100\% \quad (5-13)$$

When the TMM rotates due to the magnetic torque induced by the temperature difference, the input of the system is the heat inflow and the pumping power to overcome the pressure drop across the heat exchanger:

$$\eta_{sys} = \frac{W_{mag}}{Q_{in} + W_{pump}} \quad (5-14)$$

Where,

$$W_{mag} = \mu_0 \oint H dM \quad (5-15)$$

$$Q_{in} = \rho V \int_{T_c}^{T_h} c_p(T, B) dT \quad (5-16)$$

and the necessary pumping power to push the HTF through the shaped MCM can be expressed as

$$W_{pump} = P A_c L \quad (5-17)$$

Where P , A_c and L are pressure drop, cross section area and the length of the flow channel, respectively.

In order to have a fair comparison between the efficiency generated by different geometries, we compared them with ideal Carnot efficiency over the maximum temperature span in the system, which in our case is:

$$COP_{h,Carnot} = \frac{T_H - T_c}{T_H} = \frac{T_{HTF} - T_{ini}}{T_{HTF}} \quad (5-18)$$

Then the second-law efficiency can be written as:

$$\eta_{2nd} = \frac{\eta_{sys}}{COP_{h,Carnot}} \quad (5-19)$$

The last performance parameter we considered here is the hot HTF consumption for generating 1 kWh electricity. In each cycle, the hot HTF flow through the MCM is calculated as the sum of the HTF remains in the pores of MCM and the amount of HTF flow through of the MCM:

$$V_{cycle_HTF} = V_{MCM}\varepsilon + \dot{V}t \quad (5-20)$$

For simplifying the case of the electrical power generation, we assume the magnetic work generated by the MCM is fully converted into electricity (in the real case the mechanical efficiency is around 95%) and there is only one magnetic field source in the system. therefore, the HTF consumption for generate 1 kWh electricity can be calculated as:

$$V_{consump} = \frac{3600 \times 1000}{W_{mag}} V_{cycle_HTF} \quad (5-21)$$

By implementing all the equations and correlation functions into the model, we can perform simulations case by case with single sets of parameters or in groups with bundled parameters. In the next section of this chapter, we list two batches of simulations. The 1st batch focus on the contribution of the MCE and the 2nd batch focuses on the influence of the configuration parameters. We preset here the Magnetization change percentage, the second-law efficiency and the hot HTF consumption as result for both simulation batches.

5.4.3 Modelling result

In the first batch of simulation, beside the main analysis parameters, we also keep the heat source temperature, the feature size, and the porosity the same, with $T_h = 333$ K, $G_f = 0.6 \times 10^{-3}$ m, $\varepsilon = 30\%$, respectively. By varying the flow rate from low $\dot{V} = 1.6 \times 10^{-7}$ m³/s, middle $\dot{V} = 9.26 \times 10^{-6}$ m³/s, $\dot{V} = 1.75 \times 10^{-5}$ m³/s to high $\dot{V} = 2.17 \times 10^{-5}$ m³/s, we can observe how much the MCE contributes to the overall performance under different initial temperature and heat-flow conditions.

For better comparison, we list the results with MCE effect in the columns on the left and the results without MCE effect in the columns on the right. In the HTF consumption plot y axis is with logarithmic scale in order to present both the extreme value around the Cuire temperature of the MCMs and the mild value in the rest of the temperature range well.

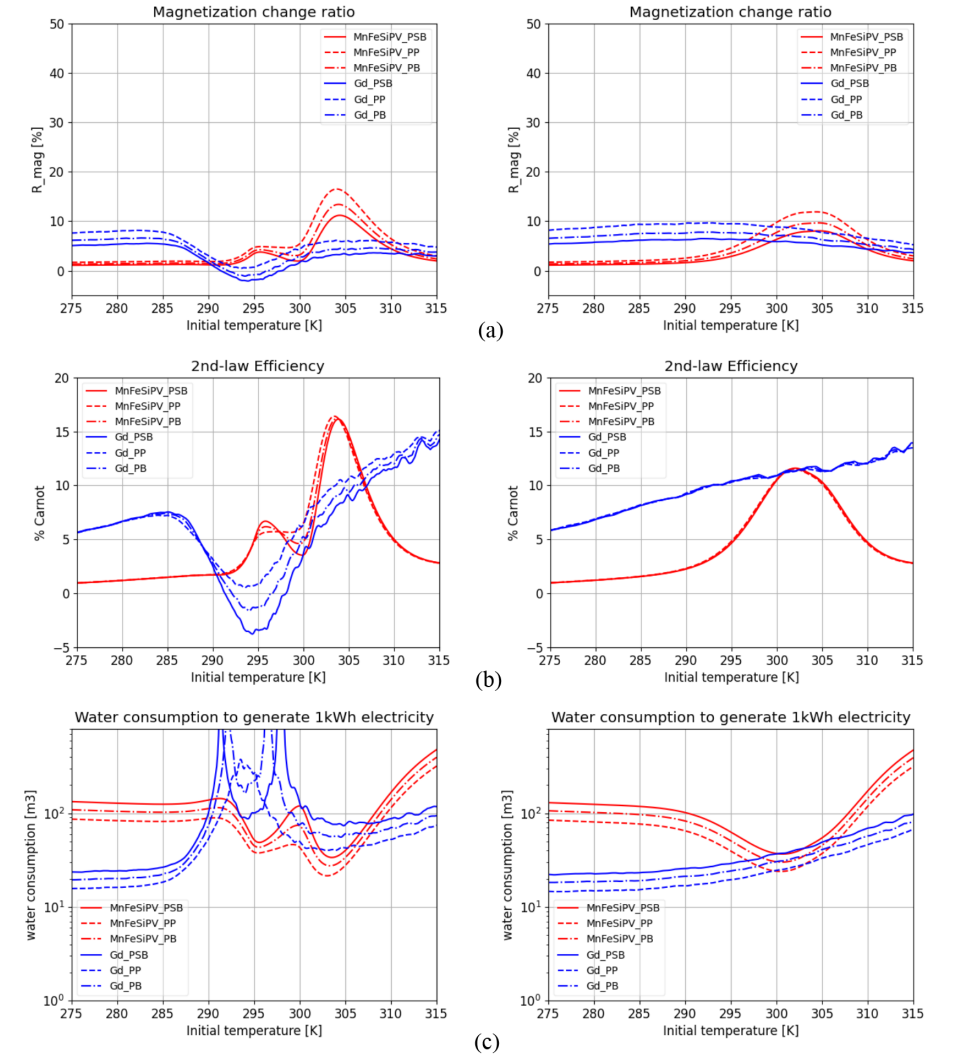


Figure 5.12: Performance result versus initial temperature of the MCM with the analysis variables set $G_f = 0.6 \times 10^{-3}$ m, $\varepsilon = 30\%$, $T_h = 333$ K, $\dot{V} = 1.6 \times 10^{-7}$ m³/s, plots in left column are the results considering MCE while right column are the results ruling out MCE

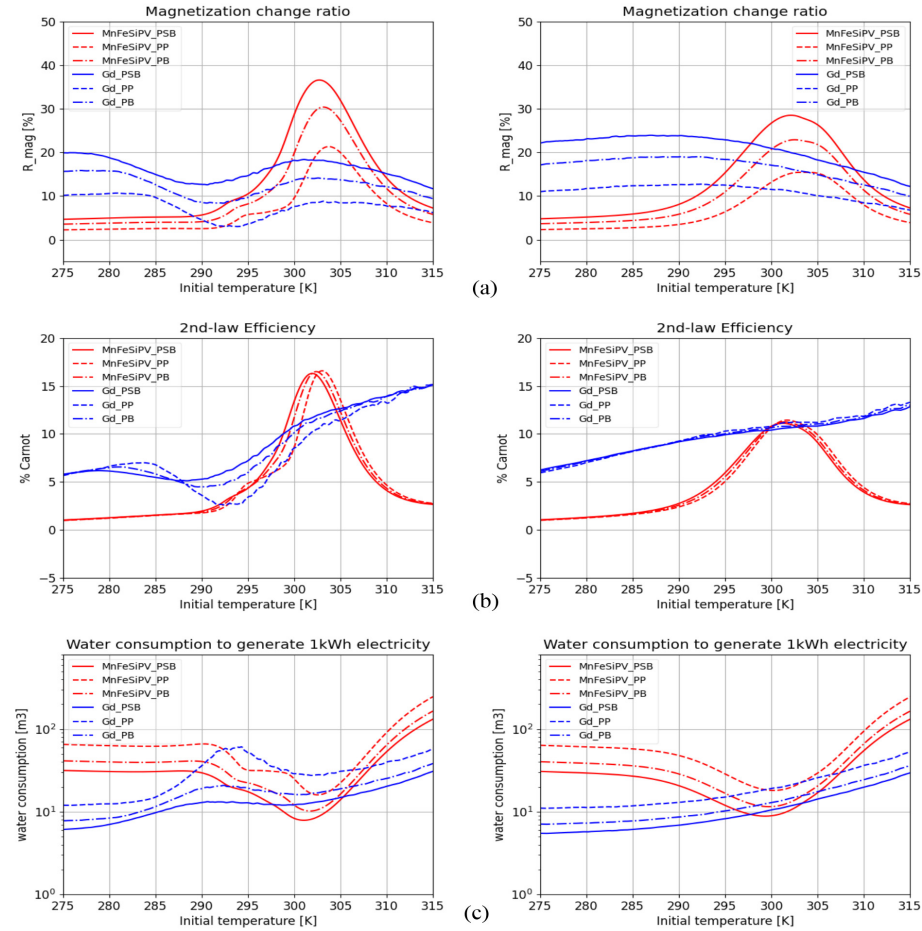


Figure 5.13: Performance result versus initial temperature of the MCM with the analysis variables set $G_f = 0.6 \times 10^{-3} \text{ m}$, $\varepsilon = 30\%$, $T_h = 333 \text{ K}$, $\dot{V} = 9.26 \times 10^{-6} \text{ m}^3/\text{s}$, plots in left column are the results considering MCE while right column are the results ruling out MCE

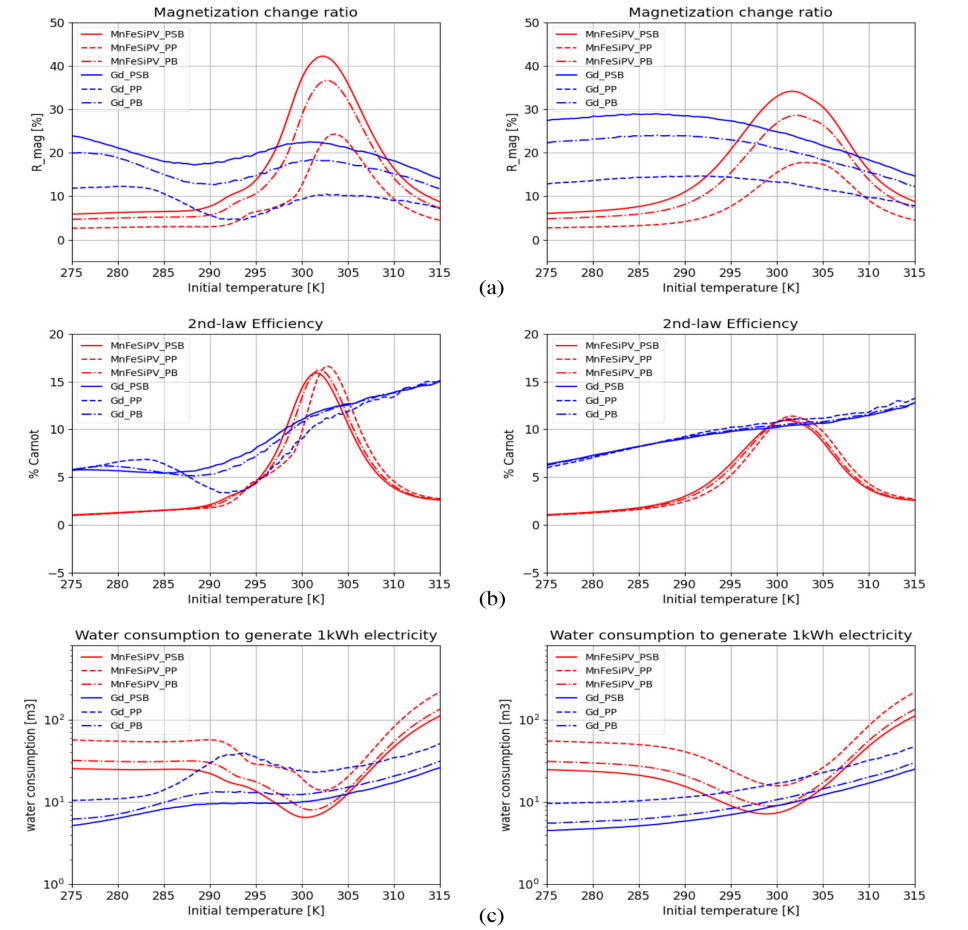


Figure 5.14: Performance result versus initial temperature of the MCM with the analysis variables set $G_f = 0.6 \times 10^{-3} \text{ m}$, $\varepsilon = 30\%$, $T_h = 333 \text{ K}$, $\dot{V} = 1.75 \times 10^{-5} \text{ m}^3/\text{s}$, plots in left column are the results considering MCE while right column are the results ruling out MCE

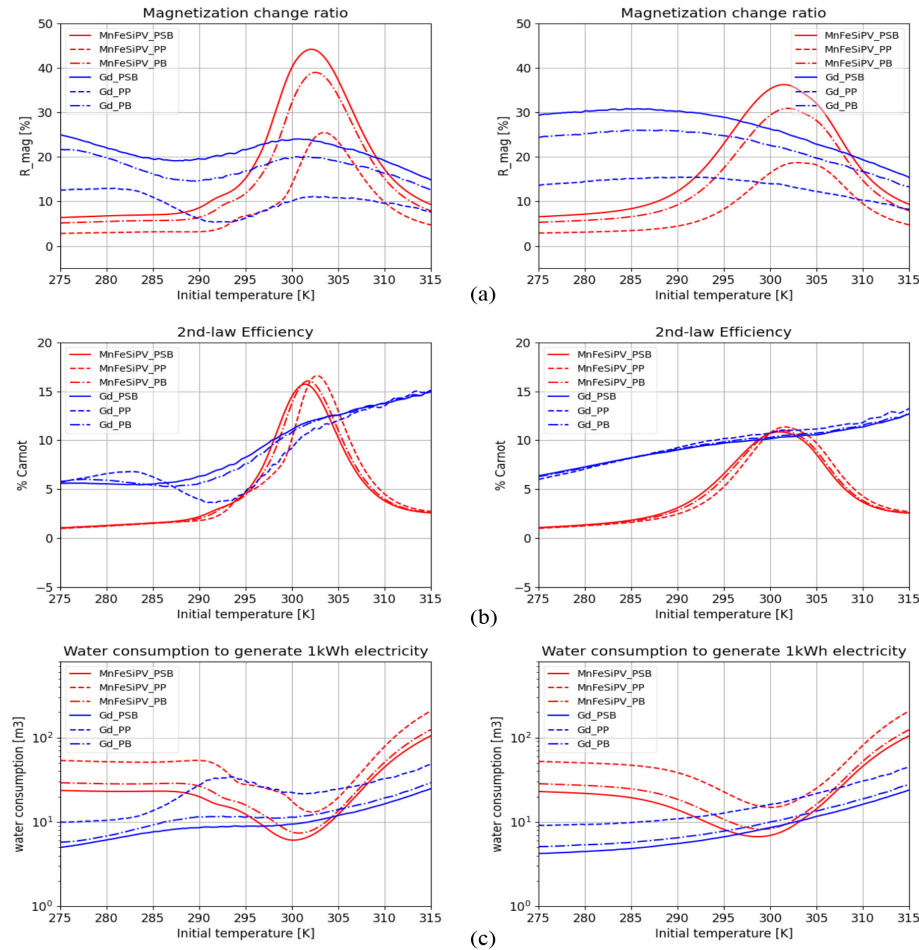


Figure 5.15: Performance result versus initial temperature of the MCM with the analysis variables set $G_f = 0.6 \times 10^{-3} \text{ m}$, $\varepsilon = 30 \%$, $T_h = 333 \text{ K}$, $\dot{V} = 2.17 \times 10^{-5} \text{ m}^3/\text{s}$, plots in left column are the results considering MCE while right column are the results ruling out MCE

One can notice in Fig. 5.12-5.15, the MCE indeed contributes to the temperature change of the MCM, but only when the initial temperature is near T_c of the MCM. The size of the contribution of MCE is inversely proportional to the volumetric flow rate of HTF. Moreover, MnFePSiV has an obvious peak of performance around its T_c at any volumetric flow rate, while Gd only shows a gentle peak around its T_c at very low flow rate, and at high flow rate all performance trends become monotonically decreasing over an elevating initial temperature. Thanks to this peak of performance, MnFePSiV outperforms Gd in an approximately 10 K temperature window (we call it the working temperature window) around its T_c under low flow rate condition. This “out-performing”

temperature window will widen and extend mostly toward lower temperature with increasing flow rate. Besides, contribution of the MCE is much more significant in the case of FOMT MCM than those of SOMT. Take the most pronounced case – MnFePSiV with PSB geometry for example, when the flow rate $\dot{V} = 1.6 \times 10^{-7}$, 9.26×10^{-6} , 1.75×10^{-5} and $2.17 \times 10^{-5} \text{ m}^3/\text{s}$, the peak magnetization change percentage contributed by the MCE is always around 10%. As that of Gd, also with PSB geometry, the magnetization change percentage contributed by the MCE is around 6%.

Another important point is, the volumetric flow rate has to be large enough to suppress the cooling effect from demagnetization. In Fig. 5.12 under the case $\dot{V} = 1.6 \times 10^{-7} \text{ m}^3/\text{s}$, the MCE of Gd has a negative contribution to the magnetization change, due to its famous second order magnetic phase transition (SOMT) behavior, which has a large adiabatic temperature change over a wide temperature span. Therefore, the heat contribution of the heat transfer fluid should be large enough to move the temperature of Gd away from its Curie temperature. On the contrary, the MnFePSiV (a typical MCM with first order phase transition (FOMT)) does not experience such a difficulty, even with the extremely low flow rate case. This different indicate that comparing with the SOMT MCMs, the FOMT MCMs can benefit from easier magnetic state switching.

The second law efficiency is a very interesting aspect. As the heat inflow has a big impact on the efficiency, so the system becomes less efficient when more heat is absorbed. Thus, the geometries with better heat transfer coefficient like PSB and PB have lower efficiency than PP here. Regarding the contribution of the MCE, without MCE both Gd and MnFePSiV result a system efficiency equal to 10% of Carnot engine. However, when MCE is enabled, MnFePSiV has a spectacular 50% improvement in efficiency at its Curie Temperature, while Gd has an improvement of around 23%. Besides, the volumetric flow rate has very little impact on the second law efficiency of both Gd and MnFePSiV. For all geometries, the efficiency goes slightly downward with increasing flow rate.

When it comes to the consumption of HTF per kWh electricity generation, the Gd outperforms MnFePSiV in most of the temperature range except in a very small temperature window near the Curie temperature of MnFePSiV. However, when MCE is enabled, the temperature window enlarges from 5 K at $\dot{V} = 1.6 \times 10^{-7} \text{ m}^3/\text{s}$, to 8 K at $\dot{V} = 2.17 \times 10^{-5} \text{ m}^3/\text{s}$. By enabling MCE, the MnFePSiV requires 12% - 16% less HTF than Gd near its Curie Temperature, this value has a positive correlation with the flow rate. Regarding the geometries, PSB has the lowest HTF consumption thanks to its great heat transfer coefficient, PB following PSB consumes a few percent more, PP has the highest HTF consumption. The HTF consumption decreases with increasing flow rate, because increasing the flow rate improves the heat transfer coefficient in all geometries. Last but not least, the spikes in the Fig. 5.12(c) are caused by the singularities between the

negative to positive values of magnetization change in Gd, which will not happen when the MCE is switched off.

MCE has a significant contribution in the thermodynamic cycle of TMM. Therefore, we take MCE into account in all the simulation cases listed below. Besides, for a better observation of the influence of the volumetric flow rate on the performance, we plot the performance metrics as a function of flow rate. The performance metrics indicated below are either the peak value of each case, or the value at the MCM's T_c in the case of a linear relation.

During the 2nd batch of simulations, we shift our focus from the independent simulation cases on control parameter sets of initial temperature and independent flow rate points to the configuration parameters i.e. the temperature of the heat source, the geometry feature size and the porosity of the heat exchanger. Beside the main input parameters listed in table 1, the analysis variables are listed below:

- geometry feature size $D_g = 0.6 \times 10^{-3}$, 0.4×10^{-3} , 0.2×10^{-3} m (this represents the fibre diameter in PSB, the average sphere diameter in PB, and the plate thickness in PP)
- porosity $\varepsilon = 15\%$, 30% , 45%
- HTF temperature $T_h = 313$, 333 , 353 K
- HTF volumetric flow rate range $\dot{V} = 1.6 \times 10^{-7} \leq \dot{V} \leq 1.67 \times 10^{-5}$ m³/s

The resulting performance metrics are plotted as a function of the flow rate of the hot HTF to reveal the trend of system performance over different input. In order to maximize the contribution of MCE, we assume the initial temperature of the MCM is always at its Cuire temperature.

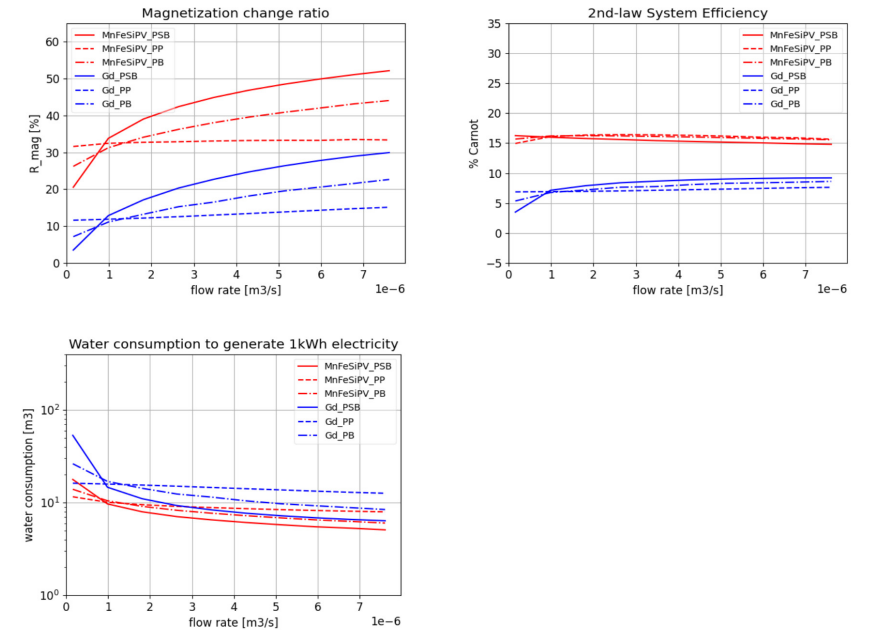


Figure 5.16: Performance result versus volumetric flow rate of the MCM with the analysis variables set $G_f = 0.4 \times 10^{-3}$ m, $\varepsilon = 30\%$, $T_h = 333$ K, the base case for all the following results

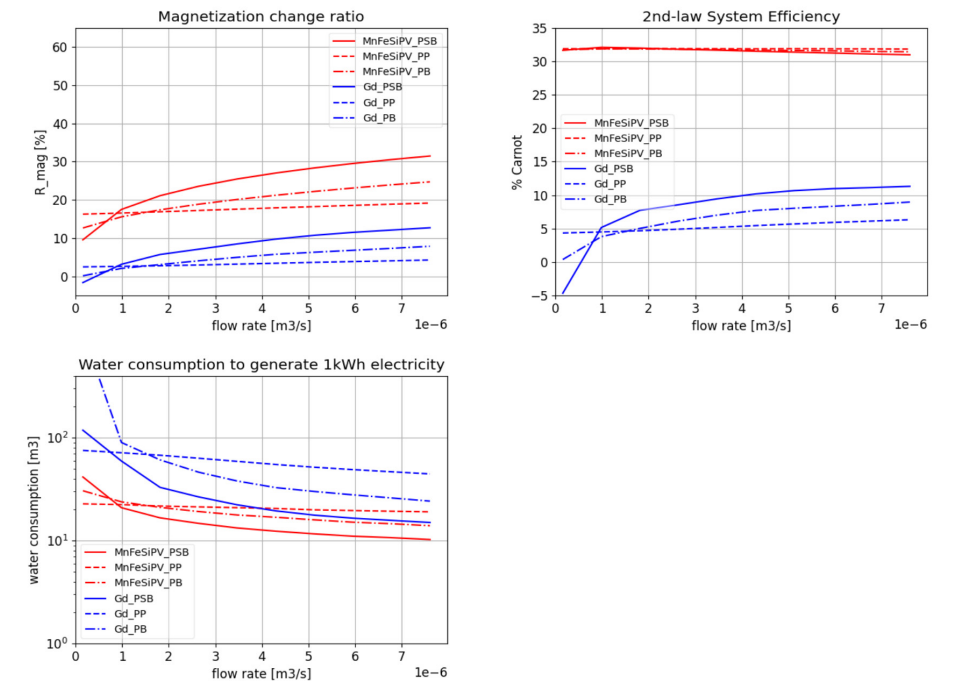


Figure 5.17: Performance result versus volumetric flow rate of the MCM with the analysis variables set $G_f = 0.4 \times 10^{-3}$ m, $\varepsilon = 30\%$, $T_h = 318$ K.

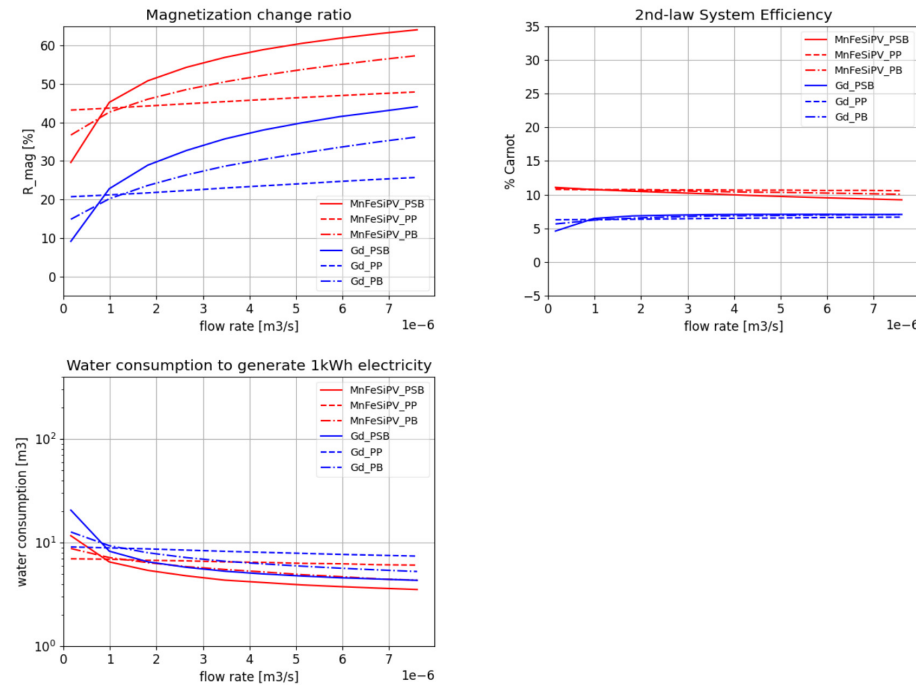


Figure 5.18: Performance result versus volumetric flow rate of the MCM with the analysis variables set $G_f = 0.4 \times 10^{-3} \text{ m}$, $\varepsilon = 30 \%$, $T_h = 348 \text{ K}$

In the first group of simulations we vary the hot flow temperature, which is the most direct control parameter in a TMM application – the “waste heat” itself. We have chosen three temperature settings: 318 K, 333 K, 348 K, with a 15 K increase, we hope to see how the geometries benefit from the temperature of the hot source. (333 K is used as base case for performance analysis of other configuration parameters.) the results are shown in Fig. 5.16 – 5.18. We can see that for the magnetization change, the PSB starts lowest but rises the fastest with increasing flow rate, while the PP starts at the highest place but ramps up very slowly and falls behind other two geometries at a flow rate between 0.5×10^{-6} to $1 \times 10^{-6} \text{ m}^3/\text{s}$, the PB takes a middle path between the other two geometries. The MnFePSiV has overall higher magnetization change percentage than Gd, the difference between these two MCMs has a negative correlation with the flow rate. The magnetization change percentage of both Gd and MnFePSiV positively scale with HTF temperature.

With second law efficiency, in MnFePSiV the PSB starts highest and drops below PP and PB with increase of flow rate. With any flow rate above $1 \times 10^{-6} \text{ m}^3/\text{s}$, the PSB has the lowest system efficiency. In Gd, this trend is totally reversed, the PSB starts at the lowest position and goes above PB and PP at flow rate above $1 \times 10^{-6} \text{ m}^3/\text{s}$, this is mainly due to

the larger thermal conductivity of Gd, the efficiency of heat transfer scales much better than that of MnFePSiV. Therefore, the second law efficiency of MnFePSiV is trending downward with increasing flow rate, while the trend in Gd is just the opposite. Lower HTF temperature results in higher efficiency, and larger efficiency difference between Gd and MnFePSiV. With HTF temperature at 318 K, the second law efficiency of MnFePSiV is 6 times of that with Gd with low flow rate, the ratio goes down to 2 times with HTF temperature at 348 K.

When it comes to the HTF consumption, the correlation becomes very simple. The consumption is reduced by higher heat transfer coefficient and higher temperature difference. Therefore, PSB always has lowest consumption, followed by PB, and PP has the highest consumption. With higher flow rate, the consumption of HTF decreases. When the HTF temperature increases from 318 K to 333 K, the consumption decreases almost 10 times almost all cases. However, when the HTF temperature increase further from 333 K to 348 K, the consumption only decreases by around 2 times. This is a combined effect of suppressed MCE (when the temperature of MCM is too far away from Curie temperature) and lower magnetization change in the paramagnetic region. Thanks to the intensive FOMT, MnFePSiV outperforms Gd in all cases regarding the HTF consumption, this advantage becomes even larger when lower HTF temperature is applied.

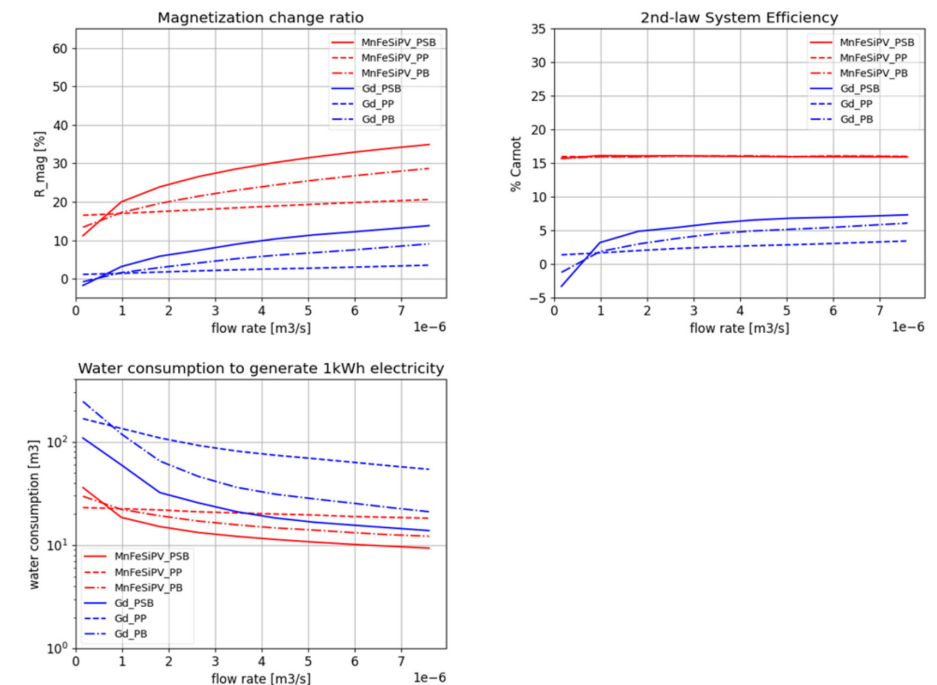


Figure 5.19: Performance result versus volumetric flow rate of the MCM with the analysis variables set $G_f = 0.6 \times 10^{-3} \text{ mm}$, $\varepsilon = 30 \%$, $T_h = 333 \text{ K}$.

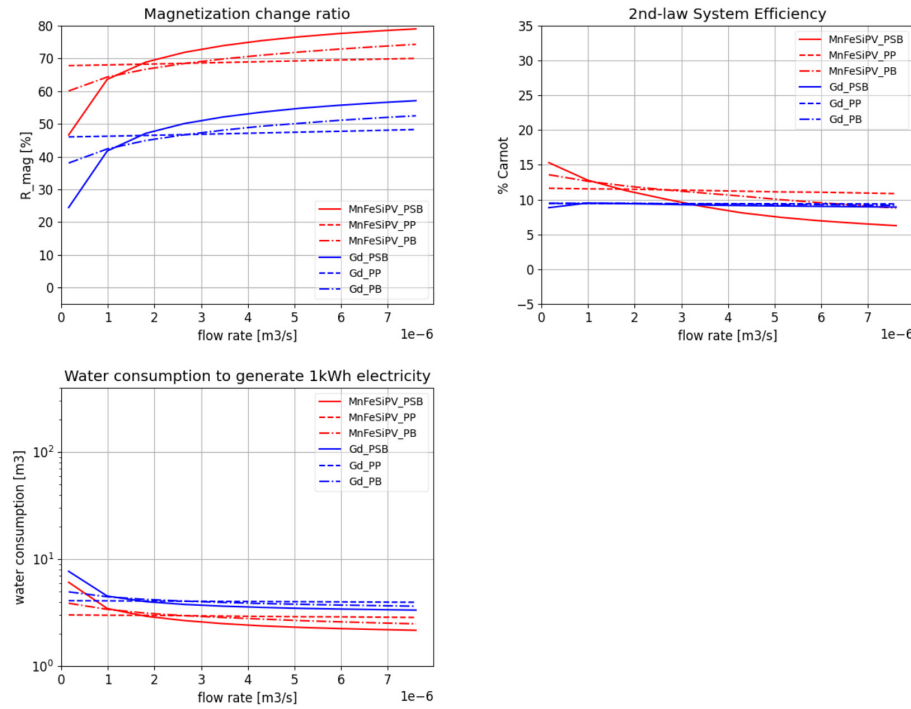


Figure 5.20: Performance result versus volumetric flow rate of the MCM with the analysis variables set $G_f = 0.2 \times 10^{-3} \text{ m}$, $\varepsilon = 30 \%$, $T_h = 333 \text{ K}$.

The second group of simulations focused on the influence of the geometry feature size of the MCM. The $0.4 \times 10^{-3} \text{ m}$ is the base case, and we compare it with the cases of $0.6 \times 10^{-3} \text{ m}$ and $0.2 \times 10^{-3} \text{ m}$, the results are listed in Fig. 5.16, Fig. 5.19 and Fig. 5.20. In this group of simulations, we can see that:

Most correlations and trends between the MCMs, geometries, and flow rate are similar to the first simulation group in the case of $G_f = 0.6 \times 10^{-3} \text{ m}$. However, when the geometry feature size becomes $0.2 \times 10^{-3} \text{ m}$, the magnetization change percentage gets a large boost in both Gd and MnFeSiV, in all geometries, this value reaches its highest level among all simulation cases. In the meantime, the HTF consumption also reaches its lowest level among all cases. Regarding the second law efficiency, when feature size becomes $0.2 \times 10^{-3} \text{ m}$, the difference between geometries over the whole range of flow rate in the case of MnFeSiV becomes more significant while the in the case of Gd, the difference becomes much less comparing with other simulation cases. This may be caused by the sharp ferro-to-para magnetic state transition with MnFeSiV, and as for Gd, the temperature change may be too large and it brings Gd into paramagnetic state even at low flow rate.

Similarly, as in the first simulation group, regarding the trend of magnetization change, PSB has low initial values but a high growth rate, PP has high initial values but a low growth rate, PB is in between. PP falls behind PSB and PB at a flow rate between 0.05×10^{-5} to $0.1 \times 10^{-5} \text{ m}^3/\text{s}$.

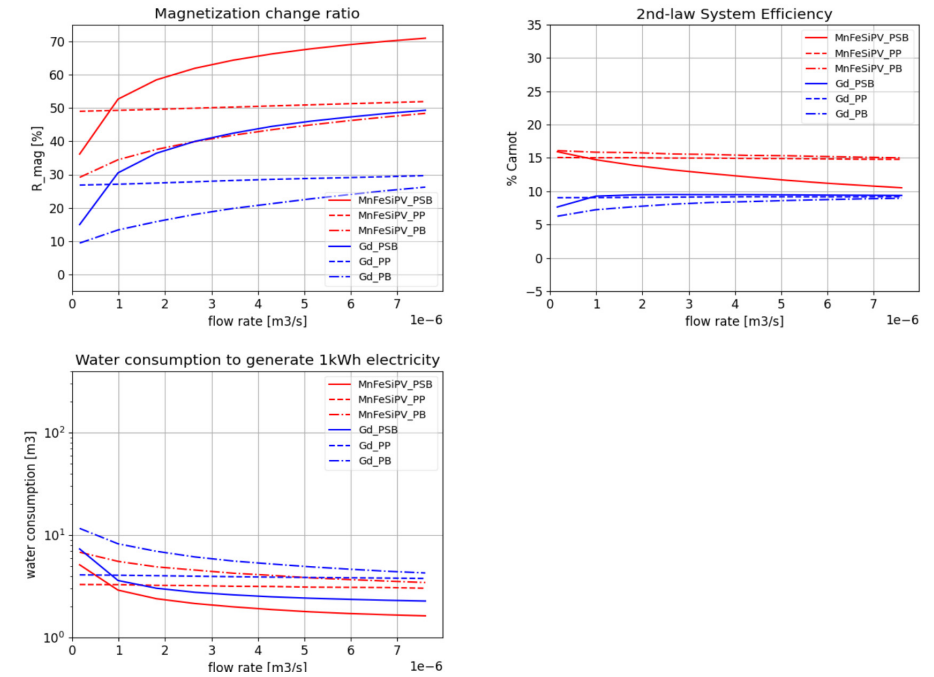


Figure 5.21: Performance result versus volumetric flow rate of the MCM with the analysis variables set $G_f = 0.4 \times 10^{-3} \text{ mm}$, $\varepsilon = 20 \%$, $T_h = 333 \text{ K}$.

The third group of simulations focuses on the influence of the porosity of the MCM. 30% is the base case, and we compare it with the cases of 20% and 40%, the results are listed in Fig. 5.16, Fig. 5.21 and Fig. 5.22.

As shown in Fig. 21, when the porosity decreases to 20%, all three geometries show increases in magnetization change. However, PSB has a much larger rise in comparison with PP and PB, and consumes much less HTF than PP and PB. At the largest flow rate, all the performance parameters of PSB almost reaches the same level as in the case of $G_f = 0.2 \times 10^{-3} \text{ m}$ (see Fig. 5.20).

The situation becomes very interesting in Fig. 22, when the porosity increases to 40%, the PB for the first time have the highest magnetization change and lowest HTF consumption among the three geometries, about 8% higher than PSB and 25% higher than PP.

Efficiency wise, we see the efficiency becomes dramatically lower in the case of Gd when applies 40% porosity, this is due the reduction on heat transfer coefficient in Gd, and for Gd, temperature change is majorly caused by heat transfer from HTF.

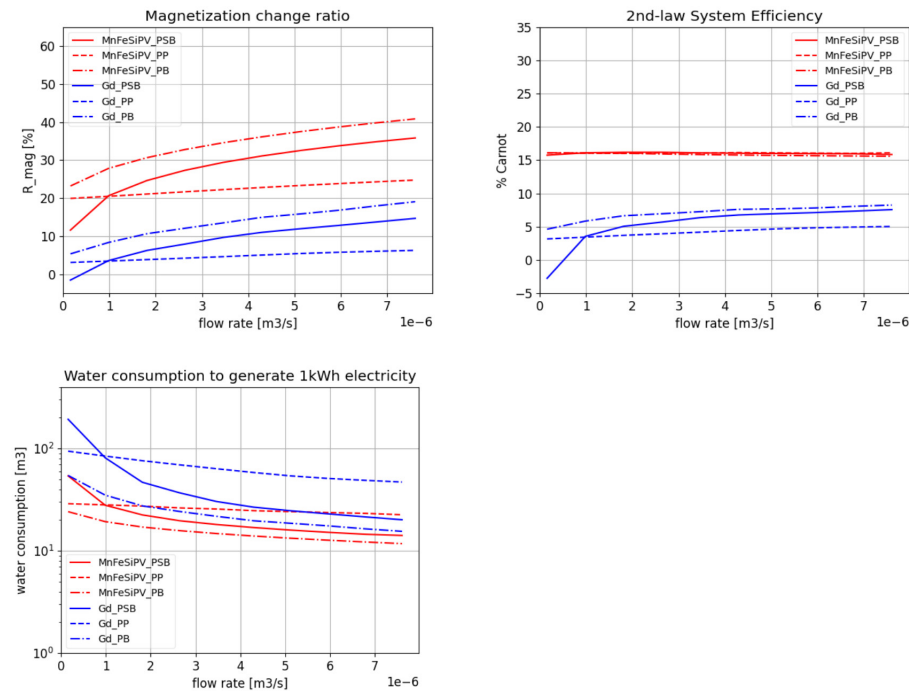


Figure 5.22: Performance result versus volumetric flow rate of the MCM with the analysis variables set $G_f = 0.4 \times 10^{-3} \text{ mm}$, $\varepsilon = 40 \%$, $T_h = 333 \text{ K}$,

5.4.4 Result discussion

All the simulations in this work are based on lumped parameter analysis, we notice that the Biot number is quite large in some cases. To more accurately solve this one-dimensional transient conductive problem, other analysis tools like the Heisler chart method or implicit space-time method are needed. However, either method will make the model more complicated and time consuming. Given the fact that the lumped analysis approach assumes the entire block of material has a uniform temperature instead of a

temperature gradient, it tends to overestimate the temperature change caused by HTF flow. This will suppress the MCE effect, and lift the performance of the heat exchange process. Therefore, when lumped parameter analysis is applied, one should notice that the MCE effect would contribute more than the current results indicate, the geometries with a high heat transfer coefficient would have outperformed the other geometries more.

From the material property aspect: thanks to its low specific heat capacity and outstanding thermal conductivity Gd has higher total temperature change than MnFePSiV or any FOMT type MCM in a wide temperature span. Besides, Gd also has a large gradual magnetization change over a large temperature span. This feature makes it very tolerable for any control parameters, very beneficial for prototyping and trialing. However, the MnFePSiV has higher magnetization change than Gd within a small temperature span near its Curie Temperature, combined with its intensive MCE. Therefore, with a good control of initial temperature and an adequate flow rate, one just has to change the temperature of MnFePSiV by a small amount to achieve a high magnetization change, which will then result in a better efficiency than for Gd. With this consideration, we can imagine that similar to the multi-layer magnetocaloric regenerator, we can also apply a multi-layer heat exchanger in TMM. As there always is a temperature gradient in the heat exchanger along the flow direction, only a well-designed multi-layer heat exchanger with the Cuire temperatures of the MCM nicely aligned with the gradient can offer maximum magnetic force output.

From the heat exchanger geometry aspect: Among the three types of geometry, under the same geometry constrain. The packed screen bed has the highest heat transfer coefficient and moderate pressure drop compared to the parallel plate and packed bed geometry. The parallel plate geometry, has the lowest pressure drop and a moderate heat transfer coefficient; The packed bed, has the lowest heat transfer and the highest pressure drop amount the three. However, one additional feature for these three geometries is the specific surface area. The pack bed has the highest specific surface area, the PSB has slightly less, and the PP has the least.

Among the three configuration parameters, geometry feature size has the largest impact on the performance, followed by the porosity, and the temperature of the heat source has the least impact. However, judging from the complexity of implementation, the order is just the opposite, the temperature of the heat source has the lowest complexity to adjust, the porosity of the MCM requires some engineering work, while the geometry feature size is not always possible to adjust, the finer it goes the more complicated it becomes.

5.5 CONCLUSIONS

The performance of the thermomagnetic motor prototype is relatively low. This was expected, because the magnetocaloric properties of the current 3D printed mesh structures are not ideal for city conditions. To reach high performance, the T_c of the heat exchanger units which is now at $T_c = 273\text{ K}$ (0°C) need to be higher in the range of $T_c = 313\text{ K}$ (40°C). However, thanks to the strong magnetic field source, the MCM blocks can still generate enough torque to move the rotary wheel in our experiment. This also means a high magnetic field will bring higher system efficiency.

It proves to be very challenging to optimize the chemical composition of the MCM, due to its extreme sensitivity to post processing procedures like 3D printing and heat treatment. The chemical composition, production and processing of the magnetocaloric materials and heat exchangers need to be further optimized to obtain better control of the T_c . The magnetocaloric properties are very sensitive to changes in the chemical composition, processing with 3D printing and heat treatment. The chemical composition, 3D printing process, paste refinement of the mixture of MCM and lubricant as well as the heat treatment need to be further optimized for the 3D printed structure to increase the efficiency of waste heat to power conversion in a thermomagnetic motor.

The magnetic transition is on the edge of the range of suitable temperatures. In the next step, the chemical composition and heat treatment needs to be further optimized to increase ΔM and reach higher temperatures of the T_c in the future 3D mesh structure, which will increase the performance for waste heat to power conversion in a thermomagnetic motor. By definition, the 3D mesh blocks produced by Magneto can be seen as a PSB, which is the best choice among the popular heat exchanger geometries.

From the simulation results of our explicit TMM model, we can conclude that the FOMT MCM like MnFePSiV can outperform Gd within a 10 K temperature window around its Curie temperature. Therefore, the flow rate should be matching the volume of the MCM applied in the heat exchanger, to avoid moving the temperature of MCM too far from its Curie temperature. Among all three popular heat exchanger geometries, pack screen bed (PSB) has the best overall performance thanks to its high heat transfer coefficient and low pressure drop. By applying optimal control parameters, PSB geometry, a simulated TMM with MnFePSiV can have 50% higher efficiency than Gd under the same conditions. The Magnetocaloric heat exchanger in TMM works in a passive way in which the temperature changes mainly introduced by the flow of hot and cold water. This feature works very well when the structure of the heat exchanger stays relatively simple, there, the temperature gradient is easy to control. However, when a multilayer structure is applied, the temperature gradient will be more difficult to control, especially when the

MCE effect is also utilized. The temperature change caused by both the MCE effect and the water flow can be hard to predict and to utilize, a good thermodynamic model is essential!

REFERENCES

- [1] M. Papapetrou, G. Kosmadakis, A. Cipollina, U. La Commare, G. Micale, Industrial waste heat: Estimation of the technically available resource in the EU per industrial sector, temperature level and country, *Applied Thermal Engineering*, 138 (2018) 207-216.
- [2] C. Forman, I.K. Muritala, R. Pardemann, B. Meyer, Estimating the global waste heat potential, *Renewable and Sustainable Energy Reviews*, 57 (2016) 1568-1579.
- [3] C. Liu, P. Chen, K. Li, A 1 KW thermoelectric generator for low-temperature geothermal resources, in: *Proceedings of the Thirty-Ninth Workshop on Geothermal Reservoir Engineering*, Stanford, CA, USA, 2014, pp. 24-26.
- [4] A. Nozariasbmarz, H. Collins, K. Dsouza, M.H. Polash, M. Hosseini, M. Hyland, J. Liu, A. Malhotra, F.M. Ortiz, F. Mohaddes, V.P. Ramesh, Y. Sargolzaeiaval, N. Snouwaert, M.C. Öztürk, D. Vashae, Review of wearable thermoelectric energy harvesting: From body temperature to electronic systems, *Applied Energy*, 258 (2020) 114069.
- [5] K. Li, G. Garrison, M. Moore, Y. Zhu, C. Liu, R. Horne, S. Petty, An expandable thermoelectric power generator and the experimental studies on power output, *International Journal of Heat and Mass Transfer*, 160 (2020) 120205.
- [6] K. Gaurav, S.K. Pandey, Efficiency calculation of a thermoelectric generator for investigating the applicability of various thermoelectric materials, *Journal of Renewable and Sustainable Energy*, 9 (2017) 014701.
- [7] M. Chen, H. Lund, L.A. Rosendahl, T.J. Condra, Energy efficiency analysis and impact evaluation of the application of thermoelectric power cycle to today's CHP systems, *Applied Energy*, 87 (2010) 1231-1238.
- [8] W. Poprawski, Z. Gnutek, J. Radojewski, R. Poprawski, Pyroelectric and dielectric energy conversion – A new view of the old problem, *Applied Thermal Engineering*, 90 (2015) 858-868.
- [9] J.-Y. Yu, L. Liu, The Prospect and Analysis of Nanogenerator for Wearable Devices, in: *Springer International Publishing*, 2019, pp. 75-91.
- [10] A. Potnuru, Y. Tadesse, Characterization of Pyroelectric Materials for Energy Harvesting from Human Body, *Integrated Ferroelectrics*, 150 (2014) 23-50.
- [11] R.A. Surmenev, R.V. Chernozem, I.O. Pariy, M.A. Surmeneva, A review on piezo- and pyroelectric responses of flexible nano- and micropatterned polymer surfaces for biomedical sensing and energy harvesting applications, *Nano Energy*, 79 (2021) 105442.
- [12] E. Garofalo, M. Bevione, L. Cecchini, F. Mattiussi, A. Chiolerio, Waste Heat to Power: Technologies, Current Applications, and Future Potential, *Energy Technology*, (2020) 2000413.
- [13] A. Waske, D. Dzekan, K. Sellschopp, D. Berger, A. Stork, K. Nielsch, S. Fähler, Energy harvesting near room temperature using a thermomagnetic generator with a pretzel-like magnetic flux topology, *Nature Energy*, 4 (2019) 68-74.
- [14] M. Gueltig, F. Wendler, H. Ossmer, M. Ohtsuka, H. Miki, T. Takagi, M. Kohl, High-Performance Thermomagnetic Generators Based on Heusler Alloy Films, *Advanced Energy Materials*, 7 (2017) 1601879.
- [15] X. Liu, H. Chen, J. Huang, K. Qiao, Z. Yu, L. Xie, R.V. Ramanujan, F. Hu, K. Chu, Y. Long, H. Zhang, High-performance thermomagnetic generator controlled by a magnetocaloric switch, *Nature Communications*, 14 (2023).
- [16] K. Murakami, M. Nemoto, Some experiments and considerations on the behavior of thermomagnetic motors, *IEEE Transactions on Magnetics*, 8 (1972) 387-389.
- [17] C.-C. Cheng, T.-K. Chung, C.-C. Chen, H.-M. Wang, A Rotational Actuator Using a Thermomagnetic-Induced Magnetic Force Interaction, *IEEE Transactions on Magnetics*, 54 (2018) 1-8.
- [18] M. Ujihara, G.P. Carman, D.G. Lee, Thermal energy harvesting device using ferromagnetic materials, *Applied Physics Letters*, 91 (2007) 093508.
- [19] T.A. Edison, Pyromagnetic generator (US patent 476,983), (1888).
- [20] N. Tesla, Thermo-Magnetic Motor (US patent 396,121), (1889).
- [21] V.K. Pecharsky, K.A. Gschneidner, Giant magnetocaloric effect in Gd-5(Si₂Ge₂), *Physical Review Letters*, 78 (1997) 4494-4497.
- [22] G.H. Kaneko, A.C. Souza, F. Moro, F.C. Colman, W.A.S. Conceição, C.S. Alves, P.V. Trevizoli, Design and assembling of a magnetic circuit for a thermomagnetic motor apparatus, *Journal of the Brazilian Society of Mechanical Sciences and Engineering*, 41 (2019) 394.
- [23] M. almanza, morgan.almanza@gmail.com, A. Pasko, A. Bartok, F. Mazaleyra, M. Lobue, Thermal energy harvesting: thermomagnetic versus thermoelectric generator, in: *7th International Conference on Magnetic Refrigeration at Room Temperature (Thermag VII)*, Turin, Italy, 2016.
- [24] C.S. Alves, F.C. Colman, G.L. Foleiss, G.T.F. Vieira, W. Szpak, Numerical simulation and design of a thermomagnetic motor, *Applied Thermal Engineering*, 61 (2013) 616-622.
- [25] P. Coray, D. Wymann, R. Brunner, N. Vida, Fully Operational Prototype of a 1kW Thermo-Magnetic Motor for Generating Electricity from < 80°C Heat, Abstract for the Delft Days on Magneto Calorics, DDMC, (2015).
- [26] J. Hey, M. Repaka, T. Li, J.L. Tan, Design Optimization of a Rotary Thermomagnetic Motor for More Efficient Heat Energy Harvesting, *Energies*, 15 (2022) 6334.
- [27] C.-J. Hsu, S.M. Sandoval, K.P. Wetzlar, G.P. Carman, Thermomagnetic conversion efficiencies for ferromagnetic materials, *Journal of Applied Physics*, 110 (2011).
- [28] R.A. Kishore, S. Priya, Low-grade waste heat recovery using the reverse magnetocaloric effect, *Sustainable Energy & Fuels*, 1 (2017) 1899-1908.
- [29] J.C. Armour, J.N. Cannon, Fluid flow through woven screens, *Aiche Journal*, 14 (1968) 415-420.
- [30] J.-W. Park, D. Ruch, R. Wirtz, Thermal/fluid characteristics of isotropic plain-weave screen laminates as heat exchange surfaces, in: *40th AIAA Aerospace Sciences Meeting & Exhibit*, 2012.
- [31] S. Ergun, A.A. Orning, Fluid Flow through Randomly Packed Columns and Fluidized Beds, *Industrial & Engineering Chemistry*, 41 (1949) 1179-1184.
- [32] N. Wakao, T. Funazkri, Effect of fluid dispersion coefficients on particle-to-fluid mass transfer coefficients in packed beds: Correlation of sherwood numbers, *Chemical Engineering Science*, 33 (1978) 1375-1384.
- [33] M. Nickolay, H. Martin, Improved approximation for the Nusselt number for hydrodynamically developed laminar flow between parallel plates, *International Journal of Heat and Mass Transfer*, 45 (2002) 3263-3266.
- [34] A. Bejan, Entropy generation minimization: the method of thermodynamic optimization of finite-size systems and finite-time processes, CRC press, 2013.

APPENDICES

Summary
Nederlandse samenvatting
Curriculum vitae
Acknowledgements

SUMMARY

In this PhD thesis the focus is centered on the development of magnetocaloric heat pumps and thermomagnetic motors. To maximize the performance of these systems, the available knowledge from system engineering, material shaping techniques and innovative device approaches are combined to optimize the performance of magnetocaloric devices and materials under varying operating conditions. In pursuit of this goal, extensive experiments and simulations were conducted to analyze the system efficiency and performance, and developed novel methods to ensure the optimal functioning of magnetocaloric devices.

In **Chapter 3** the first implemented cooling system, a magnetic refrigerator prototype MMFF Cooler, has been developed as a proof-of-principle. It has a reciprocating system with two permanent magnetic field sources of 1.2 T and uses 0.7 mm thick gadolinium plate as its working material. The MMFF Cooler can reach a maximum temperature span of 6.1 K with a 2 Hz AMR frequency, 1400 ml/min volumetric flow rate, and hot end temperature of 31°C. The prototype design meets the requirements of a proof-of-principle device, but the system's efficiency is far from optimal. The system's performance can be tuned by controlling the parameters with the servo motor and gear pump. The system design is still quite immature due to heat leak and dead volume, which significantly limit cooling power and extend the cooling time. The use of too many customized components suppresses the system performance and makes modification and expansion difficult. Lastly, the shaping of the gadolinium plates and the assembly mechanism needs improvement, as the large thickness of the Gd plate reduces the heat transfer efficiency and causes significant deformation when it leaves the field region.

In **Chapter 4** the subsequent cooling system was developed in the form of a rotary room-temperature AMR prototype. This device is named the FAME Cooler, the purpose is to investigate the magnetocaloric properties of different materials, as well as to further explore the room temperature magnetocaloric refrigeration technology. This device offers extensive control over AMR cycles, including the working frequency, flow rate, hot end temperature, blow fraction, phase offset, and operation mode. It also allows for easy modification of the regenerator, such as replacing the MCM or changing the number of beds. The device's performance is promising, outperforming similar scale devices globally. The rotary magnetic field source generates an average magnetic field of 0.875 T within a volume of 0.71 l. The seven regenerators are placed in an asymmetrical layout and hold in total 1.18 kg of gadolinium spheres. It achieved a maximum zero power temperature span of 11.6 K, a maximum zero-span cooling power of 162.4 W, and a simplified COP of 1.59 under specific conditions. A maximum simplified COP of 1.85 was achieved under optimal conditions. Fine-tuning the system control parameters

can further optimize its performance. The duration of the flow significantly affects the performance, especially at low heat loads. Shorter flow durations allow for precise fine tuning towards larger temperature spans. However, this becomes irrelevant when the focus lies on the cooling power.

In **Chapter 5** the third developed system, a thermomagnetic Motor (TMM) prototype called TMM0, has been developed. It uses a wheel with magnetocaloric material (MCM) to create a rotating movement by continuously magnetizing and demagnetizing the material. The magnetic force is controlled by changing the MCM's temperature with the flow of cold and hot water. The prototype has 24 Magnetocaloric Heat Exchanger (MCHE) units mounted along the wheel's outer edge and an N-shaped permanent magnet assembly generating a 1.35-1.5 T field in the center of its air gap. The wheel rotates when a net magnetic force is applied to it, with all MCHEs entering and exiting the magnetic field successively. The wheel's rotating movement is stabilized by maintaining a constant flow of cold and hot water to the MCHEs on both sides of the magnet. At present, the TMM0 system is still in its early development stage. Even at the highest tested temperature span of 50 K, with both the cold and hot flow rate set at 3.2 Lpm, the average power generation from the TMM0 is only around 25 W. This value is lower than the energy consumption of the pumps, which is about 50 W. Therefore, the TMM0 is unable to generate any net power by harvesting the heat from the water streams at this moment. Via numerical simulation through an explicit TMM model, it can be concluded that the FOMT MCM MnFePSiV can work better than Gd in a 10 K temperature range around its Curie temperature. Among the three popular heat exchanger geometries, the pack screen bed (PSB) performs the best. By using optimal control parameters and the PSB geometry, a simulated TMM with MnFePSiV can have 50% higher efficiency than Gd. When using a multilayer structure, the control of the temperature gradient becomes more difficult, especially when the MCE effect takes place. The TMM numerical model has to be further developed to fully optimize the system.

NEDERLANDSE SAMENVATTING

Dit proefschrift is gericht op de ontwikkeling van magnetocalorische warmtepompen en thermomagnetische motoren. Om de prestaties van deze systemen te maximaliseren, de beschikbare kennis van systeemengineering en materiaalvormingstechnieken geïntegreerd en innovatieve methoden bedacht om de prestaties van magnetocalorische apparaten en materialen onder wisselende bedrijfsomstandigheden te optimaliseren. Met dit doel voor ogen zijn er uitgebreide experimenten en simulaties uitgevoerd om de systeemefficiëntie en prestaties te analyseren en nieuwe methoden ontwikkeld om het optimaal functioneren van magnetocalorische apparaten te waarborgen.

In **Hoofdstuk 3** is het eerste prototype van een magnetische koelkast, de MMFF Cooler, ontwikkeld als een proof-of-principle. Het heeft een heen-en-weer bewegend systeem met twee permanente magnetische veldbronnen van 1,2 T en gebruikt een gadoliniumplaat van 0,7 mm dik als actief materiaal. De MMFF Cooler kan een maximaal temperatuursverschil van 6,1 K bereiken met een 2 Hz AMR-frequentie, een volumetrische doorstroming van 1400 ml/min en een hot-end temperatuur van 31°C. Het ontwerp van het prototype voldoet aan de eisen van een proof-of-principle apparaat, maar de efficiëntie van het systeem is verre van optimaal. De prestaties van het systeem kunnen worden afgestemd door de parameters af te regelen met de servomotor en tandwielpomp. Het systeemontwerp is nog vrij rudimentair vanwege warmteverlies en dode volume, die de koelcapaciteit aanzienlijk beperken en de koeltijd verlengen. Het gebruik van te veel aangepaste componenten beperkt de systeemprestaties en maakt modificatie en uitbreiding moeilijk. Tot slot moet de vorming en assemblage-mechanisme van de gadoliniumplaat worden verbeterd, omdat de grote dikte van de Gd-plaat de warmteoverdrachtsefficiëntie vermindert en een aanzienlijke vervorming veroorzaakt wanneer deze de veldregio verlaat.

In **Hoofdstuk 4** het volgende koelsysteem was ontwikkeld in de vorm van een roterend kamer temperatuur AMR-prototype, genaamd de FAME Cooler, met als doel de magnetocalorische eigenschappen van verschillende materialen te onderzoeken en de magnetocalorische koeltechnologie op kamertemperatuur verder te verkennen. Dit apparaat biedt uitgebreide controle over AMR-cycli, inclusief werkfrequentie, doorstroomsnelheid, hot-end temperatuur, blow fractie, fase offset en bedieningsmodus. Het maakt ook gemakkelijke aanpassingen van de regenerators mogelijk, zoals het vervangen van de MCM of het wijzigen van het aantal bedden. De prestaties van het apparaat zijn veelbelovend en overtreffen soortgelijke apparaten wereldwijd. De roterende magnetische veldbron genereert een gemiddeld magnetisch veld van 0,875 T binnen een volume van 0,71 l. De zeven regenerators zijn asymmetrisch geplaatst en bevatten in totaal 1,18 kg gadolinium bolletjes. Het behaalde een

maximaal nul-energieverbruik temperatuursverschil van 11,6 K, een maximale nul-span koelingvermogen van 162,4 W en een vereenvoudigde COP van 1,59 onder specifieke omstandigheden. De maximale vereenvoudigde COP van 1,85 werd bereikt onder optimale omstandigheden. Het verfijnen van systeemparemeters kan de prestaties verder optimaliseren. De duur van de doorstroming beïnvloedt de prestaties aanzienlijk, vooral bij lage warmtebelastingen. Een kortere doorstroomduur maakt nauwkeurige afstemming mogelijk voor grotere temperatuursverschillen. Dit wordt echter irrelevant wanneer de focus op het koelvermogen ligt.

In **Hoofdstuk 5** het derde ontwikkelde systeem, een thermomagnetisch motor (TMM) prototype genaamd TMM0, is ontwikkeld. Het gebruikt een magnetocalorisch materiaal (MCM) wiel om een roterende beweging te creëren door het continu magnetiseren en demagnetiseren ervan. De magnetische kracht wordt gecontroleerd door de temperatuur van het MCM te veranderen met de doorstroming van koud en warm water. Het prototype heeft 24 magnetocalorische warmtewisselaar (MCHE) eenheden die langs de buitenrand van het wiel zijn gemonteerd en een N-vormige permanente magneetopstelling die een veld van 1,35-1,5 T genereert in het midden van de luchtspleet. Het wiel draait wanneer er een netto magnetische kracht op wordt uitgeoefend, waarbij alle MCHes achtereenvolgens het magnetisch veld binnengaan en verlaten. De roterende beweging van het wiel wordt gestabiliseerd door een constante doorstroming van koud en warm water naar de MCHes aan beide zijden van de magneet te handhaven. Momenteel bevindt het TMM0-systeem zich nog in een vroeg ontwikkelingsstadium. Zelfs bij het hoogste geteste temperatuursverschil van 50 K, met zowel koude als warme doorstroomsnelheden ingesteld op 3,2 Lpm, is de gemiddelde stroomopwekking van de TMM0 slechts ongeveer 25 W. Dit is lager dan het energieverbruik van de pompen, dat ongeveer 50 W bedraagt. Daarom is de TMM0 momenteel niet in staat om netto vermogen op te wekken door de warmte van de waterstromen te oogsten. Via numerieke simulatie door middel van een expliciet TMM-model kan worden geconcludeerd dat de FOMT MCM MnFePSiV beter kan werken dan Gd in een temperatuurbereik van 10 K rond zijn Curie-temperatuur. Van de drie populaire warmtewisselaar-geometrieën presteert het pack screen bed (PSB) het beste. Door gebruik te maken van optimale controleparameters en PSB-geometrie kan een gesimuleerde TMM met MnFePSiV een 50% hogere efficiëntie hebben dan Gd. Bij gebruik van een meerlaagse structuur wordt het moeilijker om de temperatuurgradiënt te beheersen, vooral wanneer het MCE-effect plaats vindt. Het TMM-numerieke model verder worden ontwikkeld om het systeem volledig te optimaliseren.

ACKNOWLEDGEMENTS

My PhD journey has been an adventure beyond anything I could have imagined when I first took the train from my hometown to Guangzhou or dialed the Skype call to Delft. Over the years, I have transformed from a young man chasing vague dreams into someone with clear and focused goals. This growth has only been possible because of the support and encouragement I've received along the way. I want to take a moment to express my deepest gratitude to all those who have been part of this journey.

First and foremost, I extend my heartfelt thanks to my promoter, Prof. Dr. Ekkes Brück. His energy and enthusiasm for science have been a constant source of inspiration and motivation. I am profoundly grateful for the opportunity to pursue my project within the FAME group, where we pride ourselves on developing the best magnetocaloric materials. Your vast knowledge and practical experience have always met my needs and fueled my curiosity. I vividly remember the afternoon when you demonstrated Lenz's Law with the jumping rings in your office as we discussed eddy currents in magnetocaloric heat pumps. Despite your incredibly busy schedule, you always found time to offer advice and support. I appreciate your easygoing attitude, optimism, and the ideal balance you provided between guidance and independence.

Special thanks go to my co-promoter, Dr. Niels van Dijk. Your scientific rigor and approach to research have constantly motivated me to improve as an engineer. You emphasized the importance of attention to detail in both the preparation and presentation of my work. I deeply appreciate the valuable feedback you provided during our discussions, and I enjoyed listening to your various stories and insights into history and science. Your advice to respect my role and stay focused when I felt lost in my research was instrumental in guiding me through challenging times.

I would also like to acknowledge my colleagues in the FAME group, the Reactor Institute, and DEMO, who provided help, support, and motivation throughout my PhD project. It was a pleasure to work under the same roof as you.

Anton Lefering, thank you for sharing your knowledge about various experimental devices. Your kindness and expertise made my PhD life easier. Jouke Feringa, thank you for assisting with ICT-related issues and introducing me to the computing cluster. Kees Goubitz and Michel Steenvoorden, I appreciate your help in the XRD lab. Michel Thijs, thank you for your guidance on magnetic field simulation. Bert Zwart, I am grateful not only for your introduction to quartz tube processing but also for organizing group social activities—I will always cherish the Christmas family parties and football games in the arena. Ilse van der Kraaij-Quick, Nicole Banga, and Trudy Beentjes, thank you for your

administrative and organizational support.

My sincere thanks go to the DEMO of TU Delft, especially the DEMO-RID team. Without you, none of my designs could have been realized. You provided me with interesting ideas, solutions, and a deeper understanding of engineering. Jeroen Koning and Rene den Oudsten, you were the first to introduce me to the incredible team at DEMO. Andries Oort, your critiques of my unconventional designs were invaluable, and surprisingly you often managed to bring them to life. You showed me that sometimes, things can be accomplished with simply brutal force. Youp van Goozen, Martin van Exter, Ernst van der Wal, Raymon Bresser, Rien Waaijer, Dimitri Kuznetsov, Rene Bakker, Kevin Kamman, and Hugo van der Kort—thank you for your constant support and for sharing your remarkable engineering skills. It was a privilege to work and learn alongside you.

Lian Zhang, Luana Caron, Yibole Hargen, Francois Guillou, Xuefei Miao, N. V. Thang, and Maurits Boeije—you were my first impression of the FAME group. You introduced me to the fascinating world of magnetocaloric materials, helping me understand the principles and adjust my engineering perspective. Xinmin You, Jiawei Lai, Jun Liu, Fengqi Zhang, Anika Kiersnau, Qi Shen, Hanggai, and Diego Pineda Quijano — it was a pleasure to collaborate, discuss, and celebrate with you. I am proud to have worked with such talented colleagues and look forward to future collaborations.

I am fortunate to have met Zhou Zhou, Xiaoyu Zhang, Shasha Lv, Yaolin Xu, Hongde Luo, Tiantian Yao, Fengjiao Qian, and Wenqin Shi. You welcomed me warmly and introduced me to the RID Chinese alumni community. I enjoyed your speeches and conversations during our gatherings, and I miss the summer and New Year parties as you all departed one by one. I also want to thank my fellow PhDs and postdocs at RID: Tomas Verhallen, Niek de Klerk, Violetta Arszewska, Evgenii Velichka, Alexandros Vasileiadis, Viviana Marques Pereira, Steven Parnell, Swapna Ganapathy, Lars Bannenberg, Hanan Al-Kutubi, Remco van der Jagt, Tammo Schwietert, Jens Noorlander, Chuang Yu, Haixing Fang, Zhaolong Li, Bo Peng, Bei Tian, Yifan Fu, and Chao Wang—it was wonderful to have your companionship and support throughout this journey.

My particular acknowledgments go to my supervisor, Prof. Dr. DeChang Zeng at South China University of Technology (SCUT). You encouraged me not to settle and inspired me to see my PhD as the beginning of my career. You introduced me to a research field where I could dedicate my passion and contribute to sustainability. Besides, I would like to thank my daily supervisor Dr. Zhigang Zheng, who showed me all the basics of a magnetic refrigerator. You are such an easy-going teacher and hardworking colleague, I enjoyed all the time we worked together.

My sincere thanks also go to Prof. Dr. Frank de Boer. You equipped me with the fundamentals of solid-state physics and connected me with TU Delft and Ekkes. I thoroughly enjoyed your course at SCUT and admire your spirit of knowledge-sharing and collaboration.

I am deeply grateful to Ben Harrison, whose panoramic skills in system engineering and rich life experience were invaluable during the ups and downs of my device development. You have been both a consultant and a friend, and I hope to lead a life as fulfilling as yours.

To my friends Zhaoguo Qiu and Fa Chang—I cannot thank you enough for helping me navigate the challenges of knowledge and cultural adjustment at the start of my PhD. Your support back in China has been crucial during my time in the Netherlands.

Special thanks to my friends Xu Ma and Jiawei Lai — I am so grateful that we began our journey in the Netherlands together. As part of the same sponsorship batch, we supported each other in countless ways and shared many great experiences. Specifically, Jiawei, I enjoyed every talk we have, you can't imagine how much you helped me with your material science specialties.

I owe a great deal to my best mate Hengqian Yi, who shared the most significant part of my time in the Netherlands. I cherish our conversations, adventures, and the crazy ideas we discussed that now seem quite achievable. I hope you and Yunran Qiu find the perfect place to settle down and start a lovely family soon.

My gratitude extends to my colleagues at Magneto B.V.: Bennie Reesink, Michael Mascheck, Alexandar Gunkel, and Ivo Dusek — it has been a pleasure to start a deep-tech business with you. Ted van Burk, Xinmin You, Eduard Pieter, Jilles Langeveld, Dr. Hamutu Ojiyed, Karlijn van Buitenen, Jasper Pierik, Daniel J. Kurucz, Gijs Groote, and Dr. Ivan Batashev—you are the core of Magneto, and without you, our innovative products would not exist. It is a great honor to work alongside you.

Finally, I want to thank my parents for their love, support, and unwavering belief in my abilities. As an only child living abroad, I owe you so much. A special thanks to my beloved wife, Huijun Ren, who brought sunshine and more — our little angel, Celine, into my life. My achievements have only been possible through your understanding and sacrifice. Love you forever!

Bowei Huang
Aug. 2024 in Jiujiang

CURRIUCLUM VITAE

Bowei Huang, born on November 11th, 1986, in Jiujiang, China, is a motivated and disciplined researcher with a passion for innovation. He is currently a PhD candidate in Applied Science at Delft University of Technology and a member of the Fundamental Aspects of Materials and Energy research group.



During his MSc studies, under the supervision of Prof. Shaowu Zhou, Bowei led the development of a Zigbee-based maximum cluster-centered positioning algorithm, successfully implemented in an underground mining personnel positioning wireless sensor network. His exceptional contributions earned him a Master's degree with honors in July 2011.

Bowei then shifted his focus from embedded electronics to magnetocaloric technology during his PhD research in September 2011. Initially guided by Prof. DeChang Zeng at South China University of Technology, and later by Prof. Ekkes Brück and Dr. Niels van Dijk at Delft University of Technology, Bowei designed and constructed three innovative magnetocaloric devices: the Magnetocaloric heat pump prototypes SCUT MKIII and FAME Cooler, and the thermomagnetic motor TMM0.

As his PhD research progressed, Bowei co-founded Magneto B.V., a startup spin-off from Delft University of Technology. At Magneto, he manages engineering development and customer coordination. Recently, the Magneto team developed the 3D mesh magnetocaloric heat exchanger, a fully customizable solution for various magnetocaloric heat pumps and thermomagnetic motors.

Looking ahead, Bowei Huang is dedicated to advancing the magnetocaloric industry, aiming to contribute to a greener, more sustainable future.

